

Alma Mater Studiorum – Università di Bologna

DOTTORATO DI RICERCA IN

**BIOINGEGNERIA**

Ciclo XXVIII

Settore Scientifico disciplinare: ING-IND/34

---

**Development of new bioactive and porous apatitic  
scaffolds for the regeneration of load-bearing bones**

A dissertation by

**Massimiliano Dapporto**

*Ph.D. candidate*

*Supervisor*

**Prof. Luca Cristofolini**

*Co-supervisors*

**Dott. Simone Sprio**

**Dott.ssa Anna Tampieri**

*PhD Coordinator*

**Prof. Elisa Magosso**

**Esame finale Anno 2016**



# CONTENTS

<b>SUMMARY</b> .....	7
<b>CHAPTER 1 INTRODUCTION</b> .....	<b>11</b>
1.1 The Human Skeleton.....	11
1.2 The Bone Structure.....	13
1.2.1 Bone Tissue .....	13
1.2.2 Bone Cells.....	16
1.2.3 Bone Modeling and Remodeling .....	18
1.3 Bone Tissue Engineering and calcium orthophosphates.....	20
1.3.1 Cranial injuries and cranioplasty.....	23
1.3.1.1 Anatomy of the skull .....	24
1.3.1.2 Cranioplasty.....	25
1.3.1.3 Porous bioceramic scaffolds .....	27
1.3.1.4 Hydroxyapatite.....	30
1.3.2 Spinal injuries and vertebroplasty .....	32
1.3.2.1 Anatomy of the spine .....	32
1.3.2.2 Osteoporosis and vertebroplasty.....	34
1.3.2.3 Bone cements.....	36
1.3.2.4 Tricalcium phosphate (TCP) .....	39
1.4 References.....	40
<b>CHAPTER 2 OVERVIEW OF METHODS</b> .....	<b>45</b>
2.1 X-Ray Diffraction (XRD).....	45

2.2 Scanning Electron Microscopy (SEM) .....	50
2.3 Inductively Coupled Plasma Optical Emission Spectroscopy .....	53
2.4 Specific Surface Area.....	54
2.5 Particle Size Distribution.....	56
2.6 Rheology of suspensions .....	58
2.7 Thermogravimetric analysis (TGA) .....	60
2.8 Zeta Potential.....	61
2.9 Mercury porosimetry.....	62
2.10 Mechanical characterization .....	63
2.10.1 Compression.....	63
2.10.2 Flexure (4-point bending).....	64
2.11 Design of Experiments.....	65
2.12 References .....	69
<b>CHAPTER 3 MACROPOROUS APATITE-BASED SCAFFOLDS .....</b>	<b>71</b>
3.1 Preparation of macroporous bioceramic scaffolds .....	71
3.1.1 Replica Method .....	71
3.1.2 Direct Foaming Method .....	73
3.2 Results and Discussion.....	74
3.2.1 Replica method: role of sponge and thermal treatment.....	74
3.2.2 A novel Direct Foaming route .....	76
3.3 Conclusions.....	83
3.4 References.....	84
<b>CHAPTER 4 PREPARATION OF <math>\beta</math>-TCP SCAFFOLDS BY ROBOCASTING .....</b>	<b>87</b>
4.1 The robocasting as additive manufacturing approach.....	87

4.2 Preparation of calcium phosphate pastes for robocasting .....	89
4.3 Results and Discussion.....	92
4.4 Conclusions.....	102
4.5 References.....	103
<b>CHAPTER 5 DEVELOPMENT OF APATITIC BONE CEMENTS.....</b>	<b>105</b>
5.1 Preparation of Sr-doped Calcium Phosphate bone cements (CPCs) ..	105
5.1.1 Synthesis and characterization of Sr- $\alpha$ TCP phases.....	106
5.1.2 Synthesis of aqueous setting solutions.....	108
5.1.3 Liquid-On-Powder Ratio And Mixing Procedure.....	108
5.2 Results and Discussion.....	110
5.2.1 Characterization of the Sr-doped CPCs.....	110
5.2.2 Designing the performance of CPCs.....	122
5.3 Conclusions.....	126
5.4 References.....	127
<b>FINAL CONCLUSIONS AND FUTURE PERSPECTIVES .....</b>	<b>131</b>
<b>ACKNOWLEDGMENTS .....</b>	<b>133</b>



# SUMMARY

---

The research activity described in the present thesis is devoted to the design and development of porous bioactive ceramic materials and scaffolds addressed to the regeneration of bone tissue and was mainly carried out at the Institute of Science and Technology for Ceramics, belonging to the National Research Council of Italy (ISTEC-CNR), during my Ph.D. in Bioengineering.

In the last decades the development of porous bioactive scaffolds for bone tissue engineering has become a major area of material science and biomedical research, including interdisciplinary approaches spanning from the field of chemistry, engineering, medicine and biology.

Nowadays there is still a lack of effective therapies able to regenerate large bone defects, so that the development of implantable bioactive materials able to overcome the drawbacks related to the use of bone autografts and allografts is highly demanded. In fact, the currently used bio-inert devices (e.g. metallic devices) can merely provide a mechanical support without regenerating the damaged bone tissue often inducing adverse side effects while forcing the patient to frequent revision surgeries, with also relevant socio-economic impact.

In this respect, the synthesis of artificial bioactive scaffolds able to mimic the compositional, morphological and mechanical features of bone is considered as the elective approach for effective tissue regeneration.

The main aim of my work was the design and optimization of forming processes to produce bioactive ceramics implants as potential solution for the treatment of large and load-bearing bone defects, particularly in the field of cranio-maxillofacial, orthopaedic and spinal surgery.

The main inorganic component of bone tissue is a calcium phosphate phase, with the structure of hydroxyapatite,  $\text{Ca}_{10}(\text{PO}_4)_6(\text{OH})_2$ .

Therefore, the elective materials to provide bone-mimicking scaffolds are calcium phosphates, mainly hydroxyapatite and tricalcium phosphates.

The processing of these materials into 3-dimensional biomimetic structures with controlled porosity and adequate structural properties, would favour new bone formation, penetration and integration with the scaffold.

Clinical application of synthetic materials is mainly hampered by the difficulty in achieving adequate reproducibility of the scaffold final performance, particularly if the treatment of large bone defects is demanded. Moreover, the size and shape of scaffolds for bone reconstruction should face specific anatomical requirements, so that flexible fabrication technologies are requested to tailor the chemistry and architecture of the porous scaffolds in respect to specific applications in bone surgery.

After a general introduction of bone tissue physiology and an overview on the analytical methods involved in the research (Chapter I and Chapter II, respectively), this thesis focuses on the preparation of macro-porous apatitic structures via a novel route based on the direct foaming of ceramic suspensions with high-energy planetary ball milling (Chapter III). This method, here used for the first time in the production of foamed ceramic suspensions, enabled a radical optimization of the production process significantly improving the final mechanical properties, thus opening to the development of large and complex-shape porous scaffolds. Then, Chapter IV describes the preparation of robocasted 3-D macroporous scaffolds for applications in orthopaedics, performed during my 6-months stage at Imperial College London. In this respect, an extensive optimization of the rheology of colloidal inks based on bioactive  $\beta$ -tricalcium phosphate was carried out, pointing out a reliable formulation to obtain scaffolds with controlled architecture by the layer-by-layer deposition of ceramic material. Finally, Chapter V describes the synthesis and optimization of a novel bioactive calcium phosphate bone cement based on strontium-substituted apatite, here proposed for the first time in a formulation enriched with bio-erodible alginate, to improve cohesion and osteoconductivity. The optimization process enabled the



synthesis of fully injectable pastes, exhibiting also improved biologic performance, if compared with a commercial calcium phosphate cement.

In the present thesis, the optimization of the various parameters significantly affecting the final properties of the described biomaterials was performed according to a Design of Experiment approach (DoE). In this way, the parameters were varied following rational combinations, leading to time and resources saving, while obtaining preliminary modeling equations of the processes.



# Chapter 1

## INTRODUCTION

---

### 1.1 The Human Skeleton

Sitting, standing, walking and taking a breath are examples for daily acts involving our skeleton. Without a skeletal system, there would be no rigid framework to support the soft tissues of the body and no system of joints and levers to allow the body to move (Fig.1.1).



**Fig. 1.1 - The human skeleton** ([www.clipartof.com](http://www.clipartof.com))

The human skeleton is composed of 270 bones at birth, which decreases to 206 bones by adulthood after some bones have fused together.

Although the skeleton is usually thought of as only the rigid framework of the body, the bones provide: 1) *structural support* for the body, allowing movement and locomotion by providing levers for the muscles, 2) *protection* for vital internal organs from damage, 3) maintenance of *mineral homeostasis* and acid-base

balance, 4) reservoirs of growth factors and cytokines and 5) the environment for *hematopoiesis* within the marrow spaces [1].

The bones can be classified according to the region of the skeleton they belong to, or their general shape.

In the former case, the skeleton has been divided into two different regions: the axial skeleton, including the skull, the vertebral column and the rib cage, and the appendicular skeleton, which consists of the arms, pectoral girdles, legs and pelvic girdle.

In the latter case, long bones, short bones, flat bones, and irregular bones have been classified. Long bones include the femur, humeri, clavicles, radii, ulnae, metacarpals, tibiae, fibulae, metatarsals, and phalanges. Short bones include the carpal and tarsal bones, patellae, and sesamoid bones. Flat bones include the skull, mandible, scapulae, sternum, and ribs. Irregular bones include the vertebrae, sacrum, coccyx, and hyoid bone.

The typical macrostructure of bones is reported in Fig.1.2 and Fig.1.3, where a long bone has been chosen as a useful model. Each long bone consists of a central shaft, the *diaphysis*, and two ends, the so-called *epiphysis*. A thin layer of articular cartilage covers the epiphyses where the bone articulates with other bones (joints).

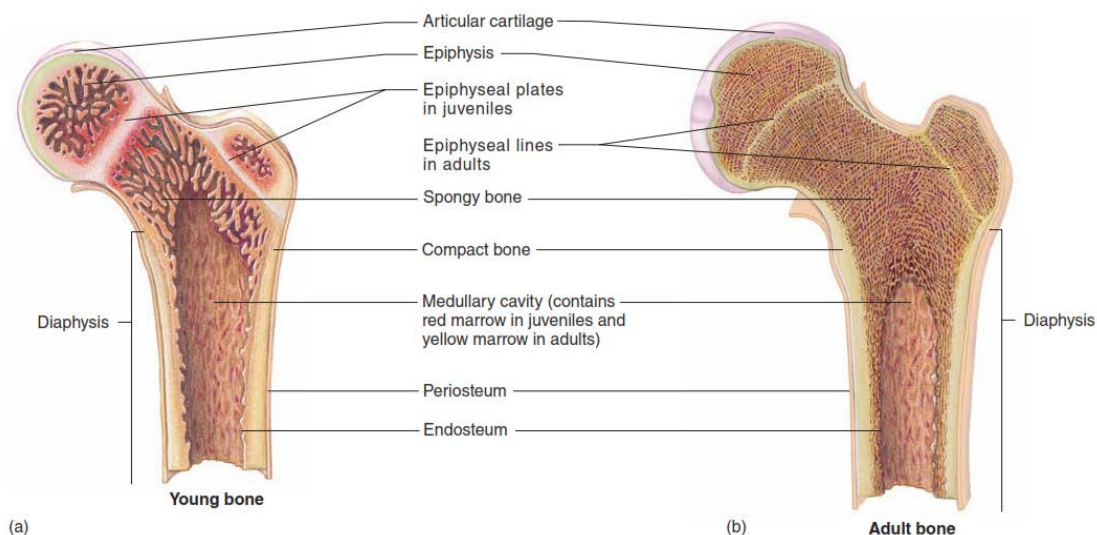


**Fig.1.2 - Structure of a long bone - Young long bone (the femur) showing the epiphysis, epiphyseal plates, and diaphysis (a), adult long bone with epiphyseal lines (b)** (The McGraw-Hill Companies, Inc.)

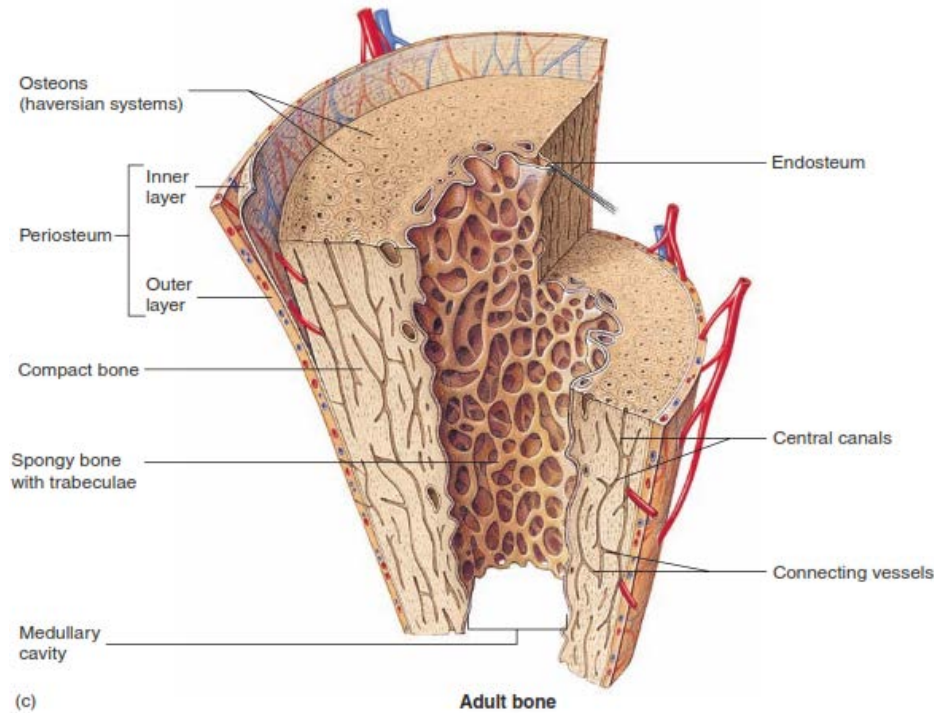


**Fig.1.3 - Structure of a long bone - Internal features of a portion of the diaphysis** (The McGraw-Hill Companies, Inc.)

## 1.2 The Bone Structure

### 1.2.1 Bone Tissue

The bone tissue is the major structural and supporting connective tissue of the body, composed of a tough *organic matrix* that is greatly strengthened by deposits of *calcium salts*.

The crystalline salts deposited in the organic matrix of bone are composed principally of calcium and phosphate. The formula for the major crystalline salt, known as *hydroxyapatite*, is  $\text{Ca}_{10}(\text{PO}_4)_6(\text{OH})_2$ .

Average compact bone contains about 30 wt% matrix and 70 wt% salts. Newly formed bone may have a considerably higher percentage of matrix in relation to salts.

The organic matrix of bone is 90-95% collagen fibers, while the remaining part is a homogeneous gelatinous medium called *ground substance*. The collagen fibers

extend primarily along the lines of tensional force, providing the bone with its powerful tensile strength.

The ground substance is composed of extracellular fluid plus proteoglycans, especially chondroitin sulfate and hyaluronic acid. The precise function of each of these is not known, although they do help to control the deposition of the mineral phases.

Each bone is composed of two main different bone types: the compact (or cortical) bone and the spongy (or trabecular) bone. Cortical bone is denser and surrounds the marrow space, whereas trabecular bone is composed of a honeycomblike network of trabecular plates and rods interspersed in the bone marrow compartment. Both cortical and trabecular bone are composed of osteons (Fig.1.4).

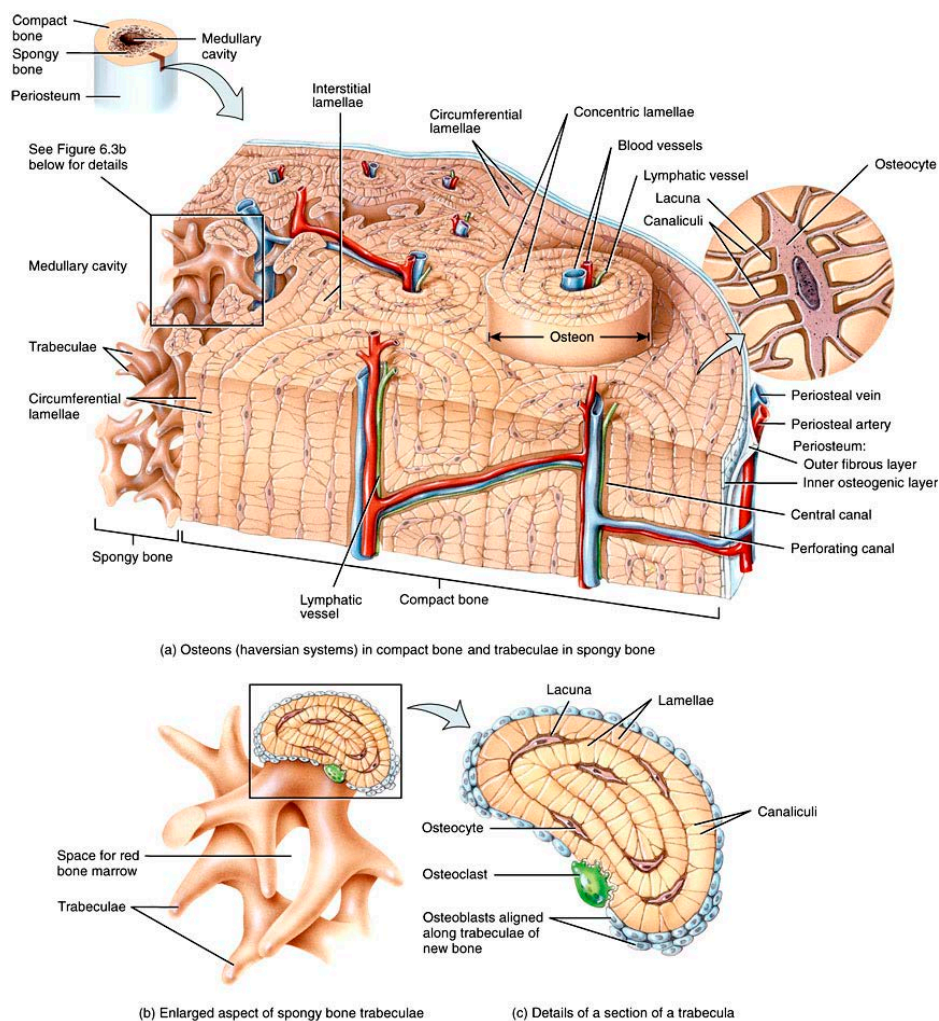


**Fig.1.4 - Histology of bone tissue** (©John Wiley & Sons, Inc.)

The adult human skeleton is averagely composed of 80% cortical bone and 20% trabecular bone. However, different bones may have different cortical to trabecular bone ratio: for example, the vertebrae, the femoral heads and the femoral diaphysis are characterized by a ratio equals to about 25:75, 50:50 and 95:5, respectively.

The bone tissue is characterized by a hierarchical structure that ranges over 9-10 orders of magnitude in length, from the molecular level to the bone structure (Fig.1.5).

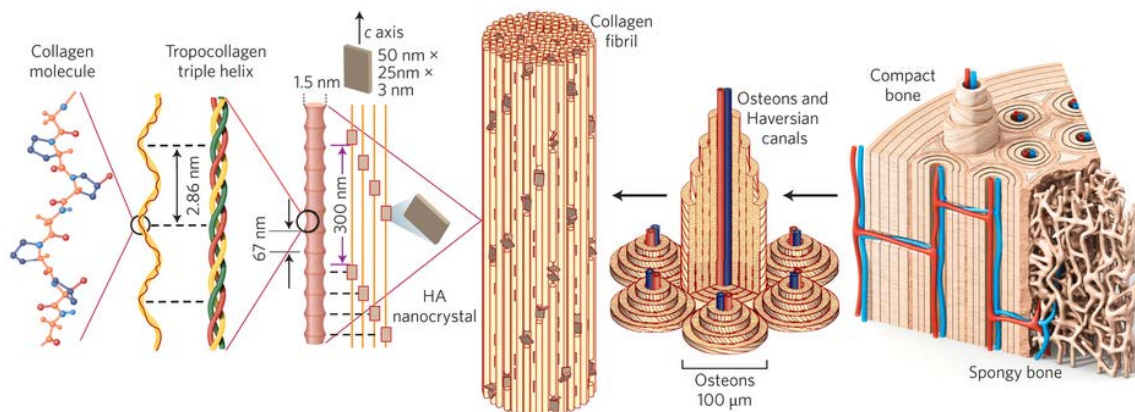


**Fig.1.5 – Hierarchical structure of bone – Macroscale arrangements involve both compact/cortical bone at the surface and spongy/trabecular bone in the interior.**

The bone is composed of cells embedded in an extracellular matrix, which is an ordered network assembled from two major nanophases: collagen fibrils made from type-I collagen molecules (~300 nm long, ~1.5 nm in diameter) and hydroxyapatite nanocrystals (plate-shaped, 50 nm × 25 nm in size, 1.5–4 nm thick) distributed along the collagen fibrils. The hydroxyapatite nanocrystals are preferentially oriented with their c axis parallel to the collagen fibrils, and arranged in a periodic, staggered array along the fibrils [2]. These two nanophases make up about 95% of the dry weight of bone. The structures form a tough yet lightweight, adaptive, self-healing and multifunctional material. Bone derives its resistance to fracture with a multitude of deformation and toughening mechanisms operating at many size scales, ranging from the nanoscale structure of its protein molecules to the macroscopic physiological scale.

### 1.2.2 Bone Cells

Bone tissue is continuously remodeled through the concerted actions of bone cells, which include *osteogenic cells*, *osteoblasts*, *osteoclasts*, *osteocytes* and *bone-lining cells* [3] (Fig.1.6).

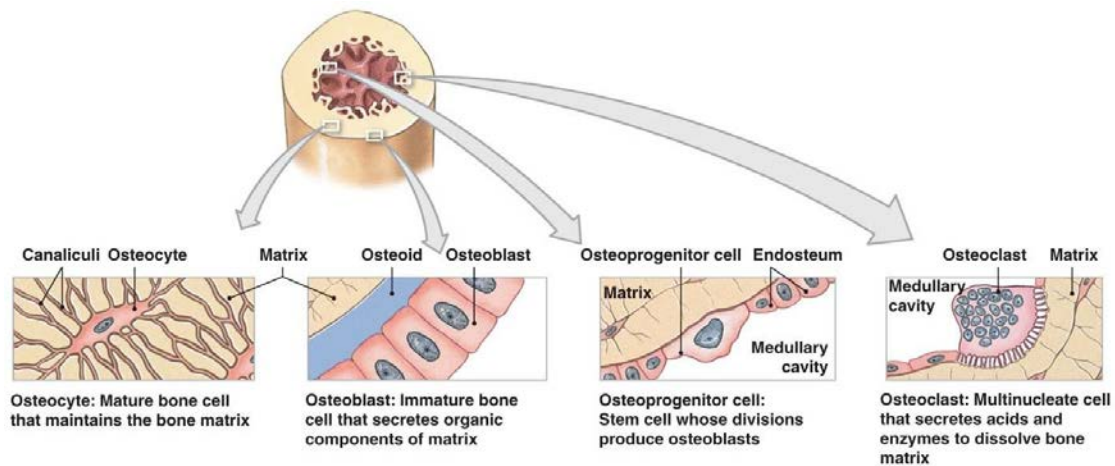


**Fig.1.6 – Types of bone cells** (Anatomy and Physiology, Martini, 2007)

#### Osteoprogenitor cells

The osteoprogenitor cells are stem cells derived from the embryonic mesenchymal tissue. They are found in the endosteum and the periosteum, and in the central canals of bones. The osteogenic cells are the only bone cells that divide, differentiating into osteoblasts which, in turn, are responsible for forming new bone.

#### Osteoblasts

Osteoblasts play a very important role in creating and maintaining skeletal architecture; these cells are responsible for the deposition of bone matrix and for osteoclasts regulation. Osteoblasts are mononuclear, not terminally differentiated, specialized cells [4]. When they are active, a large Golgi apparatus and an abundant rough endoplasmic reticulum is visible. In addition, osteoblasts form tight junctions with adjacent osteoblasts [5].

As they differentiate they acquire the ability to secrete bone matrix. Ultimately, some osteoblasts become trapped in their own bone matrix giving rise to osteocytes.



### **Osteoclasts**

Osteoclasts are multinucleated giant cells that differentiate from myeloid precursors under the influence of the cytokines macrophage colony stimulating factor (M-CSF) and receptor activator of NF- $\kappa$ B ligand (RANKL) supplied by osteoblasts and/or osteocytes [6]. Osteoclasts degrade bone by the polarized secretion of proteolytic enzymes (e.g., cathepsin K) and acids, which hydrolyze and solubilize the organic and inorganic components of bone, respectively.

Subsequent to the osteoclastic resorptive phase, coupling mechanisms promote the recruitment and differentiation of mesenchyme-derived osteoblast progenitors at the resorption lacunae. After these cells mature into osteoblasts, they line the eroded bone surface and secrete the organic component of bone, termed osteoid, which is mineralized over time by the incorporation of hydroxyapatite [7]. As osteoblasts secrete osteoid, some cells are entrapped within the matrix where they eventually become osteocytes.

### **Osteocytes**

Osteocytes are the most abundant cells in bone; these cells communicate with each other and with the surrounding medium through extensions of their plasma membrane [8].

Osteocytes are embedded in osteons arranged concentrically around the Haversian canal. An osteocyte resides in a lacuna and connects to other osteocytes through its processes that extend through the canaliculi. Mechanical loads on bone induce fluid flow in the canalicular space.

Therefore, osteocytes are thought to act as mechanosensors, instructing osteoclasts where and when to resorb bone and osteoblasts where and when to form it [9].

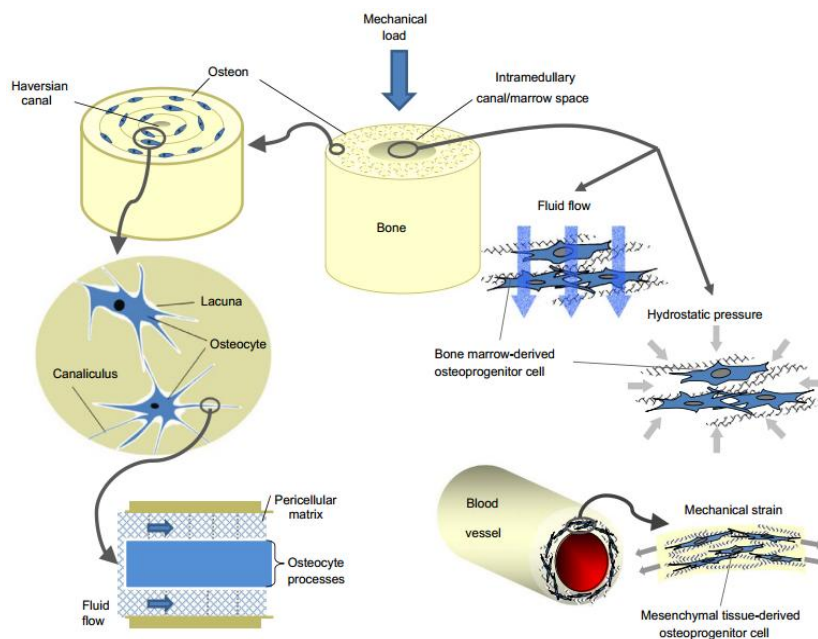


**Fig.1.7 – Schematic of the anatomical locations of and mechanical loads experienced by osteocytes and osteoprogenitor cells [9].**

### Bone-lining cells

Bone lining cells, or periosteal cells, are flattened in shape, with few cell organelles. These cells cover the surface of bones and are found to affect both the bone remodeling and the concentration of minerals in blood and bone tissues. It is observed that mechanical loading stimulates bone formation by reactivation of bone-lining cells to become active osteoblasts. Bone-lining cells occupy the majority of adult bone surface. They serve as an ion barrier separating fluids percolating through the osteocyte and lacunar canalicular system from the interstitial fluids.

### 1.2.3 Bone Modeling and Remodeling

The bone is a complex, living tissue that is constantly adapting to metabolic and structural demands. Because it is a mineralized tissue, all changes in external osseous form occur along vascularized periosteal surfaces via uncoupled anabolic and catabolic modeling events. Modeling changes the shape and size of bones in response to mechanical loading or wounding. On the other hand, remodeling is

turnover of bone that is related to bone maturation, skeletal maintenance, and mineral metabolism.

Bone modeling activity is a mechanically mediated adaptive process supposed to be controlled by the peak strain of dynamic loading [10, 11] (Fig.1.8).

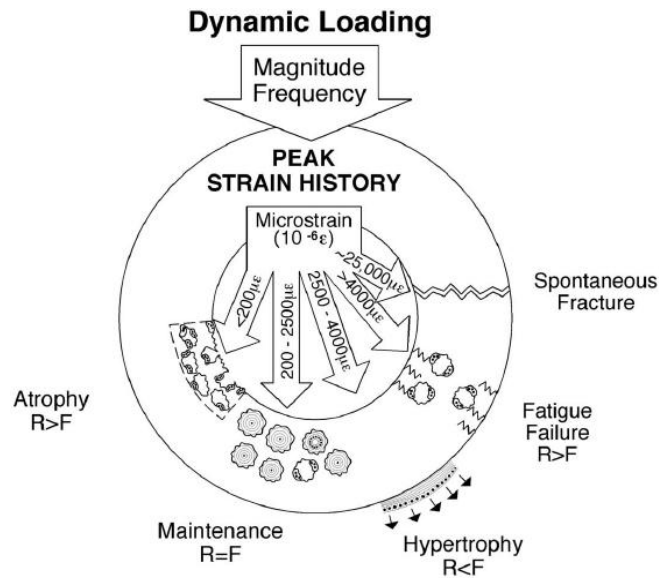


**Fig.1.8 – Frost’s mechanostat shows the relationship of dynamic loading and peak strain history to: atrophy, physiologic maintenance, hypertrophy, fatigue failure, and spontaneous fracture. R = resorption; F = formation [12].**

Sensitive biomechanical feedback of anabolic and catabolic modeling is the mechanism of growth, adaptation and atrophy of the skeletal system. Disuse atrophy and overload hypertrophy are the means for sculpting bones and adapting their mass and orientation to optimally support functional loading.

The bone remodeling begins early in fetal life, and once the skeleton is fully formed in young adults almost all of the metabolic activity is in this form. The bone remodeling cycle involves a series of highly regulated steps that depend on the interactions of two cell lineages, the mesenchymal osteoblastic lineage and the hematopoietic osteoclastic lineage (Fig.1.9).

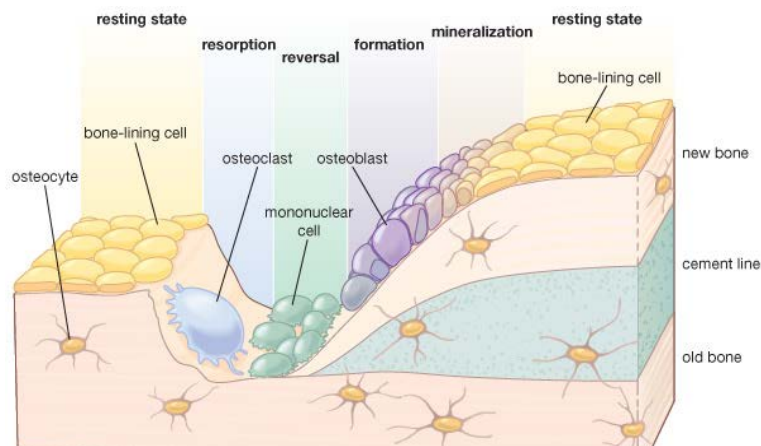


**Fig.1.9 – Bone remodeling process** (©Encyclopaedia Britannica, Inc, 2010)

The initial activation stage, the resting state, involves the interaction of osteoclast and osteoblast precursor cells, thus leading to the differentiation, migration and fusion of the large multinucleated osteoclasts. These cells attach to the mineralized bone surface and initiate bone resorption. Osteoclastic resorption produces irregular scalloped cavities on the trabecular bone surface, called Howship lacunae, or cylindrical Haversian canals in cortical bone. Once the osteoclasts have completed their work of bone removal, there is a “reversal” phase during which mononuclear cells, which may be of the macrophage lineage, are seen on the bone surface. The events during this stage are not well understood, but they may involve further degradation of collagen, deposition of proteoglycans to form the so-called cement line, and release of growth factors to initiate the formation phase. During the final formation phase of the remodeling cycle, the cavity created by resorption can be completely filled in by successive layers of osteoblasts, which differentiate from their mesenchymal precursors and deposit a mineralizable matrix.

### **1.3 Bone Tissue Engineering and calcium orthophosphates**

Bone tissue engineering is a multidisciplinary research area based on the understanding of bone structure, bone mechanics and tissue formation to induce new functional bone tissues. In other words, to successfully regenerate or repair bone, a precise knowledge of the bone biology and its development is essential.

Given the structural and metabolic functions of bones, skeletal defects often incur in considerable morbidity. Conventional medical strategies generally focus on preventing the causes of diseases; when it comes to repair of tissue defects elicited by the diseases, mostly rely on natural healing abilities of tissues, failing to cure irreversible tissue defects. In bone and cartilage, irreversible tissue defects are caused by aging, trauma, disease, tumors as well as developmental abnormalities. The role of Bone Tissue Engineering in the field of Regenerative Medicine has been the topic of substantial research over the past three decades.

Three main pillars of bone tissue engineering were also identified (Fig. 1.10): a scaffold provides a structure for tissue growth, while cells produce the desired tissue under biochemical signaling able to affect their growth and phenotype.

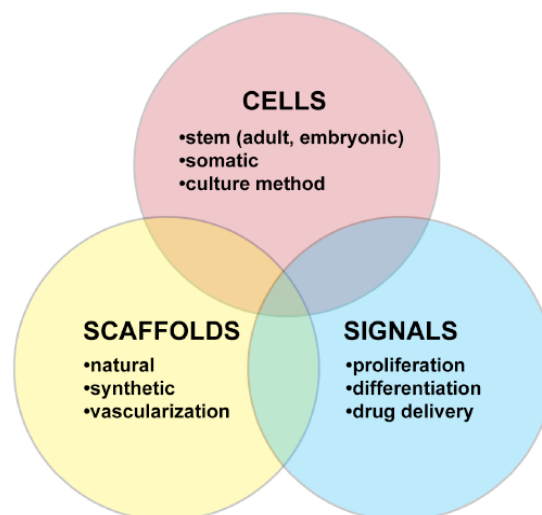


**Fig.1.10 – Scheme of the three pillars of tissue engineering. To bring tissue engineering into reality, it is crucial to sufficiently advance and combine the three [13].**

The calcium orthophosphates are chemical compounds of wide interest in many fields of science, including medicine [14], due to their abundance in nature and presence in living organisms.

By definition, all calcium orthophosphates consist of three major chemical elements, calcium (oxidation state +2), phosphorus (oxidation state +5) and oxygen (reduction state -2), as a part of orthophosphate anions.

In particular, calcium orthophosphates have been studied as bone repair materials for the last 90 years, given their resemblance with the inorganic phase of bones.

The first in vivo use of tricalcium phosphate (TCP) was performed by Albee and Morrison in 1920 [15]. Despite few early experiments, it was only in the 1970's that calcium orthophosphates - mostly hydroxyapatite (HA) - were synthesized, characterized, and applied [16-19].

Calcium orthophosphates were prepared by sintering (thermal consolidation) as granules or blocks, porous or dense. Since then, the interest in these materials has increased. In the mid 1980's, Brown and Chow [20] discovered the first hydraulic calcium phosphate cement, i.e. a mixture of calcium phosphate powders and water that hardened with time at room temperature. This discovery opened up new perspectives for the use of calcium orthophosphates in the treatment of bone defects.

Two different categories of calcium phosphate compounds (CaP) can be distinguished: 1) CaP obtained by precipitation from an aqueous solution at or around room temperature (low temperature), and 2) CaP obtained by thermal reactions (high-temperature) [21] (Fig.1.11).

Name	Formula	Ca/P	Mineral	Symbol
Monocalcium phosphate monohydrate	$\text{Ca}(\text{H}_2\text{PO}_4)_2 \cdot \text{H}_2\text{O}$	0.50	–	MCPM
Dicalcium phosphate	$\text{CaIIP}_2\text{O}_4$	1.00	Monetite	DCP
Dicalcium phosphate dihydrate	$\text{CaHPO}_4 \cdot 2\text{H}_2\text{O}$	1.00	Brushite	DCPD
Octocalcium phosphate	$\text{Ca}_8\text{H}_2(\text{PO}_4)_6 \cdot 5\text{H}_2\text{O}$	1.33	–	OCP
Precipitated hydroxyapatite ("tricalcium phosphate")	$\text{Ca}_{10-x}(\text{HPO}_4)_x(\text{PO}_4)_{6-x}(\text{OH})_{2-x}$	1.50–1.67	–	PHA
Amorphous calcium phosphate $n = 3-4.5; 15-20\% \text{H}_2\text{O}$	$\text{Ca}_3(\text{PO}_4)_2 \cdot n\text{H}_2\text{O}$ 1.50	-	ACP	
Monocalcium phosphate	$\text{Ca}(\text{H}_2\text{PO}_4)_2$	0.50	–	MCP
$\alpha$ -Tricalcium phosphate	$\alpha\text{-Ca}_3(\text{PO}_4)_2$	1.50	–	$\alpha$ -TCP
$\beta$ -Tricalcium phosphate	$\beta\text{-Ca}_3(\text{PO}_4)_2$	1.50	–	$\beta$ -TCP
Sintered hydroxyapatite	$\text{Ca}_5(\text{PO}_4)_3\text{OH}$	1.67	Hydroxyapatite	HA
Oxyapatite	$\text{Ca}_{10}(\text{PO}_4)_6\text{O}$	1.67	–	OXA
Tetracalcium phosphate	$\text{Ca}_4(\text{PO}_4)_2\text{O}$	2.00	Hilgenstockite	TetCP

**Fig.1.11 – Main calcium phosphate compounds. The first 6 compounds precipitate at room temperature in aqueous systems. The last 6 compounds are obtained by thermal decomposition or thermal synthesis [21].**

A key parameter of calcium phosphate compounds is their *solubility* (in water): if the solubility of a CaP is less than the mineral part of bone, it degrades extremely

slowly, whereas if the solubility of a CaP is greater than that of the mineral part of bone, it is too easily degraded.

The analysis of the calcium phosphate solubility reveals that at physiological pH (7.2–7.4) the concentration of Ca and P dissolved from calcium orthophosphates decreases in the order  $\text{TTCP} > \alpha\text{-TCP} > \text{DCPD} > \text{DCPA} > \text{OCP} > \beta\text{-TCP} > \text{HAp}$  (Fig.1.12). However, in those conditions, HA is the most stable of all calcium orthophosphates, and in this way it should precipitate as  $\alpha\text{-TCP}$  dissolution progresses [22].

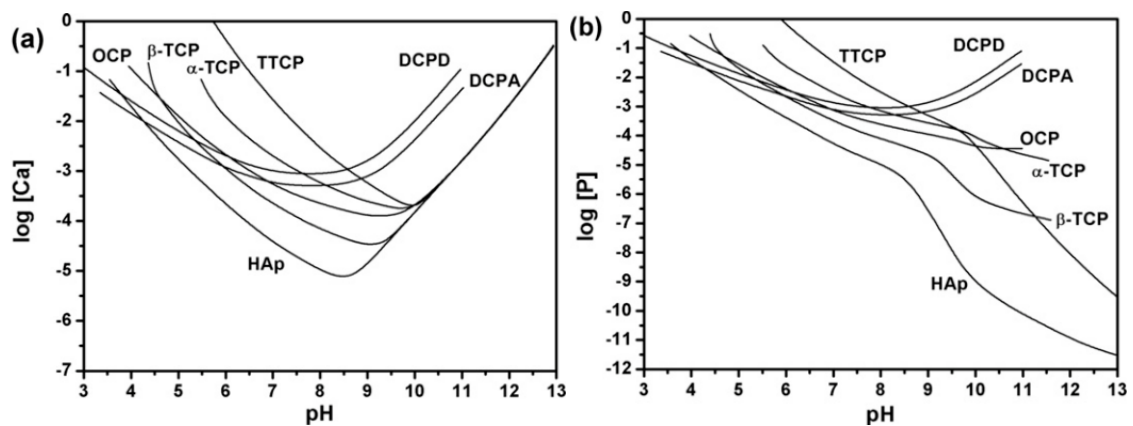


**Fig.1.12 - Solubility phase diagram for the ternary system  $\text{Ca}(\text{OH})_2\text{-H}_3\text{PO}_4\text{-H}_2\text{O}$ , at 37°C: (a) solubility isotherms showing  $\log [\text{Ca}]$  and pH of solution in equilibrium with various salts; (b) solubility isotherms showing  $\log [\text{P}]$  and pH of the solutions [22]. TTCP: tetracalcium phosphate. DCPA: dicalcium phosphate anhydrous. HAp: precipitated apatite**

In the present thesis, the research activity is focused on Bone Tissue Engineering as regards the synthesis, characterization and optimization of *scaffolds* based on hydroxyapatite and tricalcium phosphate for the regeneration of complex-shape large bone defects.

### 1.3.1 Cranial injuries and cranioplasty

Cranial injuries involve trauma to the skull and the brain. The skull is tough, resilient, and provides excellent protection for the brain, but a severe impact or blow can result in fractures and may be accompanied by injuries to the brain.

Head injuries are dangerous, especially because can lead to permanent disability, mental impairment and death.

The cranial-encephalic trauma are considered the main cause of head injury both in Europe and in USA: it is estimated that road accidents are associated with 50% of mortality [23].

Brain injury incidence is higher in young people showing a peak incidence in young adults aged 15-24 with secondary peaks in infants and the elderly between the ages of 70-80.

A skull fracture is a break in one or more of the eight bones that form the cranial portion of the skull, usually occurring as a result of blunt force trauma. If the force of the impact is excessive, the bone may fracture at or near the site of the impact and cause damage to the underlying physical structures contained within the skull such as the membranes, blood vessels and brain, even in the absence of a fracture.

#### 1.3.1.1 Anatomy of the skull

In most of the vertebrates, the *skull* refers to the bony structure mainly deputed to the support of the face and of the protection of the brain, as well as the fixation of the sense organs' position to obtain their optimal functions.

Like other anatomical structures, also the skull is considered to be composed by two main parts: for humans they are identified as neurocranium, referring to the vault surrounding the brain, and the viscerocranium, which refers to the bone surrounding the face. Except for the mandible, the other bones of the skull are joined together by sutures, almost rigid articulations permitting only very little movements.



The brain is not directly in contact with the skull bones because of the interposition of the so called meninges, membranes that envelope the brain and the spinal cord or the central nervous system. In mammals, three meningeal layer are recognized: the *dura mater*, the *arachnoid mater* and the *pia mater* (Fig.1.13).



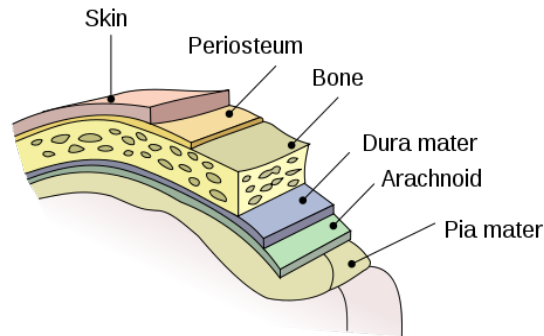


**Fig.1.13 - The meninges** (from Wikipedia)

Both the meninges and the cerebrospinal fluid, a colorless body fluid situated between the arachnoid mater and the pia mater, play a key role in the protection of the central nervous system.

### 1.3.1.2 Cranioplasty

Cranioplasty is the surgical repair of a bone defects of the skull after a previous operation or injury (Fig.1.14).

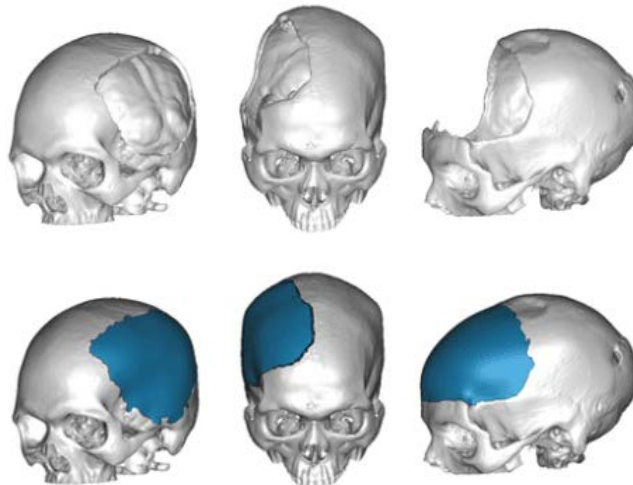


**Fig.1.14 - Skull defects and cranioplasty**

The first attempts to repair cranial bone date back to 7000 B.C., so that cranioplasty is considered one of the oldest neurosurgical practices [24].

Over the past centuries a lot of techniques and materials have been introduced as improvement of neurosurgical care, leading to an increase of the patients surviving cranial injuries. The aim of cranioplasty is not only a cosmetic issue; also, the repair of cranial defects gives relief to psychological drawbacks and increases the social performances.

The cranioplasty is nowadays a mandatory surgical technique following the Decompressive Craniectomy (DC), a potentially life-saving procedure in patients with medically intractable intracranial hypertension secondary to severe closed head injuries or massive strokes. The DC involves the surgical removal of part of the skull in order to facilitate the neurological recovery of severe head injured patients.

Procedural and neurological side effects are to be considered, as the currently available complex and time-consuming techniques are often unsatisfactory, both for the surgeon and the patient [25, 26].

The optimal timing for performing a cranioplasty seems to play a key role not only in avoiding procedure-associated complications, but also in the neurological outcome of these patients. However, the existent data in the literature are not solid enough for drawing any safe conclusions regarding the ideal timing for performing a cranioplasty [27].

An example of custom-made scaffold for regenerative cranioplasty is given by the Custom Bone Service cranial prosthesis from Fin-Ceramica S.p.A, Faenza, Italy [28, 29], consisting in a porous apatitic structure. It may be defined as a biomimetic framework because it is recognised as “self” by the recipient bone, thus avoiding any immunological reaction. Furthermore, it is characterised by a high macro (diameter > 150  $\mu\text{m}$ ), micro (diameter < 10  $\mu\text{m}$ ) and interconnected porosity reaching 70%, allowing high permeability for the cells and blood coming from the recipient bone.

The production begins with the raw digital data obtained during the CT scan; its extensive elaboration allows the creation of essential 3D computer reproduction of the patient’s skull. Only through the raw data elaboration of the CT scan and the subsequent 3D computer reproduction, it is possible to construct a 3D synthetic model of the patient’s skull using stereolithography. From this 3D synthetic model, the first prototype of the custom-made implant is produced. Together with the surgeon, the custom-made prototype is thoroughly reviewed for prospective modifications. This step is extremely important to ensure a custom-made implant which provides a superior aesthetic outcome for the patient and a straightforward

surgical technique for the surgeon. Once the surgeon has approved the custom-made prototype, the final implant is precisely prepared via Replica method, refined, controlled and sterilized prior to shipment to the hospital for implantation.

### **1.3.1.3 Porous bioceramic scaffolds**

Materials containing tailored porosity exhibit special properties and features that usually cannot be achieved by their conventional dense counterparts.

In this respect, in the last decades the porous ceramics have been extensively studied for a wide range of applications and several processing methods were proposed for their preparation [30-34].

The artificial bone substitutes represent one of the most challenging application, especially due to the difficulty of mimicking the properties of the natural bone [35]. Hydroxyapatite (HA) is widely recognized as the golden material for bone and teeth regeneration, due to its close similarity with the inorganic part of bone, which confer excellent biocompatibility and ability to permit new bone formation and adhesion [36-39]. However, in spite a variety of techniques for scaffold development has been investigated so far [30-34], the repeatable and reliable production of HA scaffolds with bone-mimicking pore structure and adequate mechanical strength is still a big challenge [33].

The traditional processes reported in literature for the production of macroporous ceramics are: *partial sintering*, *sacrificial fugitives*, *replica templates* and *direct foaming* (Fig.1.15).

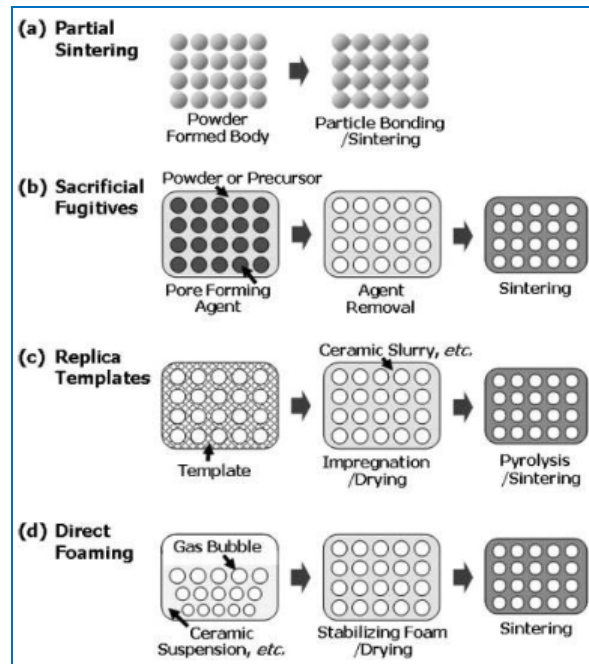


Fig.1.15 – Representative fabrication processes of macroporous ceramics [33]

### Partial sintering

The partial sintering of powder compact is the most conventional and frequently used approach to fabricate porous ceramic materials. The high temperature thermal treatment induces surface diffusion or evaporation-condensation phenomena, leading to a homogeneous porous structure when sintering is terminated before full densified. Pore size and porosity are controlled by the size of starting powders and degree of partial sintering, respectively.

### Sacrificial fugitives

The sacrificial template technique usually foresees to prepare a biphasic composite consisting of a continuous matrix of ceramic powders and a dispersed sacrificial phase that is initially homogeneously distributed throughout the matrix and finally extracted to generate pores inside the microstructure. Porosity is controlled by the amount of the agents. This approach is useful particularly for obtaining high open porosity.

### Replica Templates

The Replica method is considered as the first method used for the production of macroporous ceramics. It involves the impregnation of a polymeric cellular structure with a ceramic suspension in order to produce a macroporous ceramic

exhibiting the same morphology as the original template. The success of this method is attributed to its simplicity and flexibility. However, some critical aspects have to be strictly controlled and optimized, such as the rheological behavior of the ceramic suspensions (shear-thinning), the presence of binders or plasticizers in the initial suspension to avoid the strut cracking during pyrolysis and the final thermal treatment parameters (heating rate, high temperature). In this respect, a disadvantage of this method is the cracking of the struts after thermal treatment, leading to a severe degradation of the mechanical performance of the structure.

### **Direct foaming**

The direct foaming method was stated to be a low-cost and easy process that can provide pore volumes in the range 40-97% by incorporating a gas (e.g. air) into a ceramic suspension, that is subsequently dried and sintered. The total porosity of directly foamed ceramics is proportional to the amount of gas incorporated into the suspension or liquid medium during the foaming process. The pore size, on the other hand, is determined by the stability of the wet foam before setting takes place.

Cellular structures prepared by direct foaming usually exhibit considerably higher mechanical strength than those obtained by other template-based techniques, mainly due to the strongly reduced occurrence of flaws in the cell struts [34].

Liquid foams are thermodynamically unstable systems due to their high gas-liquid interfacial area. Several physical processes take place in wet foams to decrease the overall system free energy, leading to foam destabilization. The main destabilization mechanisms are: *drainage*, *coalescence*, *Ostwald ripening* [34].

Drainage is the physical separation between the gaseous and liquid phases of the foam because of the effect of gravity: light gas bubbles move upwards forming a denser foam layer on the top, while the heavier liquid phase is concentrated on the bottom (Fig. 1.16a).

Coalescence takes place when the thin films formed after drainage are not stable enough to keep the touching cells apart, resulting in the association of neighboring bubbles: the stability of the thin films is determined by the attractive and repulsive interactions between bubbles (Fig. 1.16b). Coalescence is favored by attractive van

der Waals forces and can only be hindered by providing steric and/or electrostatic repulsion among the interacting bubbles.

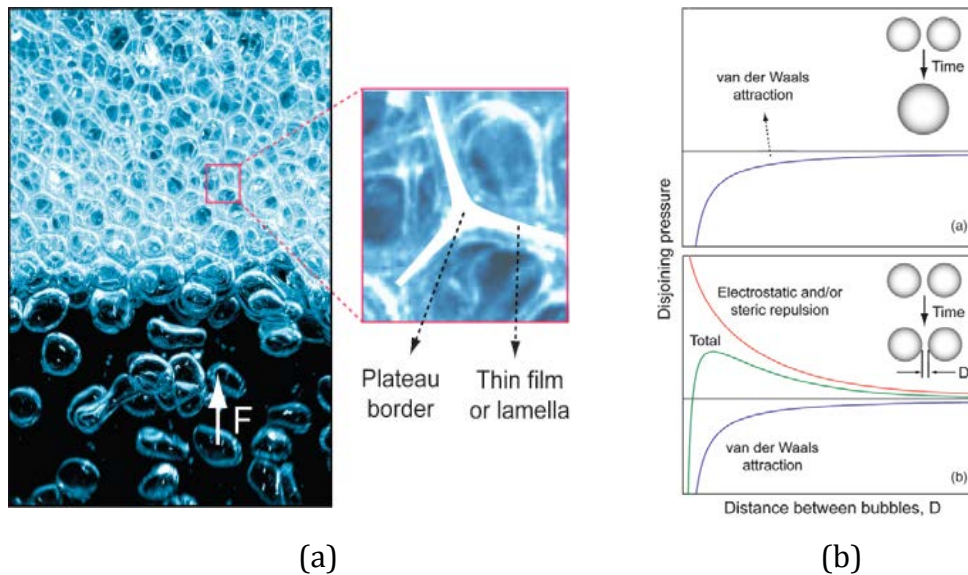


**Fig.1.16: Foam drainage (a), coalescence: schematic dependence of the disjoining pressure among two interacting gas bubbles as a function of their distance (b).**

Foams can be tailored to efficiently prevent drainage and coalescence processes, but in long-term the Ostwald ripening phenomenon can occur, leading to the destabilization of the system due to the difference in Laplace pressure between bubbles of different sizes.

Surfactants and biomolecules adsorbed at the gas-liquid interface can slow down this coarsening process by decreasing the interfacial energy [34].

#### 1.3.1.4 Hydroxyapatite

The hydroxyapatite is a naturally occurring mineral form of calcium apatite with the formula  $\text{Ca}_5(\text{PO}_4)_3(\text{OH})$ , but is usually written  $\text{Ca}_{10}(\text{PO}_4)_6(\text{OH})_2$  to denote that the crystal unit cell comprises two entities (Fig.1.17). It is also the main inorganic component of biological hard tissues such as bones and teeth of vertebrates.

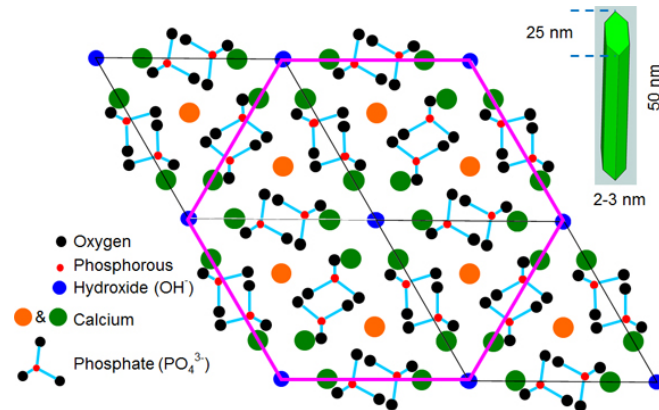


**Fig.1.17 – Bidimensional schematic representation of the hydroxyapatite crystal lattice**

Biological apatite is an inorganic calcium phosphate salt in apatite form and nanosize with a biological derivation. Additionally, due to the similarity in chemical compositions and structure, together with its outstanding bioactivity and biocompatibility, biological apatite has been used as bone substitutes for the reconstruction of bone defect in oral implantology, periodontology, oral, and maxillofacial surgery as well as orthopedics. Given the significant role of biological apatite in the structure and function of biological tissues and its clinical applications, numerous studies have been carried out in the investigation of its basic physiochemical and biological properties.

The composition and structure of synthetic precipitated apatite (HAp) have been studied as potential precursor of biological apatite.

The structure of apatite allows for wide compositional variations because of its ability in detaining different ions in its three sublattices. In detail, the site of  $\text{Ca}^{2+}$  may be occupied by bivalent or monovalent cations such as  $\text{Sr}^{2+}$ ,  $\text{Ba}^{2+}$ ,  $\text{Mg}^{2+}$ ,  $\text{Na}^+$ , and  $\text{K}^+$ , the site of P could be substituted by atoms such as C, As, V, S, while hydroxyl ( $\text{OH}^-$ ) may be replaced by  $\text{OD}^-$ ,  $\text{CO}_3^{2-}$ ,  $\text{F}^-$ ,  $\text{Cl}^-$  or even be left vacant [40] (Fig.1.18).

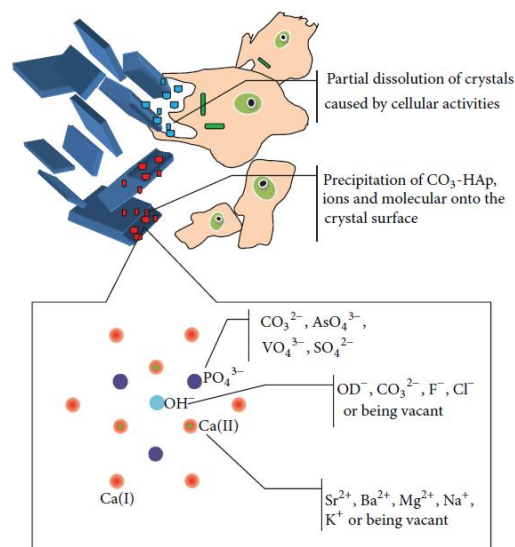


**Fig.1.18– Schematic drawing of partial dissolution/precipitation of biological apatite *in vivo* and ionic substitutions in the crystal of HAp [40]**

Two different crystal forms were reported: *hexagonal*, with the lattice parameters  $a = b = 9.432 \text{ \AA}$ ,  $c = 6.881 \text{ \AA}$ , and  $\gamma = 120^\circ$  [41] and *monoclinic*, with the lattice parameters  $a = 9.421 \text{ \AA}$ ,  $b = 2a$ ,  $c = 6.881 \text{ \AA}$ , and  $\gamma = 120^\circ$  [42].

Each crystal is shaped like a long, flat plate. The relative ratio of calcium to phosphorus can vary markedly under different nutritional conditions, the Ca/P ratio on a weight basis varying between 1.3 and 2.0.

### 1.3.2 Spinal injuries and vertebroplasty

#### 1.3.2.1 Anatomy of the spine

The vertebral column, also known as the *backbone* or *spine*, is a bony skeletal structure found in vertebrates. The spine is made of 33 individual bones stacked one on top of the other (Fig.1.19).



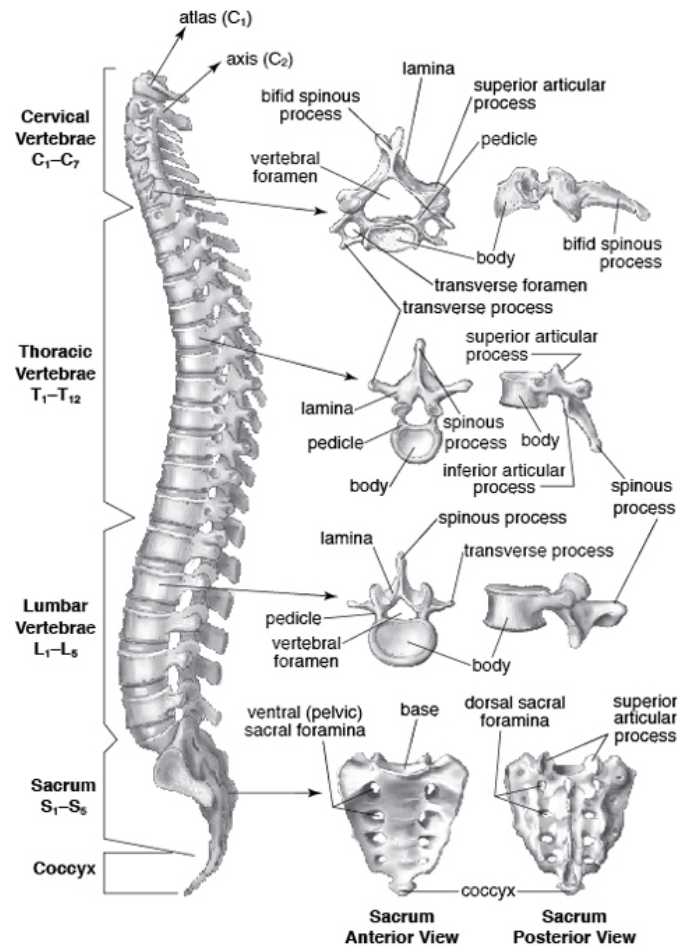


**Fig.1.19 – Anatomy of the vertebral column**

The vertebrae are numbered and divided into five regions: *cervical*, *thoracic*, *lumbar*, *sacrum*, and *coccyx*. Only the top 24 bones are moveable, while the vertebrae of the sacrum and coccyx are fused together. The vertebrae in each region have unique features that help them perform their functions.

Ligaments and muscles connect the bones together and keep them aligned. The spinal column provides the main support for your body, allowing you to stand upright, bend, and twist.

Protected deep inside the bones, the spinal cord connects your body to the brain, allowing movement of your arms and legs (Fig.1.20).

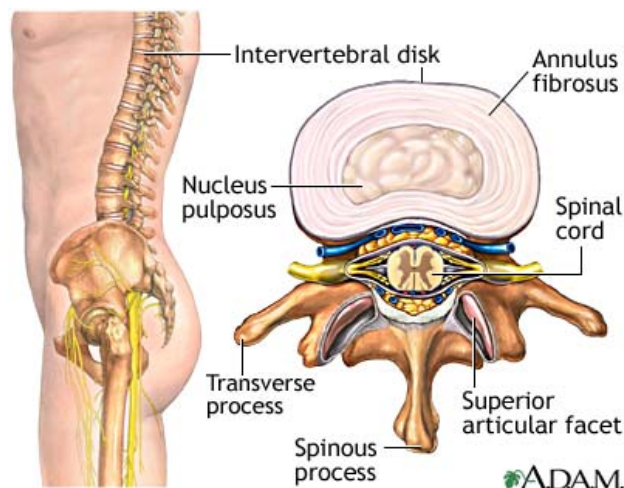


**Fig.1.20 – Axial (overhead) view of a vertebra and structure of the spinal cord**  
(<http://keckmedicine.adam.com/>).

Strong muscles and bones, flexible tendons and ligaments, and sensitive nerves contribute to a healthy spine. Keeping your spine healthy is vital if you want to live an active life without back pain.

#### **1.3.2.2 Osteoporosis and vertebroplasty**

Osteoporosis is defined as a systemic skeletal disorder characterized by low bone mass and micro-architectural deterioration of bone tissue, with a consequent increase in bone fragility and susceptibility to fracture (Fig.1.21).

The Bone Mineral Density (BMD) is the amount of bone mass per unit volume (volumetric density,  $\text{g}/\text{cm}^3$ ), that can be measured in vivo by densitometric techniques.

Because the BMD in the young healthy population is normally distributed [43] and the bone loss mainly occurs with advancing age, the prevalence of osteoporosis increases with age.

The prevalence of osteoporosis in the EU is estimated at 27.6 million in 2010 (22 million of women and 5.6 million of men) [44].

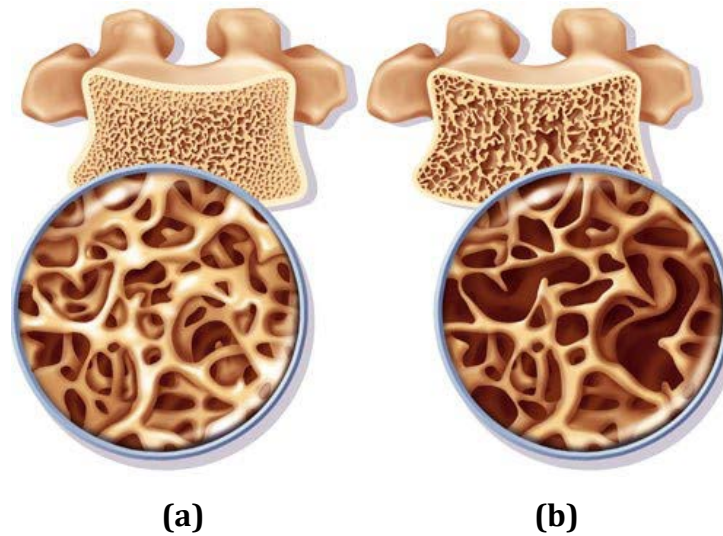


**Fig.1.21 - Vertebral body's trabecular structure: healthy bone (a) and osteoporotic bone (b)**

The description of osteoporosis captures the notion that low bone mass is an important component of the risk of fracture, but other abnormalities such as micro-architectural deterioration contribute to skeletal fragility.

Physical disability, advancing age and/or exposure to microgravity increase the risk of suffering from osteoporosis, and such disuse osteoporosis is associated with huge economic and health burden.

The bone loss, in general, refers to a reduction of bone mass in relation to bone volume, while the ratio of bone mineral to collagen remains unchanged. The loss of trabecular bone is more rapid and dramatic, while the cortical bone loss continues for a longer period [45].

The typical sites of osteoporosis fracture are hip, vertebra and wrist, but also humerus, ribs, tibia and fibula [46].

Among them, the osteoporotic vertebral fractures are associated with considerable reduction of quality of life, morbidity and mortality. Back pain in the majority of these patients is treated with prolonged bed-rest, local and systemic analgesia, and bracing. However, the extension of bed-rest in these patients results in increased bone loss, muscle weakness and joint stiffness [47].

A possible alternative is the vertebroplasty, a surgical procedure that involves the percutaneous injection of a bone cement into the fractured vertebral body, to provide mechanical support and relief from the pain. Vertebroplasty is considered

a minimally invasive surgical procedure because the procedure is performed through a small puncture in the patient's skin, instead of an open incision. A biopsy needle is guided into the fractured vertebra under X-ray guidance and a bone cement is injected directly into the fractured vertebra with the goal of creating a sort of internal cast. Then, the needle is removed and the cement hardens, stabilizing the bone (Fig.1.22).

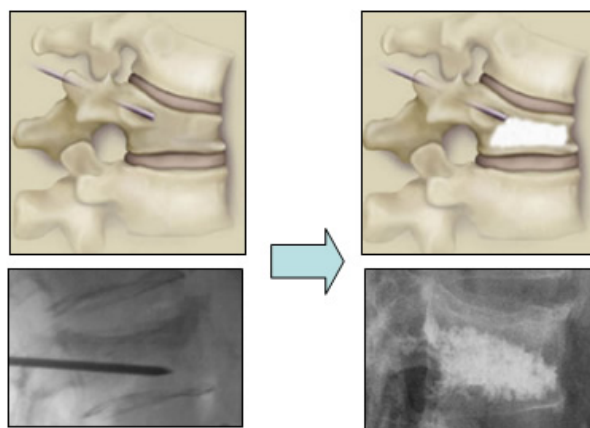


**Fig.1.22 - Vertebroplasty procedure**

### **1.3.2.3 Bone cements**

Injectable cements addressed to bone healing are a subject of major interest and intense investigation, as they can be delivered by minimal invasive surgery and, benefiting from the ability of self-hardening in situ, they may adequately stabilize bone defects. Particular interest is also addressed to vertebral fractures, due to trauma or osteoporosis-related bone weakening, mainly treated with vertebroplasty/kyphoplasty procedures since decades [48-52]. However, complete bone regeneration still remains an unsolved clinical need, mainly due to the lack of bone cements endowed with suitable bioactivity, osteoconductivity and bio-resorption ability.

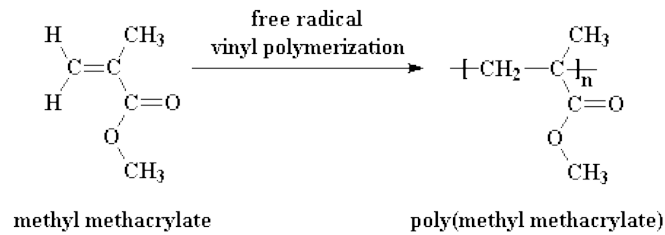
To date, two main categories of bone cements have been developed, based on polymers (especially acrylic formulations) and calcium phosphates.

#### **Acrylic Bone cements**

Poly(methylmethacrylate) (PMMA)-based bone cement, commonly known as acrylic bone cement, has been used for over 40 years, for fixation of total joint replacement prostheses to periprosthetic bone. The acrylic bone cements on the

market consist of two components: a liquid and a powder, which are mixed in the operating room until they become dough-like and then applied to stabilize a joint replacement prosthesis or directly injected into damaged vertebral bodies.

The basic component of acrylic bone cements is methylmethacrylate (MMA), which is an ester of methacrylic acid (Fig.1.23).

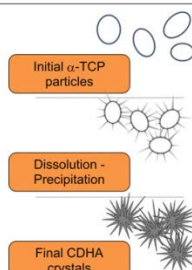
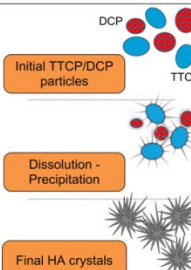
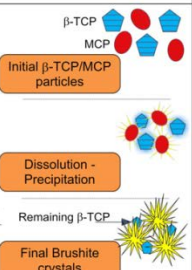
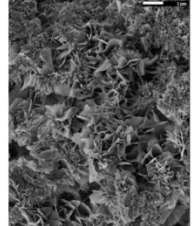
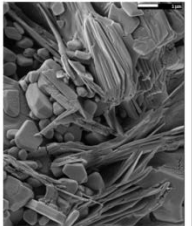


**Fig.1.23 - Polymerization reaction typical of PMMA-based cements**

### Calcium phosphate bone cements (CPCs)

Calcium phosphate cements (CPCs) were discovered in the 1980s by Brown and Chow [53] and LeGeros et al. [54]. The first commercial CPC products were introduced in the 1990s for treatment of maxillo-facial defects as well as for treatment of fractures. Since then, new cement formulations have been developed that fulfill specific requirements for other applications, such as bone augmentation, reinforcement of osteoporotic bones, fixation of metallic implants in weakened bone, spinal fractures and vertebroplasty.

CPCs are hydraulic cements. In general, CPCs are formed by a combination of one or more calcium orthophosphate powders, which upon mixing with a liquid phase, usually water or an aqueous solution, form a paste that is able to set and harden: the dissolution of the precursor powder via a hydraulic reaction and the precipitation of a thermodynamically more stable setting product occur. In this respect, unlike acrylic bone cements, which harden through a polymerization reaction, CPCs set as a result of a dissolution and precipitation process (Fig.1.24).

	Apatitic Cement		Brushitic Cement
	Single Component	Multiple Components	
Reactives	$\alpha$ -TCP	TTCP + DCPA/DCPD	$\beta$ -TCP + MCPM/MCPA
Reaction	$3\alpha\text{-Ca}_3(\text{PO}_4)_2 + \text{H}_2\text{O} \rightarrow \text{Ca}_9(\text{HPO}_4)_2(\text{PO}_4)_6(\text{OH})$	$2\text{Ca}_9(\text{PO}_4)_6\text{O} + 2\text{CaHPO}_4 \rightarrow \text{Ca}_{10}(\text{PO}_4)_6(\text{OH})_2$	$\beta\text{-Ca}_3(\text{PO}_4)_2 + \text{Ca}(\text{H}_2\text{PO}_4)_2 \cdot \text{H}_2\text{O} + 7\text{H}_2\text{O} \rightarrow 4\text{CaHPO}_4 \cdot 2\text{H}_2\text{O}$
Type of Reaction	Hydrolysis	Acid-Base	Acid-Base
Setting mechanism and crystal morphology			
SEM		<div style="display: flex; align-items: center; justify-content: center;"> <div style="writing-mode: vertical-rl; transform: rotate(180deg);">APATITE</div> <div style="writing-mode: vertical-rl; transform: rotate(180deg);">BRUSHITE</div> </div>	

**Fig.1.24 - Classification of calcium phosphate cements, with examples of the most common formulations [55].**

The entanglement of the precipitated crystals is responsible for cement hardening. Despite the large number of possible formulations, the CPCs developed up to now have only two different end products, precipitated hydroxyapatite (HA) or brushite (DCPD).

This in fact is a predictable situation since hydroxyapatite is the most stable calcium phosphate at  $\text{pH} > 4.2$  and brushite the most stable one at  $\text{pH} < 4.2$ .

When set, the apatitic CPCs consist of a network of calcium phosphate crystals, with a chemical composition and crystal size that can be tailored to closely resemble the biological hydroxyapatite occurring in living bone.

The CPCs leading to the formation of HA or calcium deficient HA (CDHA) can be classified in two main categories, which are summarized in Fig.1.25: 1) monocomponent CPCs, in which a single calcium phosphate compound, alpha tricalcium phosphate ( $\alpha$ -TCP) hydrolyses to CDHA without varying the Ca/P ratio, according to the reported chemical formula; 2) Multicomponent CPCs, in which two or more calcium phosphates, some more acidic and the other basic, set following an acid–base reaction.

### 1.3.2.4 Tricalcium phosphate (TCP)

The tricalcium phosphate ( $\text{Ca}_3(\text{PO}_4)_2$ ), bioresorbable material, exists in three different polymorphs: the low-temperature  $\beta$ -TCP, and the high-temperature forms,  $\alpha$ - and  $\alpha'$ -TCP. The last one lacks practical interest because it only exists at temperatures  $>1430^\circ\text{C}$  and reverts almost instantaneously to  $\alpha$ -TCP on cooling below the transition temperature. In contrast,  $\beta$ -TCP is stable at room temperature and transforms reconstructively at  $1125^\circ\text{C}$  to  $\alpha$ -TCP, which can be retained during cooling to room temperature [22].

Cell parameters (a, b, c,  $\alpha$ ,  $\beta$  and  $\gamma$ ), cell volume (V), number of formula units per cell (Z), volume per formula unit (V<sub>0</sub>), theoretical density (D<sub>th0</sub>) and the projections of the unit cells along the [0 0 1] direction are shown in Fig.1.25.

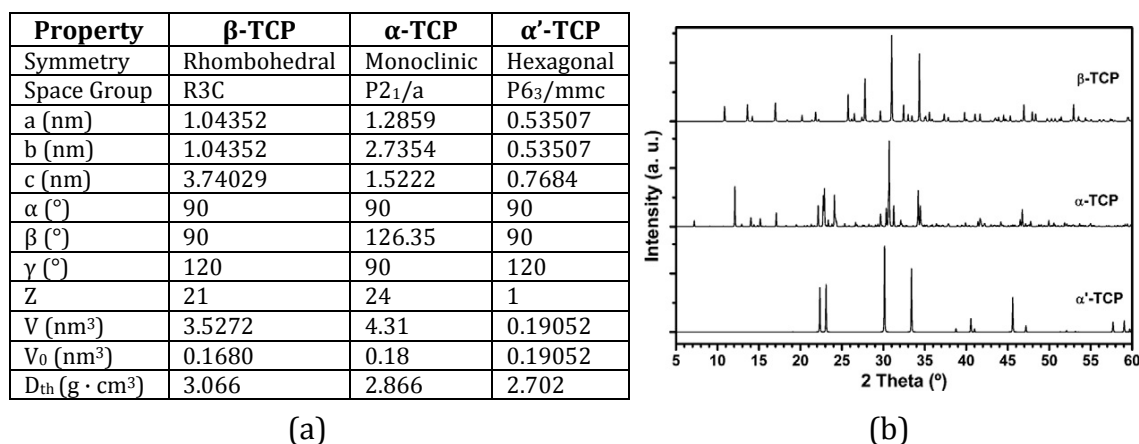


**Fig.1.25 - (a) Structural data of  $\alpha$ -TCP and its polymorphs. (b) calculated X-ray diffraction pattern of  $\alpha$ -TCP and its polymorphs [22]**

The difference in packing densities of the three polymorphs is consistent with thermodynamic considerations and with their stability temperature ranges.

The structural differences between  $\beta$ - and  $\alpha$ -polymorphs of TCP are responsible for their different chemical and biological properties, among them, solubility and biodegradability.

The  $\alpha$ -TCP is characterized by higher solubility than  $\beta$ -TCP, so that in aqueous solutions the dissolution of  $\alpha$ -TCP proceeds faster than  $\beta$ -TCP, as reported [56, 57].

$\beta$ -TCP is used mainly for preparing biodegradable bioceramics shaped as dense and macro-porous granules and blocks, whereas the more soluble and reactive  $\alpha$ -TCP is used mainly as a fine powder in the preparation of calcium phosphate

cements. Both  $\beta$ - and  $\alpha$ -TCP materials are used in clinics for bone repair and remodelling applications.

#### 1.4 References

- [1] Clarke B. Normal Bone Anatomy and Physiology. Clin J Am Soc Nephro. 2008;3:S131-S9.
- [2] Wegst UGK, Bai H, Saiz E, Tomsia AP, Ritchie RO. Bioinspired structural materials. Nat Mater. 2015;14:23-36.
- [3] Cowin SC. Bone Mechanics Handbook, Second Edition: Taylor & Francis; 2001.
- [4] Caetano-Lopes J, Canhao H, Fonseca JE. Osteoblasts and bone formation. Acta reumatologica portuguesa. 2007;32:103-10.
- [5] Mackie EJ. Osteoblasts: novel roles in orchestration of skeletal architecture. The international journal of biochemistry & cell biology. 2003;35:1301-5.
- [6] Boyle WJ, Simonet WS, Lacey DL. Osteoclast differentiation and activation. Nature. 2003;423:337-42.
- [7] Sims NA, Martin TJ. Coupling the activities of bone formation and resorption: a multitude of signals within the basic multicellular unit. BoneKEy reports. 2014;3:481.
- [8] Knothe Tate ML, Adamson JR, Tami AE, Bauer TW. The osteocyte. The international journal of biochemistry & cell biology. 2004;36:1-8.
- [9] Chen JH, Liu C, You L, Simmons CA. Boning up on Wolff's Law: mechanical regulation of the cells that make and maintain bone. Journal of biomechanics. 2010;43:108-18.
- [10] Frost HM. Bone Mass and the Mechanostat - a Proposal. Anatomical record. 1987;219:1-9.
- [11] Frost HM. Skeletal Structural Adaptations to Mechanical Usage (Satmu) .1. Redefining Wolff Law - the Bone Modeling Problem. Anatomical record. 1990;226:403-13.
- [12] Roberts WE, Huja S, Roberts JA. Bone modeling: biomechanics, molecular mechanisms, and clinical perspectives. Seminars in Orthodontics.10:123-61.
- [13] Ohba S, Yano F, Chung U-i. Tissue engineering of bone and cartilage. IBMS BoneKEy. 2009;6:405-19.
- [14] Dorozhkin SV. Calcium orthophosphates: occurrence, properties, biomineralization, pathological calcification and biomimetic applications. Biomatter. 2011;1:121-64.
- [15] Albee FH. Studies in Bone Growth: Triple Calcium Phosphate as a Stimulus to Osteogenesis. Annals of surgery. 1920;71:32-9.
- [16] Getter L, Bhaskar SN, Cutright DE, Perez B, Brady JM, Driskell TD, et al. Three biodegradable calcium phosphate slurry implants in bone. Journal of oral surgery. 1972;30:263-8.
- [17] Jarcho M, Kay JF, Gumaer KI, Doremus RH, Drobeck HP. Tissue, cellular and subcellular events at a bone-ceramic hydroxylapatite interface. J Bioeng. 1977;1:79-92.



- [18] Rejda BV, Peelen JG, de Groot K. Tri-calcium phosphate as a bone substitute. *J Bioeng.* 1977;1:93-7.
- [19] Roy DM, Linnehan SK. Hydroxyapatite formed from coral skeletal carbonate by hydrothermal exchange. *Nature.* 1974;247:220-2.
- [20] Brown WE, Chow LC. Dental restorative cement pastes. 1985.
- [21] Bohner M. Calcium orthophosphates in medicine: from ceramics to calcium phosphate cements. *Injury.* 2000;31:S37-S47.
- [22] Carrodegua RG, De Aza S. alpha-Tricalcium phosphate: synthesis, properties and biomedical applications. *Acta biomaterialia.* 2011;7:3536-46.
- [23] Corrigan JD, Selassie AW, Orman JA. The epidemiology of traumatic brain injury. *J Head Trauma Rehabil.* 2010;25:72-80.
- [24] Barker FG. Repairing Holes in the Head: A History of Cranioplasty. *Neurosurgery.* 1997;41:999.
- [25] Chaturvedi J, Botta R, Prabhuraj AR, Shukla D, Bhat DI, Devi BI. Complications of cranioplasty after decompressive craniectomy for traumatic brain injury. *British journal of neurosurgery.* 2015:1-5.
- [26] Zanaty M, Chalouhi N, Starke RM, Clark SW, Bovenzi CD, Saigh M, et al. Complications following cranioplasty: incidence and predictors in 348 cases. *Journal of neurosurgery.* 2015;123:182-8.
- [27] Tasiou A, Vagkopoulos K, Georgiadis I, Brotis AG, Gatos H, Fountas KN. Cranioplasty optimal timing in cases of decompressive craniectomy after severe head injury: a systematic literature review. *Interdisciplinary Neurosurgery.* 2014;1:107-11.
- [28] Staffa G, Barbanera A, Faiola A, Fricia M, Limoni P, Mottaran R, et al. Custom made bioceramic implants in complex and large cranial reconstruction: a two-year follow-up. *Journal of cranio-maxillo-facial surgery : official publication of the European Association for Cranio-Maxillo-Facial Surgery.* 2012;40:e65-70.
- [29] Staffa G, Nataloni A, Compagnone C, Servadei F. Custom made cranioplasty prostheses in porous hydroxy-apatite using 3D design techniques: 7 years experience in 25 patients. *Acta neurochirurgica.* 2007;149:161-70; discussion 70.
- [30] Colombo P. Materials science. In praise of pores. *Science.* 2008;322:381-3.
- [31] Deville S. Freeze-casting of porous ceramics: A review of current achievements and issues. *Adv Eng Mater.* 2008;10:155-69.
- [32] Messing GL, Stevenson AJ. Materials science. Toward pore-free ceramics. *Science.* 2008;322:383-4.
- [33] Ohji T, Fukushima M. Macro-porous ceramics: processing and properties. *Int Mater Rev.* 2012;57:115-31.
- [34] Studart AR, Gonzenbach UT, Tervoort E, Gauckler LJ. Processing routes to macroporous ceramics: A review. *J Am Ceram Soc.* 2006;89:1771-89.
- [35] Shackelford JF. *Bioceramics*: Taylor & Francis; 2003.
- [36] Dutta SR, Passi D, Singh P, Bhuihar A. Ceramic and non-ceramic hydroxyapatite as a bone graft material: a brief review. *Irish journal of medical science.* 2015;184:101-6.
- [37] Pepla E, Besharat LK, Palaia G, Tenore G, Migliau G. Nano-hydroxyapatite and its applications in preventive, restorative and regenerative dentistry: a review of literature. *Annali di stomatologia.* 2014;5:108-14.

- [38] Rivera-Muñoz EM. Hydroxyapatite-Based Materials: Synthesis and Characterization 2011.
- [39] Venkatesan J, Kim SK. Nano-hydroxyapatite composite biomaterials for bone tissue engineering--a review. *Journal of biomedical nanotechnology*. 2014;10:3124-40.
- [40] Liu Q, Huang SS, Matinlinna JP, Chen ZF, Pan HB. Insight into Biological Apatite: Physiochemical Properties and Preparation Approaches. *Biomed Res Int*. 2013.
- [41] Posner AS, Perloff A, Diorio AF. Refinement of the hydroxyapatite structure. *Acta Crystallographica*. 1958;11:308-9.
- [42] Elliott JC, Mackie PE, Young RA. Monoclinic hydroxyapatite. *Science*. 1973;180:1055-7.
- [43] Strom O, Borgstrom F, Sen SS, Boonen S, Haentjens P, Johnell O, et al. Cost-effectiveness of alendronate in the treatment of postmenopausal women in 9 European countries--an economic evaluation based on the fracture intervention trial. *Osteoporosis international : a journal established as result of cooperation between the European Foundation for Osteoporosis and the National Osteoporosis Foundation of the USA*. 2007;18:1047-61.
- [44] Hernlund E, Svedbom A, Ivergard M, Compston J, Cooper C, Stenmark J, et al. Osteoporosis in the European Union: medical management, epidemiology and economic burden. A report prepared in collaboration with the International Osteoporosis Foundation (IOF) and the European Federation of Pharmaceutical Industry Associations (EFPIA). *Archives of osteoporosis*. 2013;8:136.
- [45] Robling AG, Castillo AB, Turner CH. Biomechanical and molecular regulation of bone remodeling. *Annu Rev Biomed Eng*. 2006;8:455-98.
- [46] Kanis JA, Adachi JD, Cooper C, Clark P, Cummings SR, Diaz-Curiel M, et al. Standardising the descriptive epidemiology of osteoporosis: recommendations from the Epidemiology and Quality of Life Working Group of IOF. *Osteoporosis international : a journal established as result of cooperation between the European Foundation for Osteoporosis and the National Osteoporosis Foundation of the USA*. 2013;24:2763-4.
- [47] Dionyssiotis Y. Management of osteoporotic vertebral fractures. *Int J Gen Med*. 2010;3:167-71.
- [48] Böhner M. Calcium orthophosphates in medicine: from ceramics to calcium phosphate cements. *Injury*. 2000;31 Suppl 4:37-47.
- [49] Poitout DG. *Biomechanics and Biomaterials in Orthopedics*. 1st ed: Springer; 2004
- [50] Saint-Jean SJ, Camire CL, Nevsten P, Hansen S, Ginebra MP. Study of the reactivity and in vitro bioactivity of Sr-substituted alpha-TCP cements. *Journal of materials science Materials in medicine*. 2005;16:993-1001.
- [51] Watts NB, Harris ST, Genant HK. Treatment of painful osteoporotic vertebral fractures with percutaneous vertebroplasty or kyphoplasty. *Osteoporosis international : a journal established as result of cooperation between the European Foundation for Osteoporosis and the National Osteoporosis Foundation of the USA*. 2001;12:429-37.

- [52] Xue W, Dahlquist K, Banerjee A, Bandyopadhyay A, Bose S. Synthesis and characterization of tricalcium phosphate with Zn and Mg based dopants. *Journal of materials science Materials in medicine*. 2008;19:2669-77.
- [53] Brown WE, Chow LC. A new calcium phosphate water setting cement. *Cements research progress: Amer Cer Soc*; 1986. p. 352-79.
- [54] LeGeros R., Chohayeb A., Shulman A. Apatitic calcium phosphates: possible dental restorative materials. *Journal of dental research*. 1982;61.
- [55] Ginebra MP, Canal C, Espanol M, Pastorino D, Montufar EB. Calcium phosphate cements as drug delivery materials. *Advanced drug delivery reviews*. 2012;64:1090-110.
- [56] Chow LC. Calcium phosphate cements. *Monographs in oral science*. 2001;18:148-63.
- [57] Wang L, Nancollas GH. Calcium orthophosphates: crystallization and dissolution. *Chemical reviews*. 2008;108:4628-69.



# Chapter 2

## OVERVIEW OF METHODS

---

### 2.1 X-Ray Diffraction (XRD)

X-ray diffraction (XRD) is a non-destructive analytical technique primarily used for phase identification of a crystalline material. The material is finely ground, homogenized and the average bulk phase composition is analyzed.

XRD is based on constructive interference of monochromatic X-rays and the crystalline material. The X-rays are generated by a cathode ray tube, filtered to produce monochromatic radiation, collimated to concentrate and directed towards the sample.

The interaction of the incident X-rays with the sample produces constructive interference and a diffracted ray when the Bragg's law is satisfied (Fig.2.1).

Bragg's Law:

$$n \lambda = 2 d \sin (\theta)$$

where

$\lambda$  is the wavelength of the rays

$\theta$  is the angle between the incident rays and the surface of the crystal

$d$  is the spacing between layers of atoms

and constructive interference occurs when  $n$  is an integer (whole number)

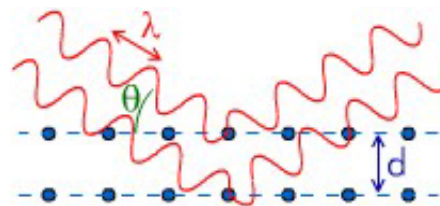
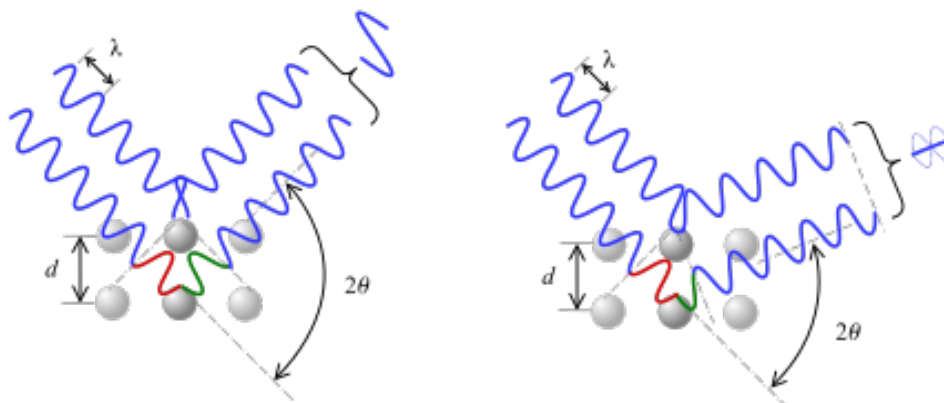


Fig.2.1 - Bragg's law and constructive interference

The phase composition of the material is investigated by comparing diffraction data against a database of Powder Diffraction Files (International Centre for Diffraction Data - ICDD).

When coupled with Rietveld refinement techniques, XRD may also provide structural information, such as unit cell dimensions and lattice strains.

The interaction of X-rays with atoms leads to the movement of the electronic cloud, with subsequent re-radiation waves with the same frequency, a phenomenon known as elastic scattering or Rayleigh scattering (Fig.2.2).



**Fig.2.2 - Constructive (left figure) or destructive (right figure) interference in Rayleigh scattering of X-rays.**

XRD data are usually presented in diffraction patterns (diffractograms), that is plots reporting diffracted peaks as function of the scattering angle  $2\theta$ , whenever a constructive interference between X-rays and the crystalline matrix of the material occurs.

Both the position of the peaks, corresponding to the lattice spacings and their relative intensity are indicative of a particular phase, providing a "fingerprint" for the material composition.

### **Crystal Structure**

Crystals are solids in which the atoms are regularly arranged. Such regularity of arrangement can be described in terms of symmetry elements, reflecting the symmetry of the physical properties of a crystal.

The crystal structure of a material is represented by its *unit cell*, quantitatively described by its lattice parameters, the length of the cell edges and the angles between them. The positions of the atoms inside the unit cell are described by the set of atomic positions  $(x_i, y_i, z_i)$  measured from a given lattice point.

The geometrical entities (points, axes or planes) with respect to which a lattice symmetry occurs are defined *symmetry elements*.

By using the symmetry elements it is possible to define the *symmetry operations*, namely the virtual motions of the smallest asymmetrical unit around a symmetrical center.

Complex symmetry operations lead to *space groups*, the most detailed level to describe the symmetry properties of the crystal, such as cleavage, electronic band structure and optical properties.

Although there are an infinite number of ways to specify a unit cell, for each crystal structure there is a conventional unit cell, which is chosen to display the full symmetry of the crystal. However, the conventional unit cell is not always the smallest possible choice.

A *primitive unit cell* of a particular crystal structure is the smallest volume completely filled by stacked atoms.

In a unit cell each atom has an identical arrangement of the neighboring atoms, while in a primitive cell each atom may also have different local atoms arrangements. The crystal structure consists of the same group of atoms, the basis, positioned around each and every lattice point. This group of atoms therefore repeats indefinitely in three dimensions according to the arrangement of one of the 14 Bravais lattices (Fig.2.3).

The possible lattice centring are:

- P: Primitive centring, lattice points on the cell corners only;
- I: Body centred, one additional lattice point at the center of the cell;
- F: Face centred, one additional lattice point at centre of each of the faces of the cell;
- C: Centred on a single face, one additional lattice point at the centre of one of the cell faces



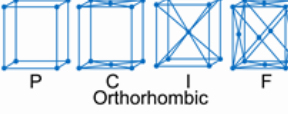




 <p>Cubic P    Cubic I    Cubic F</p>	<p>Three axes at right angles; all equal: <math>a = b = c; \alpha = \beta = \gamma = 90^\circ</math></p>
 <p>Tetragonal P    Tetragonal I</p>	<p>Three axes at right angles; two equal: <math>a = b \neq c; \alpha = \beta = \gamma = 90^\circ</math></p>
 <p>P    C    I    F Orthorhombic</p>	<p>Three axes at right angles; all unequal: <math>a \neq b \neq c; \alpha = \beta = \gamma = 90^\circ</math></p>
 <p>Monoclinic P    Monoclinic C</p>	<p>Three axes, one pair not at right angles, all unequal: <math>a \neq b \neq c; \alpha = \gamma = 90^\circ \neq \beta</math></p>
 <p>Triclinic P</p>	<p>Three axes not at right angles; all unequal: <math>a \neq b \neq c; \alpha \neq \beta \neq \gamma \neq 90^\circ</math></p>
 <p>Rhombohedral</p>	<p>Three axes equally inclined, not at right angles; all equal: <math>a = b = c; \alpha = \beta = \gamma \neq 90^\circ</math></p>
 <p>Hexagonal</p>	<p>Three axes coplanar at <math>120^\circ</math>, fourth axis at right angles to these: <math>a_1 = a_2 = a_3 \neq c</math>; <math>\alpha = \beta = 90^\circ, \gamma = 120^\circ</math></p>

Fig.2.3 – The 7 crystalline systems and the 14 Bravais lattices

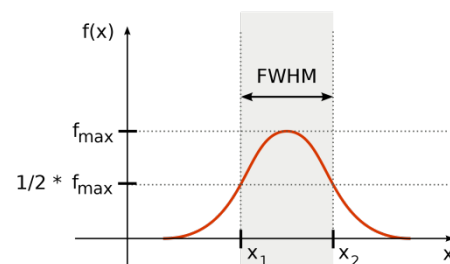
### Miller indices

The Miller indices are useful notation tools in crystallography to identify the different planes and direction of a Bravais lattice. A reticular plane is identified by three integers  $h, k, l$ , the Miller indices, reported as  $(hkl)$ . Such indices are vectors, reciprocals of the intercepts of the plane on the axes  $x, y, z$ .

### Size and Strain Broadening

The width of a diffraction peak,  $B$ , is related to several factors, including:

1. instrumental factors
2. the presence of lattice defects
3. strain dishomogeneity among the grains
4. the size of the crystallites





Analysis of XRD peak profiles indicated that full-width at half-maximum (FWHM) is sensitive to the variation in microstructure and stress-strain accumulation in the material.

Presence of tensile stress in the material causes increase in the FWHM while relaxation of tensile stress decreases FWHM.

The Scherrer equation [1] can be used to estimate the size of the crystallite

$$B(2\theta) = \frac{K\lambda}{D \cos \theta}$$

where  $B$  is the peak width corrected for the instrumental broadening,  $\theta$  is the diffraction angle,  $K$  is a form factor, usually taken as 0.9,  $\lambda$  is the wavelength of the incident radiation and  $D$  is the crystallite average size.

### Diffractometer

X-ray diffractometers consist of three basic elements: an X-ray tube, a sample holder, and an X-ray detector. X-rays are generated in a cathode ray tube by heating a filament to produce electrons, accelerating the electrons toward a target by applying a voltage, and bombarding the target material with electrons (Fig.2.4).

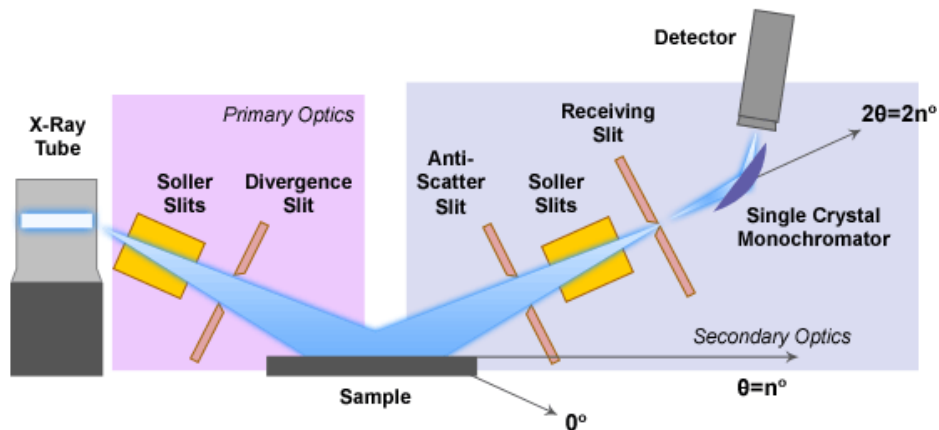


Fig.2.4 - Typical scheme of a Bragg-Brentano type diffractometer

The model of diffractometer employed in this activity is a D8 Advance diffractometer (CuK $\alpha$  radiation) working with Bragg-Brentano configuration, equipped with a LINXEYE detector (Bruker, Karlsruhe, Germany). The XRD patterns were recorded in the  $2\theta$  range  $10^\circ$ - $80^\circ$ , scan step  $0.02^\circ$  and step time 0.5

seconds. The lattice parameters refinement was performed according to the Rietveld method (TOPAS 4.2 software).

## 2.2 Scanning Electron Microscopy (SEM)

The scanning electron microscope is a device able to provide high magnification images of a sample (up to 200000x) with both resolution and field depth higher than the conventional optical microscope.

The image is obtained by “exploring” the surface of the sample with a high energy electron beam, while a real-time monitoring of the intensity of the emitted secondary electrons is performed.

After focusing the high-energy beam of electrons onto the surface of a sample, several signals are detected from the interaction of the incident electrons with the sample's surface (Fig.2.5)

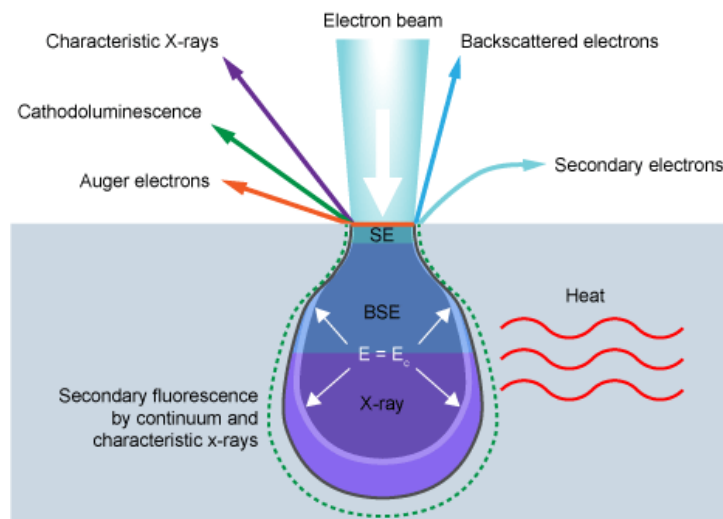


**Fig.2.5 – Electron-matter interaction**

Part of the incident electron beam (primary electrons) is reflected without decreasing the initial energy, giving rise to *backscattered electrons*.

The primary electrons which are not reflected transfer their energy to some of the electrons of the samples, making them able to diffuse towards the surface and escape outside of the sample with a low energy (energy < 50 eV), the so-called *secondary electrons*.

Furthermore, characteristic x-ray photons are emitted when the primary beam causes the ejection of inner shell electrons from the sample and are used to investigate the elemental composition of the sample. The back-scattered electrons emitted from the sample may be used alone to form an image or in conjunction with the characteristic x-rays as atomic number contrast clues to the elemental composition of the sample.

In a typical SEM, thermo-ionic electrons are emitted from a tungsten cathode (electron gun) and accelerated towards an anode (Fig.2.6)

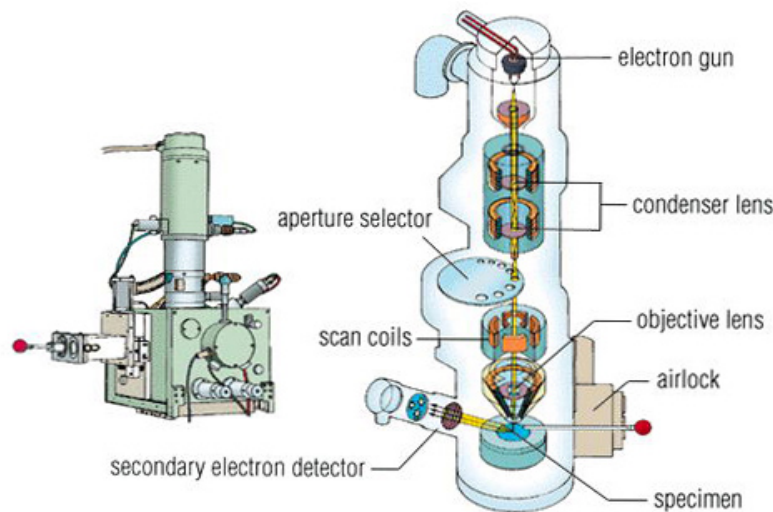


**Fig.2.6 – Structure of a SEM**

Tungsten is used because of its high melting point and low vapour pressure. The electron beam, which typically has an energy ranging from a few hundred eV to 100 keV, is focused by condenser lenses into a beam with a very fine focal spot sized 0.4 nm to 5 nm. The beam passes through pairs of scanning coils or pairs of deflector plates in the electron optical column, typically in the objective lens, which deflect the beam to scan the surface of the sample.

The interaction volume depends on the electron beam energy, the atomic number of the specimen and the specimen's density.

The secondary electrons, due to their low energy, are detected by a scintillator-photomultiplier device and the resulting signal is rendered into a two-dimensional intensity distribution that can be viewed and saved as a digital image. The

brightness of the signal depends on the number of secondary electrons reaching the detector.

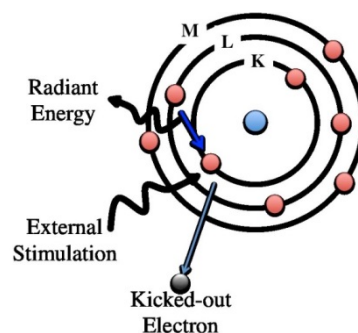
The spatial resolution of the SEM depends on the size of the electron spot, which in turn depends on both the wavelength of the electrons and the magnetic electron-optical system which produces the scanning beam.

The equipment employed in the present work is a FEI, Quanta 200, USA.

### **Energy dispersive X-ray spectroscopy (EDS)**

Energy dispersive X-ray spectroscopy is a technique that detects the x-ray fluorescence to characterize the elements present in a material.

If a sample is excited under high energy of electron beam or other electromagnetic radiation, the inner shell of electrons is ejected to vacuum creating a vacancy in that shell (figure aside).



Electrons from the outer shell jump into the vacant site for filling the inner shell. During this process (radiant energy), the sample fluoresces X-ray of energy same as the energy difference between the initial state and final state. Since each atom has its unique and discretized energy levels, the X-ray fluorescence is also characteristic of that atom.

SiLi detectors operating at liquid nitrogen temperature are commonly used in EDS experiments (Fig.2.7): striking the detector, the X-rays produce photoelectrons which in turn produces electron-hole pairs within the Si. These migrate to opposite ends of the detectors (via an applied electric field of 1.5 kV) producing a current pulse whose size is proportional to the energy of the incident X-Ray.

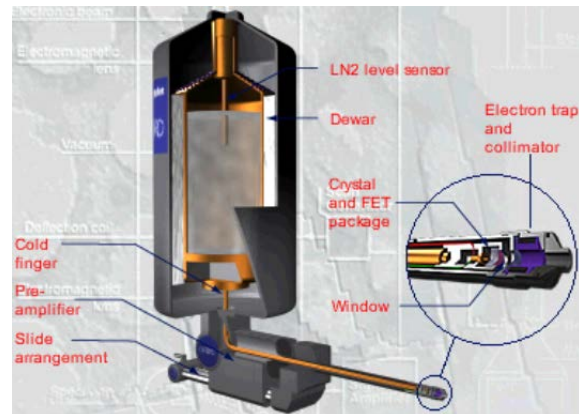


**Fig.2.7 – Schematic view of and EDS device**

### **2.3 Inductively Coupled Plasma Optical Emission Spectroscopy**

The Inductively Coupled Plasma Optical Emission Spectroscopy (ICP-OES) is one of the most powerful and popular analytical tools for the determination of trace elements [2].

The technique is based upon the spontaneous emission of photons from atoms and ions that have been excited in a radiofrequency (RF) discharge. Liquid and gas samples may be directly injected into the instrument, while solid samples require extraction or acid digestion so that the analytes will be present in a solution. The intensity of the radiation is proportional to the concentration of the element, which is obtained through a previous calibration obtained with opportune standard solutions.

An inductively coupled plasma for spectrometry is sustained in a torch that consists of three concentric tubes, usually made of quartz. The end of this torch is placed inside an induction coil supplied with a radio-frequency electric current. A flow of argon gas is introduced between the two outermost tubes of the torch and an electrical spark is applied for a short time to introduce free electrons into the gas stream (Fig.2.8).

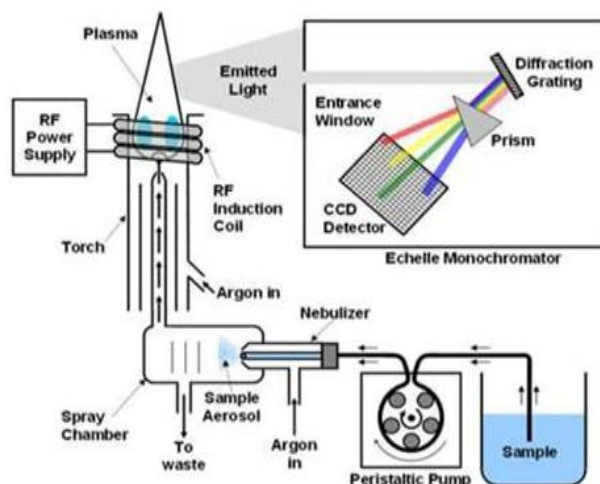


Fig.2.8 – Schematic view of an ICP-OES instrument

The sample solution is converted to an aerosol and directed into the central channel of the plasma. At its core the inductively coupled plasma (ICP) sustains a temperature of approximately 10000K, so that the aerosol is quickly vaporized. Analyte elements are liberated as free atoms in the gaseous state. Further collisional excitation within the plasma imparts additional energy to the atoms, promoting them to excited states. Sufficient energy is often available to convert the atoms to ions and subsequently promote the ions to excited states. Both the atomic and ionic excited species may then relax to the ground state via the emission of photons. These photons have characteristic energies that are determined by the quantized energy level structure for the atoms or ions. Thus, the wavelength of the photons can be used to identify the elements from which they originated. The total number of photons is directly proportional to the concentration of the originating element in the sample.

#### 2.4 Specific Surface Area

The ceramic manufacturing is strictly related to several parameters, with particular regard to the size, shape and specific surface area (SSA) of the powders. Ideally, assuming that a powder is composed by small spherical particles provided with the same diameter, the specific surface area ( $\text{m}^2/\text{g}$ ) of the powder,  $S$ , can be

calculated by multiplying the surface area of each particle and  $n$ , the number of the particles per weight unit ( $S = 4\pi r^2 n$ ).

Actually, the size and shape of the powder particles are really irregular and unexpected, so that it is not possible to define a simple model of the surface area.

In this case, the measurement of SSA is indirectly measured by the adsorption of a gas on the outer surface of the particles.

Two different adsorption processes can be described: a *physical* and a *chemical* adsorption. The main difference relates to the interactions forces involved in the adsorption of the gas: the first one is characterized by weak Van der Waals and electrostatic forces, while the latter includes also stronger chemical bonds.

For that reason, a physical adsorption is considered the easier way to determine SSA, as a reversible process (desorption) can be adopted to quantify the adsorbed gas.

### B.E.T. Equation

The scientists Stephen Brunauer, Paul Hugh Emmett and Edward Teller published in 1938 [3] a theory to describe the multilayer adsorption phenomena as an extension of the Langmuir theory [4]. Three main postulates were proposed:

- 1) gas molecules physically adsorb on a solid in layers infinitely
- 2) there is no interaction between each adsorption layer
- 3) the Langmuir theory can be applied to each layer

The resulting BET equation is

$$\frac{p}{V_{ads}(p^0-p)} = \frac{(C-1)}{V_m C} \frac{p}{p^0} + \frac{1}{V_m C}$$

where  $V_{ads}$  is the adsorbed gas quantity,  $V_m$  is the monolayer adsorbed gas quantity,  $p$  is the equilibrium pressure of the adsorbates at the temperature of adsorption,  $p^0$  is the saturation pressure of the adsorbates at the temperature of adsorption and  $C$  is the BET constant, related to the net adsorption energy.

For a given gas, the terms  $V_m$  and  $C$  are constants, so that the equation can be simplified as

$$\frac{p}{V_{ads}(p^0-p)} = \alpha \frac{p}{p^0} + \beta$$

$$\alpha = \frac{(C-1)}{V_m C} \quad \beta = \frac{1}{V_m C}$$

resulting in the equation of a line,  $y=\alpha x+\beta$ , especially in the relative pressure range 0.05-0.30. Once derived the  $\alpha$  and  $\beta$  coefficients,  $V_m$  is determined as  $1/(\alpha+\beta)$ .

The total surface area of the adsorbed gas,  $S$ , is determined by multiplying  $V_m$  and  $S_0$ , the area correspondent to  $1 \text{ cm}^3$  of an adsorbed gas monolayer ( $S = V_m \cdot S_0$ ).

Finally, SSA is determined by dividing  $S$  and  $W$ , the sample weight.

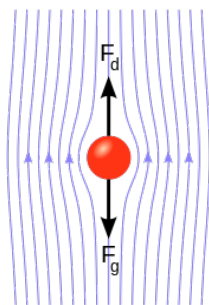
### Analytical Technique

The sample holder is immersed in liquid nitrogen to enable the adsorption process. After few minutes, the gas stabilization occurs and the adsorption process is quantified. Then, the desorption process is forced by substituting the liquid nitrogen with a room temperature water bath; in this condition, the previously adsorbed nitrogen is released. Ideally, the gas adsorption is completely reversible and the desorption is equivalent to the adsorption.

In this activity, the MICROMERITICS FlowSorb II 2300 instrument was used.

## 2.5 Particle Size Distribution

The creeping flow past a falling sphere in a fluid involves three different forces:



$F_G$  = force by gravity

$F_A$  = hydrostatic force (Archimede's principle)

$F_D$  = drag force, that is the fluid frictional force

In equilibrium conditions, the resultant force is null ( $F_G + F_A + F_D = 0$ ).

A more rigorous equation describing the particle's motion is:

$$mg - m^o g - F = m^o \frac{dv}{dt}$$

where  $m$  is the particle's mass,  $m^o$  is the mass of the volume of the liquid equals to the volume of the particle,  $g$  is the force by gravity,  $F$  is the drag force,  $v$  the particle's velocity and  $t$  the time.



Empirically, the higher the fluid viscosity, the slower the motion of a particle and the smaller the particles, the quicker the velocity variations, so that  $dv/dt$  becomes rapidly null.

The motion equation of a sphere with diameter  $D$  and density  $\rho$ , in a fluid with density  $\rho^\circ$  is:

$$F = \frac{\pi}{6} (\rho - \rho^\circ) g D^3$$

The stable motion of a spherical particle in a fluid is given by two adimensional parameters: the Reynolds number (Re) and a frictional coefficient (C).

$$\text{Re} = Dv \frac{\rho^\circ}{\eta} \quad C = \frac{F}{(\pi D^2/4)(\rho^\circ V^2/2)}$$

Finally, the Stoke's law is obtained by considering a laminar flux ( $C \cdot \text{Re} \approx 24$ ),

$$D^2 = \frac{18 v \eta}{(\rho - \rho^\circ) g}$$

### **Sedimentation Theory**

The analysis of the sedimentation is related to the dependence of the velocity of a particle in a fluid with the size of the particle, according to Stoke's law: the bigger the particle, the higher the velocity.

In this respect, to accurately evaluate the particles diameter by using the falling velocity, is necessary to know the density and the viscosity of the fluid, together with the density of the particles.

### **Analytical Technique**

Given the characteristic parameters of the fluid, the falling velocity of different size particles is theoretically evaluated before the analysis, according to Stoke's law: based on the real-time sedimentation, the height of the sample cell can be associated with a particle radius equal to or less than that determined by solving the Stoke's law.

After the calibration of the instrument with sodium esametaphosphate in aqueous solution (0.05 wt%), the specimen particles are then dispersed in a similar fluid, which is then sonicated to avoid the formation of aggregates and pumped in the sample cell (Fig.2.9)

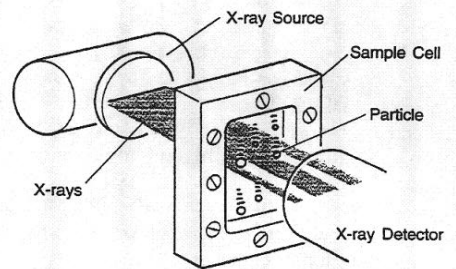


**Fig.2.9 - Detail of the sample cell during the analysis**

The size distribution of the particles is monitored by the intensity of the detected X-rays at the different height of the sample cell during sedimentation by gravity. Finally, a plot of the cumulative mass percentage vs particle diameter is obtained. In this activity, the MICROMERITICS SediGraph 5100 instrument was used.

## **2.6 Rheology of suspensions**

The rheology is the study of flow and deformation of materials under applied forces, which is routinely measured using a rheometer.

The rheological behavior of ceramic suspensions mainly depends on the content of solid particles, the particle size distribution and the degree of agglomeration [5].

At very low shear, the elementary solid particles group themselves in aggregates that may form a 3-D network involving the whole volume of suspension. This network imparts elastic properties to suspension and is responsible for apparent yield stress.

With increasing the shear rate, the network breaks into aggregates whose size continuously decreases. The size and spatial arrangement of aggregates depends on the shear rate. Such microstructural changes, induced by the shear rate increase, may produce changes in the viscosity.

At higher shear rate, aggregates break down in primary flocs. The agglomeration and breaking kinetics are not instantaneous, so that the rheological properties change with time, giving rise to thixotropic phenomena.

These agglomeration phenomena are mainly related to Brownian, hydrodynamic, and interparticle (attractive or repulsive) forces.

Van der Waals attraction forces between primary flocs is the major force responsible for flocculation. Often, a steric stabilization is necessary to avoid agglomeration by the addition of proper amount of effective dispersant (polymers), which is adsorbed on the particle surfaces.

The characterization of the rheological behavior of calcium phosphate suspensions is a useful tool in the perspective of customization of the final performance of the scaffolds.

### Viscosity and Dynamic mechanical analysis

The viscosity is the property of a fluid describing its resistance to flow. When a force,  $F$ , is applied to a volume of material by two plates separated by distance  $d$ , then a displacement (deformation) occurs.

The proportionality constant between the shear stress (force divided by area parallel to the force) and the shear strain rate (displacement divided by the product between the plates separation distance and the time) is known as dynamic viscosity,  $\eta$  (Fig.2.10).

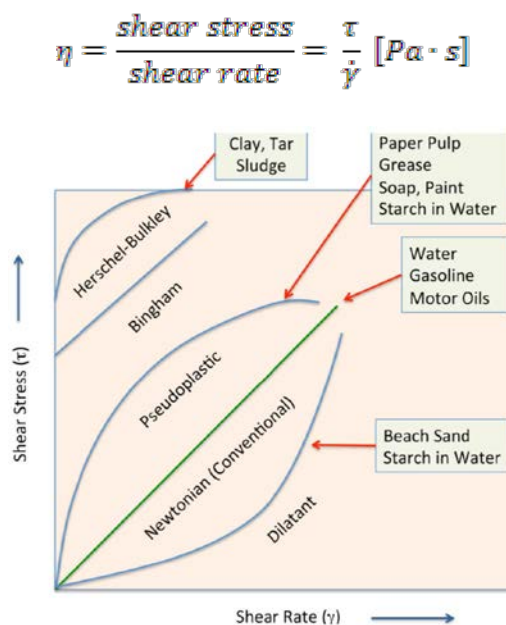
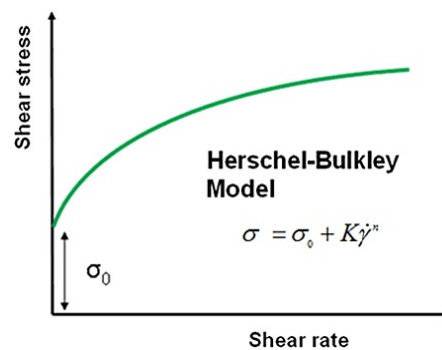


Fig.2.10 – Shear stress-Shear rate diagrams

The rheological behaviour of ceramic ink formulations for 3D printing was evaluated by Discovery HR1 (Hybrid Rheometer, TA Instruments) with a parallel Peltier plate system (plate diameter = 40mm; gap = 1000 $\mu$ m). The shear stress and the viscosity of each suspension were evaluated with increasing the shear rate from 0.01 to 100.

The dynamic mechanical properties of the materials (storage modulus, loss modulus and yield stress) were also evaluated with increasing the shear stress from 1 to 100 Pa at frequency equals to 1 Hz. The storage modulus ( $G'$ ) measures the material's ability to store elastic energy, while the loss modulus ( $G''$ ) is related to the dissipated energy. The yield stress is the stress value above which a high viscosity material flows like a liquid. The yield stress was estimated by calculating the shear stress at zero shear rate (Fig.2.11), according to the Herschel-Bulkley model [6]. The viscosity was calculated by imposing a constant shear rate typically experienced during printing ( $\dot{\gamma} = 50s^{-1}$ ) [7].



**Fig.2.11 - Schematic representation of the yield stress,  $\sigma_0$ , according to the Herschel-Bulkley model**

## 2.7 Thermogravimetric analysis (TGA)

The Thermogravimetric analysis is a useful test to determine changes in weight in relation to change in temperature. Such analysis relies on a high degree of precision in three measurements: weight, temperature, and temperature change. As many weight loss curves look similar, the weight loss curve may require transformation before results may be interpreted. A derivative weight loss curve can be used to tell the point at which weight loss is most apparent.

The analyzer usually consists of a high-precision balance with a pan loaded with the sample. The sample is placed in a small electrically heated oven with a thermocouple to accurately measure the temperature. The atmosphere may be purged with an inert gas to prevent oxidation or other undesired reactions. A computer is used to control the instrument.

Analysis is carried out by raising the temperature gradually and plotting weight against temperature. After the data is obtained, curve smoothing and other operations may be done such as to find the exact points of inflection.

In this activity, the Simultaneous Thermal Analyser (STA 409C, Netsch, Germany) was used.

## 2.8 Zeta Potential

Zeta potential ( $\xi$ ) is a physical property exhibited by any particle in suspension. It is a measure of the magnitude of the electrostatic or charge repulsion/attraction between particles, thus describing the causes of dispersion, aggregation or flocculation of particles.

The shear plane, or slipping plane, is the limit of a region around the particle surface consisting of a tightly bound electrical double layer of ions and solvent molecules. The zeta potential is defined as the difference in potential between the surface of the shear plane of particles and the electroneutral region of the solution (Fig.2.12).

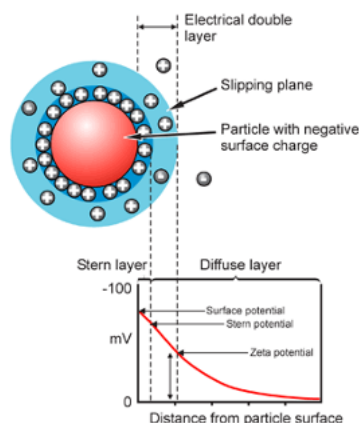


Fig. 2.12 – Zeta potential scheme

In this research activity, the zeta potential titration of colloidal ink formulations for 3D printing was performed by electroacoustic phenomena (Zetasizer Nano ZSP, Malvern, UK). A more acidic pH was achieved by adding 0.2 ml of HCl 1M, while basic pH was achieved by adding 0.2 ml of NaOH 1M.

## 2.9 Mercury porosimetry

The physical properties of materials are greatly affected by porosity. The term porosimetry refers to the analytical technique used to measure the pore size distribution of a material.

Mercury intrusion porosimetry is based on the premise that a nonwetting liquid (contact angle  $> 90^\circ$ ) will intrude capillaries only under pressure (Fig.2.13).

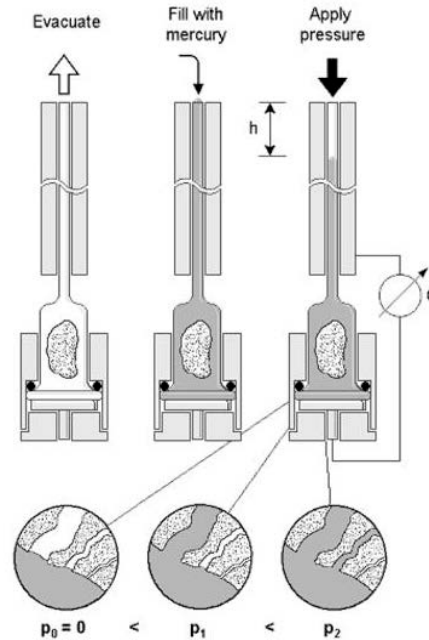


Fig.2.13 – Schematic view of a mercury porosimeter

The relationship between the pressure and capillary diameter was described by Washburn [8] as:

$$P = \frac{-4 \cdot \gamma \cdot \cos \theta}{d}$$

where  $P$  is the pressure,  $\gamma$  is the surface tension of the liquid,  $\theta$  is the contact angle of the liquid and  $d$  is the diameter of the capillary.

The pressure required for the infiltration is inversely proportional to the size of the pores, so that only low pressures are required to intrude mercury into large macropores, whereas much greater pressures are required to force mercury into small pores.

The pore size distribution is determined from the volume intruded at each pressure increment, while the total porosity is determined from the total volume intruded.

In this activity, the pore volume and pore size distributions were evaluated by mercury intrusion porosimetry (surface tension = 0.48 N/m and contact angle = 140°, Hg pressure in the range 0-200 Pa, Thermo Scientific Surfer). The measurement error is related to the accuracy of Hg intrusion porosimetry (<4%).

## 2.10 Mechanical characterization

### 2.10.1 Compression

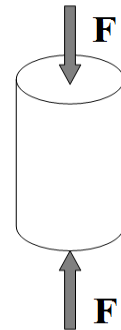
The strength of ceramics materials is mainly characterized by compressive tests, because of the intrinsic micron-size defects that can be easily extended during a tensile stress, affecting the measurement.

For that reason, the compressive strength of ceramics is generally higher than their tensile strength. A compressive test of a specimen involves a system of converging forces which tends to reduce its size (figure aside).

Ideally, the force is homogeneously distributed on the whole surface of the specimen sections, so that dividing the force,  $F$ , by the cross-sectional area,  $A$ , the average value of the compressive stress,  $\sigma$ , can be obtained.

A uniform distribution of the normal stress can be assumed in axially loaded specimens, with the exception of the local areas of application of the loads.

The compressive strength was evaluated after obtaining the planarity of the endplates by using an automatic surface grinder (VAM Rettificatrici, Italy). The tests were performed in displacement control at 0.5 mm/min, by collecting data at 20 Hz with a universal testing machine (MTS Insight 5, Minnesota, USA).



### 2.10.2 Flexure (4-point bending)

The flexural strength is a material property defined as the stress in a material just before it yields in a flexure test. The flexural strength would be the same as the tensile strength if the material were homogeneous; in fact, most materials have small or large defects which act as local stress concentrators, effectively causing a localized weakness.

Ceramics are usually very brittle, and their flexural strength depends on both their inherent toughness and the size and severity of flaws.

In this activity, the flexural strength was calculated by 4-point bending tests: a loading force is applied by means of two loading pins with a distance between them equal to a half of the distance between the supporting pins (Fig.2.14).

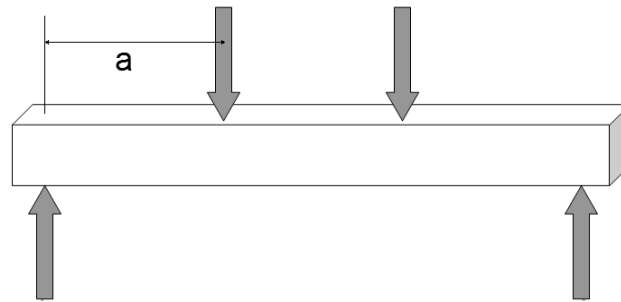


**Fig.2.14 - scheme of the 4-point bending test**

It should be noted that no specific reference standards are given for 4-point bending tests of macroporous ceramic materials, so that only some indications were adopted (ASTM C1341-00: Standard Test Method for Flexural Properties of Continuous Fiber Reinforced Advanced Ceramic Composites).

The flexural strength was determined by testing parallelepiped specimens (100mm x 20mm x 14mm) for each condition. The planarity of the endplates was obtained by using an automatic surface grinder (VAM Rettificatrici, Italy). The tests were performed in displacement control at 0.5 mm/min, by collecting data at 20 Hz with a universal testing machine (MTS Insight 5, Minnesota, USA).

The resultant state of stress in flexural testing is reported in Fig.2.15.



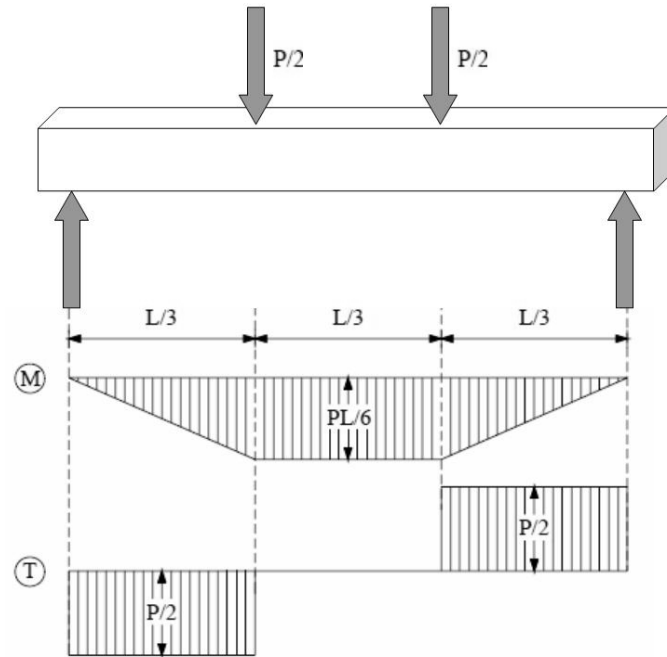


Fig.2.15 - Shear force and bending moment distribution during a 4-point bending test

Despite a stress concentration is assumed to be locally present at the loading points, the region of the specimen between the upper pins is characterized by a uniform bending moment and null shear stress, leading to pure bending loading ( $PL/6$ ) in the central part of the specimen.

Once derived the fracture load,  $P_N$ , the flexural strength is given by:

$$\sigma = \frac{3 \cdot P_N \cdot a}{b \cdot d^2}$$

where  $b$  and  $d$  represent the weight and the height of the specimens, respectively.

For each test, the deformation  $\varepsilon$  has been evaluated on displacement control,  $\delta$ , according to:

$$\varepsilon = \frac{6 \cdot \delta \cdot d}{L^2}$$

## 2.11 Design of Experiments

In general, the outputs of forming processes are affected by controllable inputs as well as a complex interaction of controllable and uncontrollable factors (Fig.2.16).

Such factors may be discrete, such as different machines or operators, or continuous such as ambient temperature or humidity.

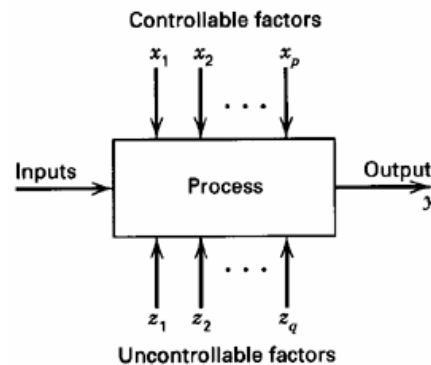


Fig.2.16 – Controllable and uncontrollable factors affecting the processes

The conventional approaches to investigate the effect of process parameters involve the single factor variation (One Factor At a Time), that is only one factor or variable at a time is changed while keeping others fixed. However, experiments designed according to rational statistical methodologies, including the simultaneous variation of several factors, are more efficient when studying two or more factors (Fig.2.17).

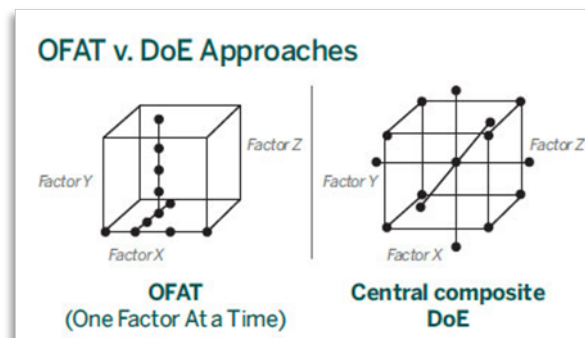


Fig.2.17 – Schematic representation of One Factor At a Time vs Design of Experiments approaches

The design of experiments (DoE) is a powerful statistical tool to investigate the effects of the variation of one or more factors on the final output of the system.

Nowadays, the DoE approach is adopted by a lot of companies in order to speed up the development of new products and processes, as well as to optimize the existing forming routes. The correct implementation of DoE may lead to decreased time to

market and production costs, while improving both quality and reliability of the products.

The DoE allows practitioners to explicitly model the relationships among the numerous variables of systems, enabling decisions at each stage of the problem-solving process .

In material science for ceramics, the optimization of forming processes with DoE is still its infancy. Such rational approach may elucidate the role of the myriad of process parameters typically involved in the ceramic manufacturing.

A thorough control of variables is particularly requested for the preparation of biomaterials, where a simultaneous customization of compositional, morphological and mechanical features is requested to meet the clinical needs.

The advantages of DoE approach can be summarized as follows:

- It requires less resources (experiments, time, material, etc.) for the amount of information obtained. This can be of major importance in industry, where experiments can be very expensive and time consuming.
- The estimates of the effects of each factor are more precise. Using more observations to estimate an effect results in higher precision (reduced variability)
- The interaction between factors can be estimated systematically. Interactions are not estimable from OFAT experiments.
- There is experimental information in a larger region of the factor space. This improves the prediction of the response in the factor space by reducing the variability of the estimates of the response in the factor space, and makes process optimization more efficient because the optimal solution is searched for over the entire factor space

A useful tool to investigate the effect of the variation of three parameters is the Central Composite Design (CCD) (Fig.2.18).

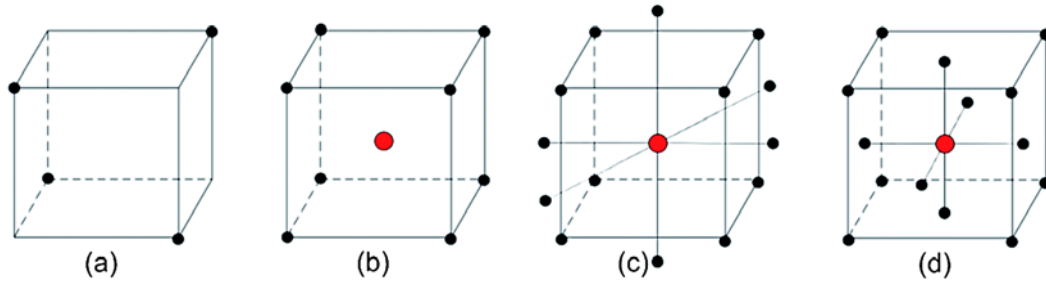


**Fig.2.18 – Experimental designs. (a) Half-fractional  $2^3$  factorial; (b) full  $2^3$  factorial with center point; (c) central composite design; (d) face-centered central composite design.**

In this activity, the Face-Centered Central Composite Design with five center points was adopted: the number of experiments required for the FCCD scheme is given by  $n = 2^k + 2k + c$ , where  $k$  is the number of factors and  $c$  is the number of center points [9, 10]. Because it is generally extremely difficult to eliminate bias using only their expert judgment, the use of randomization in experiments is common practice. A regression analysis of data was also performed, according to the following second-order polynomial equation:

$$y = \beta_0 + \sum \beta_i x_i + \sum_{i < j} \beta_{ij} x_i x_j + \sum \beta_{ii} x_i^2$$

where  $y$  is the response,  $x_i$  and  $x_j$  are the coded factor levels and  $\beta_0$ ,  $\beta_i$ ,  $\beta_{ii}$  and  $\beta_{ij}$  are the mean values of constant, linear, quadratic and interaction coefficient, respectively.

The influence of the factors was investigated by contour plots and Pareto charts from the regression analysis, using the MATLAB software.

## 2.12 References

- [1] Scherrer P. Bestimmung der inneren Struktur und der Größe von Kolloidteilchen mittels Röntgenstrahlen. *Kolloidchemie Ein Lehrbuch*: Springer Berlin Heidelberg; 1912. p. 387-409.
- [2] Hou X, Jones BT. Inductively Coupled Plasma/Optical Emission Spectrometry. *Encyclopedia of Analytical Chemistry*: John Wiley & Sons, Ltd; 2006.
- [3] Brunauer S, Emmett PH, Teller E. Adsorption of Gases in Multimolecular Layers. *Journal of the American Chemical Society*. 1938;60:309-19.
- [4] Langmuir I. THE ADSORPTION OF GASES ON PLANE SURFACES OF GLASS, MICA AND PLATINUM. *Journal of the American Chemical Society*. 1918;40:1361-403.
- [5] Gardini D, Galassi C, Lapasin R. Rheology of Hydroxyapatite Dispersions. *Journal of the American Ceramic Society*. 2005;88:271-6.
- [6] Herschel W, Bulkley R. Konsistenzmessungen von Gummi-Benzollösungen. *Kolloid-Zeitschrift*. 1926;39:291-300.
- [7] Compton BG, Lewis JA. 3D-Printing of Lightweight Cellular Composites. *Advanced Materials*. 2014;26:5930-+.
- [8] Washburn EW. Note on a Method of Determining the Distribution of Pore Sizes in a Porous Material. *Proc Natl Acad Sci U S A*. 1921;7:115-6.
- [9] Araujo PW, Brereton RG. Experimental design .2. Optimization. *Trac-Trends in Analytical Chemistry*. 1996;15:63-70.
- [10] Montgomery DC. *Design and Analysis of Experiments*: John Wiley & Sons; 2008.



# Chapter 3

## MACROPOROUS APATITE-BASED SCAFFOLDS

---

The development of porous ceramics is a pivotal target for many relevant industrial applications. Particularly in the field of bone surgery, the preparation of macroporous bone substitutes for load-bearing bone parts represents one of the most challenging application, especially due to the difficulty of expressing high bioactivity and bone-like mechanical properties simultaneously.

Despite a variety of techniques has been investigated so far, the repeatable and reliable production of macroporous HA scaffolds with bone-mimicking morphology and mechanical strength is still a major challenge.

In this respect, this chapter firstly focuses on the mechanical evaluation of the performance of scaffolds obtained by replica method and then on a novel forming process based on direct foaming of ceramic suspensions. The latter, here presented for the first time, involves the preparation of micro- and macroporous hydroxyapatite-based scaffolds by high-energy planetary ball milling (Dapporto et al., *A novel route for the synthesis of macroporous bioceramics for bone regeneration*, Journal of the European Ceramic Society 36 (2016) pp. 2383-2388).

### 3.1 Preparation of macroporous bioceramic scaffolds

#### 3.1.1 Replica Method

A commercial HA powder (Riedel de Haen, Germany) was used to prepare adequate slurries for impregnation of cellulose sponges (par.1.3.1.3), according to

[1]. Several steps of sponge manipulation (wringing out, rolling up and twisting) were performed to achieve the adequate infiltration of the slurry (Fig.3.1 a-c). Then, the sponges were dried under mild vacuum conditions at 37°C and sintered in order to eliminate the organic matrix of the sponge, while consolidating the final apatite-based structures according to the initial sponge morphology (Fig.3.1 d-f).

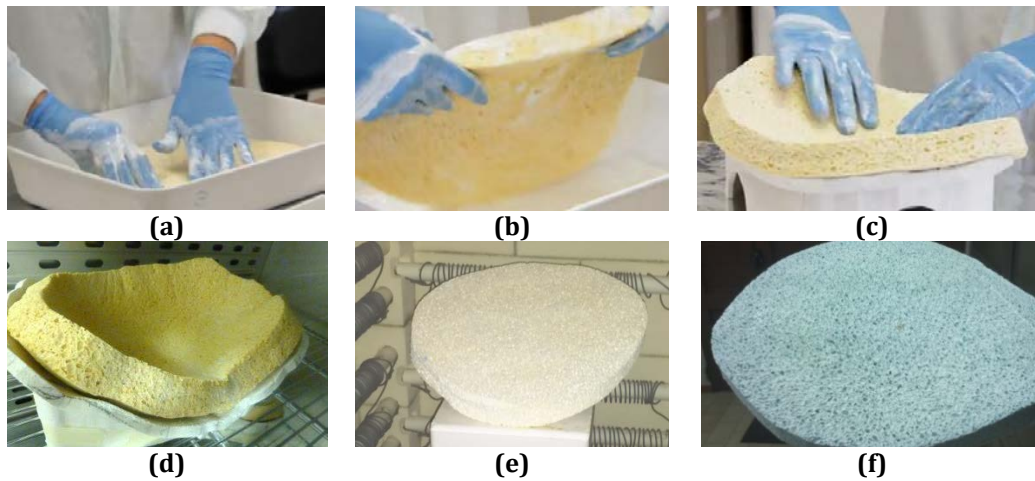


**Fig.3.1 - The multi-step Replica method**

The sintering thermal treatment included an initial debonding step, to slowly remove the organic components, without affecting the structural integrity of the scaffold (Table 3.I).

**Table 3.I - Sintering process**

<b>Temperature (°C)</b>	<b>Temperature rate (°C/h)</b>
25 - 500 (debonding)	50
500	1 h (dwell time)
500 - 1250	100
1250	1 h (dwell time)



### 3.1.2 Direct Foaming Method

Commercial HA powder (Riedel de Haen, Germany) was calcinated at 1000°C for 5 hours and sieved under 150 µm. Then, the powder was dispersed in water with Dolapix CA (Zschimmer and Schwartz, Germany), according to the weight ratio HA:H<sub>2</sub>O:dispersant=73:23:4.

A high-energy ball milling treatment, 30 minutes of stirring at 400 rpm (Pulverisette 6, Fritsch, Germany), was used for the preparation of the suspension in a 250ml zirconia jar with 6 zirconia balls (15mm diameter).

Afterwards, in respect to the powder amount, a 2 wt% of Olimpicon A (Olimpia Tensioattivi, Italy) and 0.7 wt% of W53 (Zschimmer and Schwartz, Germany) were added in the suspension as foaming agents. Then, after 5 minutes of rapid stirring at 400 rpm the as-obtained foamed suspension was poured in paper moulds and dried for 2 days at room temperature to obtain stable ceramic foams.

Three groups of HA scaffolds with different porosity (hereinafter coded as S1, S2 and S3) were prepared by varying the air volume into the jar before the last stirring.

Finally, the high-temperature thermal treatment reported in Table 3.II, including an initial debonding step, was used to consolidate the scaffolds.

**Table 3.II - Sintering process**

<b>Temperature (°C)</b>	<b>Temperature rate (°C/h)</b>
25 - 600	30
600 - 1250	100
1250	1 h (dwell time)

## 3.2 Results and Discussion

### 3.2.1 Replica method: role of sponge and thermal treatment

The characterization of sponges with 4 different increasing dry weight, henceforce coded 1, 2, 3 and 4, was carried out. The density of the sponges was evaluated by dividing the sponge dry weight and the volume of the sponge at 30 minutes after immersion in water: a slight increase of density was calculated with increasing the initial dry weight (Fig.3.2).

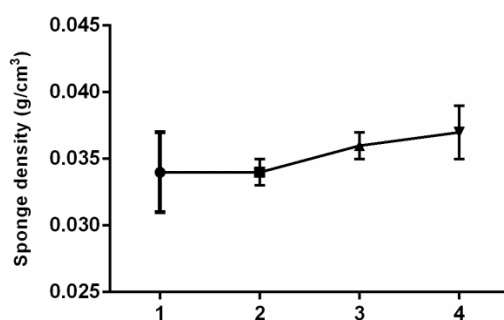


Fig.3.2 – Sponge density measurements

The morphological analysis of the sponges evidenced the presence of a wide pore size distribution, ranging from millimeters to few microns (Fig.3.3).

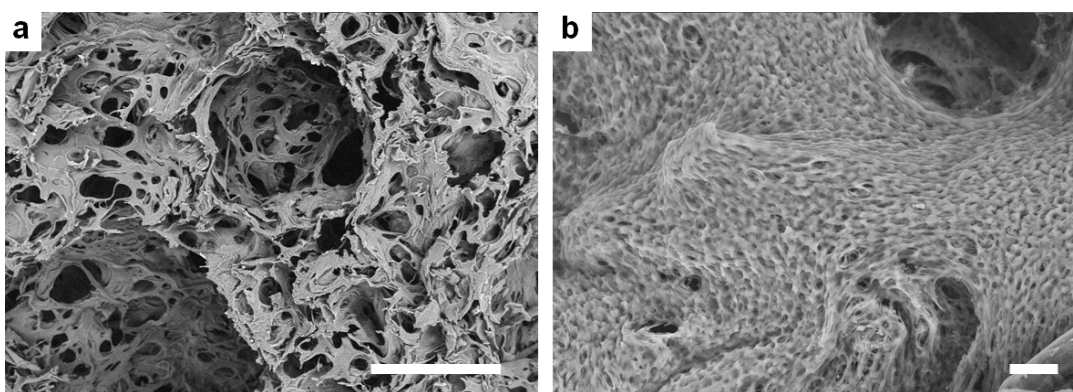


Fig.3.3 – Morphological evaluation of the commercial sponge structure.  
Scale bar: 1mm (a), 20  $\mu$ m (b)

The sponges were impregnated and sintered according to Table 3.I.

The effect of different debonding rates (20°C/h, 50°C/h and 100°C/h) on the thermal degradation of the impregnated sponges was investigated by thermogravimetry analysis, in the range 25-900°C, under nitrogen flow (Fig.3.4).

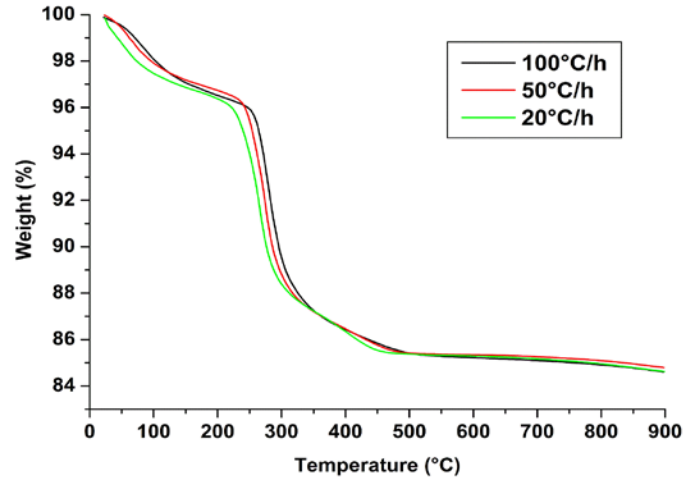


Fig.3.4 -Thermogravimetric analysis of the sponges, with temperature increasing rates (25-900°C)

The maximum mass loss rate decreased and moved toward high temperatures with increased heating rate, especially around 300°C, according to previous results [2, 3].

It is worthy noting that the mass of char residue increases at low heating rate (Table 3.III). This confirms the previous report that the char residue produced from the pyrolysis of cellulose increases with longer preheating at the low-temperature from 250 to 300°C [4].

Tab.3.III - Weight loss of the samples for each heating rate process

Heating rate	Weight loss (%) T>500°C	Weight loss (%) T=900°C
20°C/h	-0.76	-14.22
50°C/h	-0.63	-15.19
100°C/h	-0.81	-15.68

The effects of different debonding heating rate and sponge density on the 4-point bending strength of the porous scaffolds were investigated (Fig.3.5).

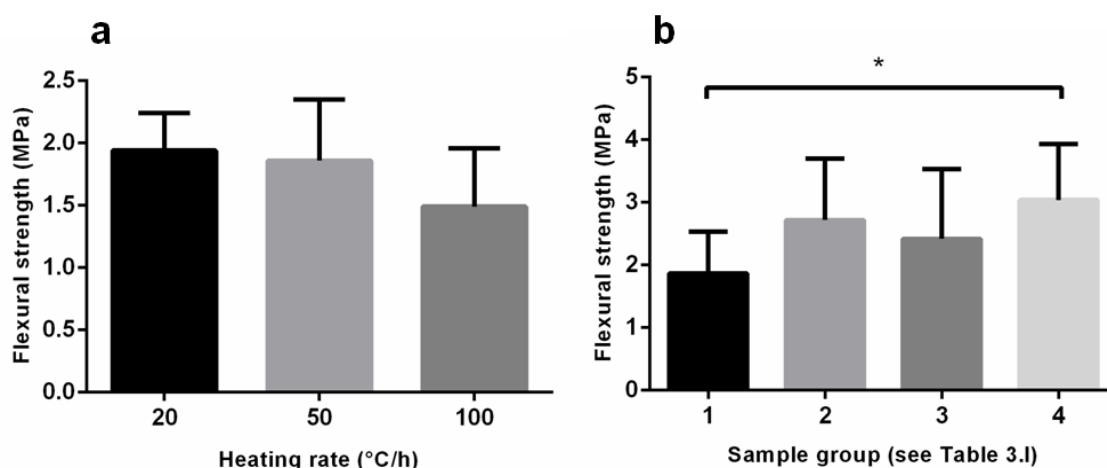


**Fig.3.5 - Effect of different debonding heating rate (a) and sponge density (b) on the flexural strength of the scaffolds**

The flexural strength exhibited a slight decrease with increasing the heating rate and increase with increasing the sponge density. A significant difference was only detected between the lowest and highest sponge density groups.

The failure of ceramic materials during testing is greatly affected by the presence of defects; in this respect, the diffuse macroporosity of the specimens, eventually associated with the unpredictable propagation of other microcracks, negatively affected the scaffold's strength and induced the high data deviation.

### 3.2.2 A novel Direct Foaming route

The specific surface area (SSA) and the mean particle diameter ( $d_{50}$ ) of the powders were analysed before and after the calcination treatment (see Table 3.IV).

**Table 3.IV - SSA and  $d_{50}$  measurements of apatite before and after the calcination treatment**

Sample	SSA ( $\text{m}^2/\text{g}$ )	$d_{50}$ ( $\mu\text{m}$ )
HA	62.6	0.5
Calcinated HA	3.7	1.7

The XRD patterns revealed that each sample is made of pure apatite phase (JCPDS Card No.09-0432). As expected, the thermally-treated powders exhibited more crystalline patterns, attested by the higher intensity of the XRD peaks as well as the

peak narrowing that puts in evidence peak splitting at higher diffraction angles due to both  $\text{CuK}\alpha 1$  and  $\text{CuK}\alpha 2$  radiations, according to Bragg's law (Fig.3.6).

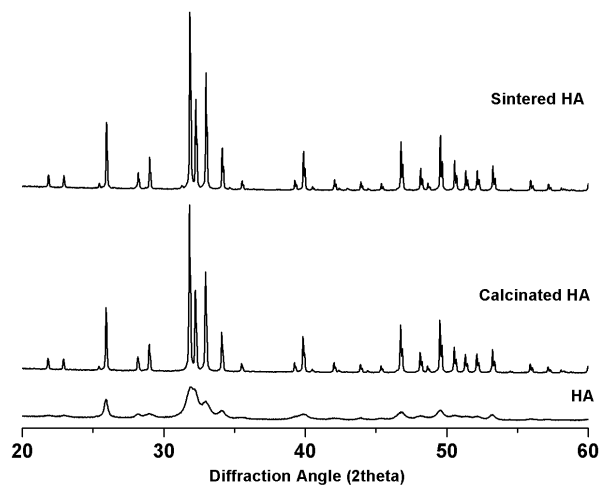


**Fig.3.6 - XRD patterns of the powders before and after thermal treatments**

The rheological behaviour of a ceramic suspension is strongly related to the interaction forces among the particles dispersed in water, in particular to the balance between the Van der Waals attraction forces and the electrostatic repulsive forces [5]. Typically, when ceramic powders are dispersed in water, the presence of attraction forces results in powder aggregation, so that the repulsive component should be artificially increased to obtain agglomerate-free systems [6-8].

In fact, inadequate dispersion of a powder can favour the formation of agglomerates, possibly resulting in microstructural inhomogeneity in the final ceramic body and in subsequent micro-cracking after sintering, due to different thermal expansion of volumes with aggregated particles in respect to porous regions.

To prevent the formation of agglomerates into the HA suspension, in the present work several precautions were taken. Firstly, the calcination treatment of the starting HA powder yielded the reduction of the specific surface area of the powder (Tab. 3.IV) with formation of more rounded particles. This occurred by thermal activation of surface diffusion phenomena inducing only a limited coalescence of the primary HA particles thus preventing grain growth [9, 10]. Then, the dispersion of the particles in the water suspension was primarily

obtained by using ammonium polyacrylate as a dispersant agent, which is a synthetic polyelectrolyte that can control the surface charge of the suspended powder particles by electrosteric dispersion phenomena [11]. Particularly, in this work a low electrolyte concentration was introduced in the aqueous solution, so that the molecules were stretched as a consequence of electrostatic repulsions along the polymer length and adsorbed onto the powder surface in a thin, flat train configuration, without the formation of loops [12, 13]. The as-obtained steric barrier, associated to the primarily electrostatic repulsion, contributed to the dispersion of the powder particles.

After obtaining a stable ceramic suspension, the foams were prepared by adding anionic tensioactive molecules based on ammonium lauryl sulphate. Upon stirring with the planetary mill, the dissociation of lauryl sulphate anions and ammonium cations occurred, leading to the formation of spheric micelles, with hydrophilic head of the sulphate portion on the outside surface and the hydrophobic tails pointing inwards towards the centre. The polar heads reduced the surface tension of water by disrupting the hydrogen bonds, favouring the incorporation of air in the form of bubbles into the suspension.

The traditional approach of direct foaming method involves several hours (e.g. 12-18 hours, typically) of mild ball milling in order to achieve the powder deagglomeration and the homogenization of the suspension [14, 15].

In this work, the novelty is represented by the use of planetary ball milling for a quicker preparation of the suspension (the process time was reduced to less than 1 hour). In this respect, it can be supposed that the improved milling efficiency was related to the high-energy ball-ball and ball-wall impacts introduced by the planetary milling, especially if the milling jar and balls have higher specific weight than the powder dispersed in the slurry [16, 17].

The relative density of the cellular solid was determined by the ratio  $\rho_c/\rho_s$ , that is, the density of the cellular material calculated as weight-on-volume ratio ( $\rho_c$ ), divided by the theoretical density of hydroxyapatite phase ( $\rho_s=3.16 \text{ g/cm}^3$ ). The porosity of the structures,  $\Phi$ , was evaluated as  $\Phi = 1-\rho_c/\rho_s$ .

The porosity of sintered samples was evaluated by both such geometrical method and the Hg intrusion technique, showing comparable results (Table 3.V).

Tab.3.V – Results of the mercury porosimetry analysis

Sample	Porosity $\Phi$ (%)	$\Phi$ by Hg intrusion (%)	Total pore volume (mm <sup>3</sup> /g)	Total pore surface area (m <sup>2</sup> /g)	Average pore diameter ( $\mu$ m)	Median pore diameter ( $\mu$ m)	Modal pore diameter ( $\mu$ m)
S1	63.0 $\pm$ 0.8	65	1001.8	2.2	1.8	164.8	247.2
S2	76.0 $\pm$ 0.7	78	1620.4	2.9	2.1	219.2	748.3
S3	85.2 $\pm$ 0.5	83	1957.4	4.4	2.0	217.7	742.1

With increasing porosity, an increase of the total pore volume and the total pore surface area was detected, together with the pores size.

The porosity of the sintered structures showed also a quasi-linear dependence with the ratio between the volume of air in the jar before the final stirring ( $V_{air}$ ) and the total jar volume ( $V_{jar}$ ) (Fig.3.7).

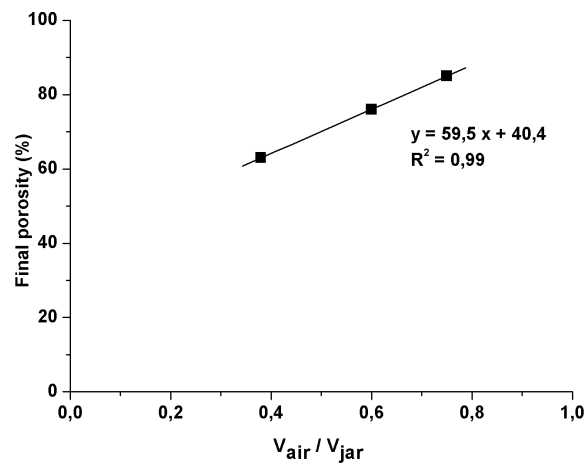


Fig. 3.7- Linear relationship between  $V_{air}/V_{jar}$  and the final porosity of the samples

The reduction in the porosity extent led to a significant increase of both compressive strength and Young’s modulus, as reported in Tab.3.VI and Fig.3.8. The number of tested specimens was also adequate to implement the Weibull analysis: high Weibull moduli were detected for each sample, proving the mechanical reliability of the process [18].

Pore characteristics are crucial in bone scaffolds as they strictly determine the extent of bone ingrowth. In this respect, the scaffolds developed in this work exhibited open and highly interconnected macro/micro-porosity (Tab.3.V and Fig. 3.9), that can favour cells migration and proliferation, as well as the perfusion of physiological fluids [19-23].

**Tab.3.VI - Results of the mechanical characterization**

Sample	Number of specimens	Compressive strength (MPa)	Young's modulus (GPa)	Weibull modulus (m)	Characteristic strength ( $\sigma_c$ )
S1	17	16.3 ± 4.3	2.9 ± 1.1	5.1	17.9
S2	26	4.3 ± 0.4	1.8 ± 0.2	12.7	4.8
S3	23	1.7 ± 0.4	0.8 ± 0.3	6.2	2.1

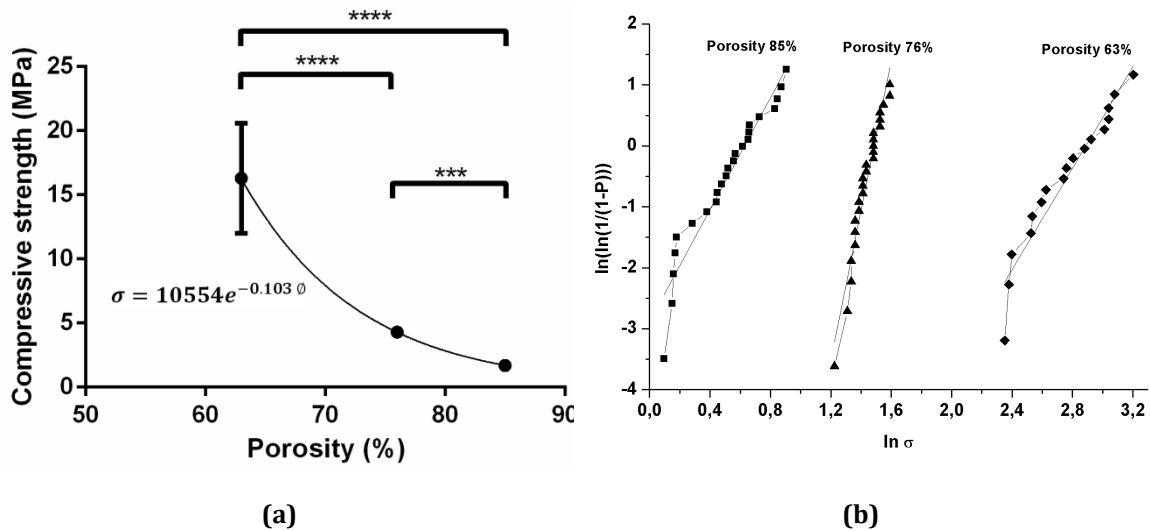


**Fig.3.8 - Mechanical characterization of the porous samples: (a) the increase of the compressive strength by reducing porosity was fitted by the reported exponential curve ( $R^2=1$ ), (b) Weibull plots for each of the 3 groups of samples analyzed in this study (\*\*\*)  $p < 0.001$ , \*\*\*\*  $p < 0.0001$ ).**

The SEM micrographs of the samples showed highly-interconnected pores with spherical shape (Fig. 3.9a). The good consolidation of the struts is clearly visible (Fig. 3.9b). Well-coalesced HA grains are intercalated to micron-size pores as detected by SEM investigation at higher magnifications (Fig.3.9c-d), also supporting the results of mercury porosimetry (Tab.3.V).



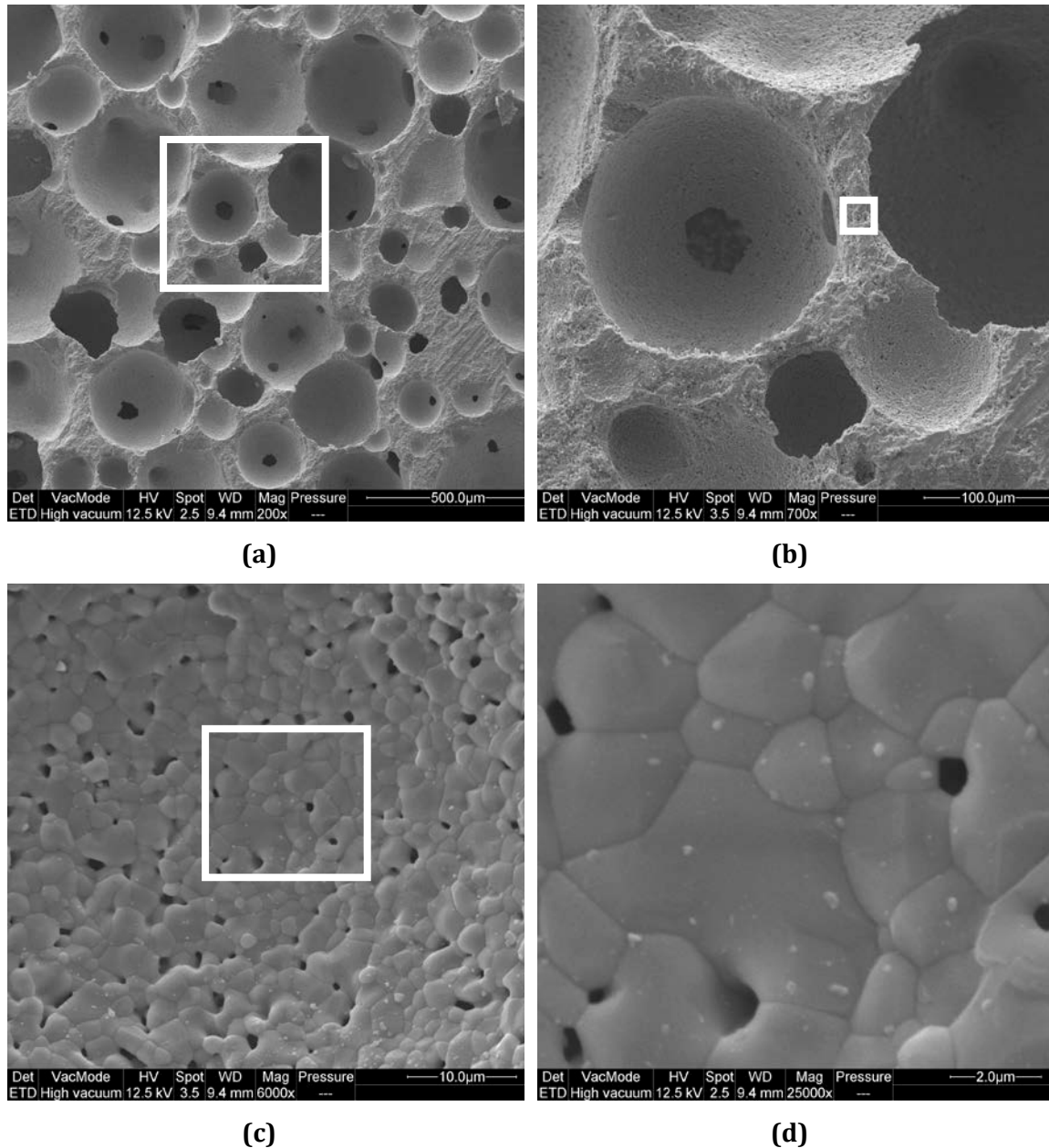


**Fig.3.9 – SEM images of the S2 porous samples. The figures (b), (c) and (d) gradually show higher magnification of figure (a), as indicated.**

A tight cohesion of apatite grains, together with a spherical pore architecture, are evident in sintered scaffolds, thus showing that the calcination treatment was effective in preserving adequate driving energy to yield extensive surface and grain-boundary diffusion towards full neck growth between particles [24] (see Fig. 3.9). This specific pore architecture may also be the source of the remarkable compressive strength of the new scaffolds (Fig. 3.8), that showed higher values than those reported in previous papers [9, 15, 18, 25-27].

The use of a high number of samples for mechanical characterization enabled to obtain the Weibull modulus, that can be used to evaluate the distribution of the strength values, thus the degree of structural homogeneity [28]. The different Weibull moduli and statistical deviations of compressive strength data could be ascribed to unpredictable flaw-pore interaction effects introduced by machining the specimens [28]. In this respect, considering the high porosity of the samples of the present study, the obtained Weibull moduli underlined the mechanical reliability and reproducibility of the process, if compared with a previously reported work [29].

The results presented in this work suggested that the application of a direct foaming method with careful adjustment of the process parameters, and the use of planetary ball milling, can result in a simple and quick approach to generate porous bioactive scaffolds with improved mechanical performance, thus preventing the need of using additional reinforcing phases for load-bearing applications. As also demonstrated in this work, this process can also be considered as a reliable tool to customize the porosity and mechanical performance of porous HA scaffolds, thus possibly opening to new personalized therapies for regeneration of load-bearing bone parts, which still represents a clinical need without adequate resolutive solutions.

To demonstrate construction of a human-sized bone structure, we fabricated a cranium fragment in a size and shape similar to what would be needed for reconstruction after traumatic injury from CT scan data: the scaffolds were provided with adequate mechanical stability to prevent failure during CNC processing (subtracting manufacturing) and complex-shape scaffolds potentially useful for maxillofacial reconstruction were successfully prepared.

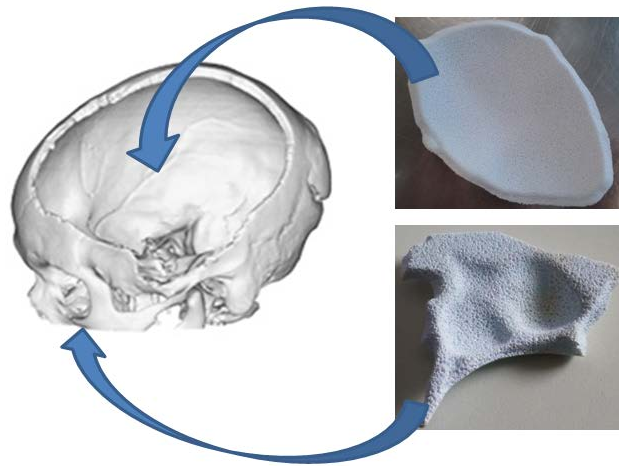


**Fig.3.10 - An example of complex-shape sample obtained after CNC prototyping, suitable for maxillofacial applications**

### **3.3 Conclusions**

The preparation of macroporous apatite-based scaffolds was carried out in this work via replica and direct foaming methods.

A slight improvement of the mechanical performance of porous structures obtained by impregnation of cellulose sponge (replica method) was obtained by increasing the sponge density.

A new method based on direct foaming was set up and optimized to develop highly porous hydroxyapatite bodies with worthy combination of pore volume and mechanical properties. The statistical evaluation of the mechanical properties enabled to validate the proposed synthesis method in respect to repeatable and reliable production of highly porous bone scaffolds. A simple model of the process parameters also pointed out the feasibility of flexible design of porous scaffolds even for load-bearing applications, thus opening to new personalized therapies.

### 3.4 References

- [1] Martinetti R, Nataloni A, Belpassi A. A method for the production of a biologically active prosthetic device for the reconstruction of bone tissue and the prosthetic device itself. Google Patents; 2005.
- [2] Bilbao R, Mastral JF, Aldea ME, Ceamanos J. Kinetic study for the thermal decomposition of cellulose and pine sawdust in an air atmosphere. *J Anal Appl Pyrol.* 1997;39:53-64.
- [3] Wang SR, Liu Q, Liao YF, Luo ZY, Cen KF. A study on the mechanism research on cellulose pyrolysis under catalysis of metallic salts. *Korean J Chem Eng.* 2007;24:336-40.
- [4] Broido A, Nelson MA. Char Yield on Pyrolysis of Cellulose. *Combust Flame.* 1975;24:263-8.
- [5] Anders AC. Rheology of Ceramic Suspensions. *Materials & Equipment/Whitewares: Ceramic Engineering and Science Proceedings*; John Wiley & Sons, Inc.; 2008. p. 1193-201.
- [6] Christian S. Stabilization of Aqueous Powder Suspensions in the Processing of Ceramic Materials. *Coagulation and Flocculation, Second Edition*; CRC Press; 2005. p. 601-62.
- [7] Kunes K, Havrda J, Hronikova K, Gregorova E, Pabst W. Stabilization of bioceramic suspensions prepared from alumina-containing zirconia powders. *Ceram-Silikaty.* 2000;44:1-8.
- [8] Sigmund WM, Sindel J, Aldinger F. Stabilization of aqueous ceramic slurries with a novel bis-hydrophilic diblock copolymer. *Z Metallkd.* 1999;90:990-5.
- [9] Cunha C, Sprio S, Panseri S, Dapporto M, Marcacci M, Tampieri A. High biocompatibility and improved osteogenic potential of novel Ca-P/titania composite scaffolds designed for regeneration of load-bearing segmental bone defects. *J Biomed Mater Res A.* 2013;101:1612-9.
- [10] Raynaud S, Champion E, Bernache-Assollant D. Calcium phosphate apatites with variable Ca/P atomic ratio II. Calcination and sintering. *Biomaterials.* 2002;23:1073-80.
- [11] Davies J, Binner JGP. The role of ammonium polyacrylate in dispersing concentrated alumina suspensions. *J Eur Ceram Soc.* 2000;20:1539-53.
- [12] Lyklema J, Fleer GJ. Electrical Contributions to the Effect of Macromolecules on Colloid Stability. *Colloid Surface.* 1987;25:357-68.
- [13] Stuart MAC, Fleer GJ, Lyklema J, Norde W, Scheutjens JMHM. Adsorption of Ions, Polyelectrolytes and Proteins. *Adv Colloid Interfac.* 1991;34:477-535.
- [14] Gonzenbach UT, Studart AR, Tervoort E, Gauckler LJ. Stabilization of foams with inorganic colloidal particles. *Langmuir.* 2006;22:10983-8.
- [15] Zhang LY, Zhou DL, Chen Y, Liang B, Zhou JB. Preparation of high open porosity ceramic foams via direct foaming molded and dried at room temperature. *J Eur Ceram Soc.* 2014;34:2443-52.
- [16] Schilz J. Internal kinematics of tumbler and planetary ball mills: A mathematical model for the parameter setting. *Mater T Jim.* 1998;39:1152-7.
- [17] Suryanarayana C. Mechanical alloying and milling. *Prog Mater Sci.* 2001;46:1-184.

- [18] Fan X, Case ED, Gheorghita I, Baumann MJ. Weibull modulus and fracture strength of highly porous hydroxyapatite. *J Mech Behav Biomed*. 2013;20:283-95.
- [19] Andrade JC, Camilli JA, Kawachi EY, Bertran CA. Behavior of dense and porous hydroxyapatite implants and tissue response in rat femoral defects. *Journal of biomedical materials research*. 2002;62:30-6.
- [20] He X, Su B, Tang ZH, Zhao B, Wang XY, Yang GZ, et al. The comparison of macroporous ceramics fabricated through the protein direct foaming and sponge replica methods. *J Porous Mat*. 2012;19:761-6.
- [21] Hyers R, SanSoucie M. Porous calcium phosphate networks for synthetic bone material. Google Patents; 2010.
- [22] Naqshbandi AR, Sopyan I, Gunawan. Development of Porous Calcium Phosphate Bioceramics for Bone Implant Applications: A Review. *Recent patents on Materials Science*. 2013;6:238-52.
- [23] Sánchez-Salcedo S, Arcos D, Vallet-Regí M, . Upgrading Calcium Phosphate Scaffolds for Tissue Engineering Applications. *Key Engineering Materials*. 2008;377:19-42.
- [24] Landi E, Tampieri A, Celotti G, Sprio S. Densification behaviour and mechanisms of synthetic hydroxyapatites. *J Eur Ceram Soc*. 2000;20:2377-87.
- [25] Soon Y-M, Shin K-H, Koh Y-H, Lee J-H, Choi W-Y, Kim H-E. Fabrication and compressive strength of porous hydroxyapatite scaffolds with a functionally graded core/shell structure. *J Eur Ceram Soc*. 2011;31:13-8.
- [26] Woottichaiwat S, Puajindanetr S, Best SM. Fabrication of Porous Hydroxyapatite through Combination of Sacrificial Template and Direct Foaming Techniques 2011.
- [27] Yook S-W, Kim H-E, Yoon B-H, Soon Y-M, Koh Y-H. Improvement of compressive strength of porous hydroxyapatite scaffolds by adding polystyrene to camphene-based slurries. *Materials Letters*. 2009;63:955-8.
- [28] Rice RW. Porosity of Ceramics: Properties and Applications: Taylor & Francis; 1998.
- [29] Fan X, Case ED, Ren F, Shu Y, Baumann MJ. Part I: Porosity dependence of the Weibull modulus for hydroxyapatite and other brittle materials. *J Mech Behav Biomed*. 2012;8:21-36.



# Chapter 4

## PREPARATION OF $\beta$ -TCP

### SCAFFOLDS BY ROBOCASTING

---

The preparation of porous scaffolds able to support the regeneration of bone tissue requires technologies enabling the control of chemistry, morphology and mechanical performance of the final scaffolds. Calcium phosphate ceramics (CaPs) have been successfully used in bone replacement for more than 50 years but, despite a lot of techniques have been proposed to obtain porous structures, the achievement of controlled porosity to enhance the cell proliferation, while preserving adequate mechanical strength still remains a significant challenge. This chapter is focused on my 6-months activity at Imperial College London, where I fabricated three dimensional (3D) calcium phosphate scaffolds via robocasting, a computer-assisted additive manufacturing approach involving the layer-by-layer deposition of material.

#### **4.1 The robocasting as additive manufacturing approach**

The ability to design and fabricate complex-shape scaffolds is a major issue in bone tissue engineering.

Diverse techniques, such as the use of replica templates (starting from polymeric sponges [1] or coral structures [2]), emulsions [3], the use of porogens [4] and freeze casting [5], have been used to build porous ceramic scaffolds for tissue engineering.

However, most of them offer only a very limited control of the porosity and are not suited to the fabrication of materials with complex shapes. New solid-free-form fabrication techniques developed during the past 20 years allow the fabrication of

ceramic materials with very complex architectures by following a computer design [6].

In the 1980s, with the advent of additive manufacturing technologies, many applications, including the processing of bioceramic materials, benefited from the faster processing of products without the need for specific tooling or molds [7]. The 3D printing technology, in particular, was developed in the early 1990s at MIT (Cambridge, MA) [8].

By using such technologies, the structural architecture can be optimized to promote bone regeneration and enhance the mechanical response of the scaffolds [9]. Among these, robocasting, a technique that combines an extrusion process with a computer-guided positioning system, can be used to build 3D structures layer by layer, by extruding a continuous filament. Robocasting inks have to flow under stress and recover enough stiffness such that, when the stress is released, they can bear both the filament weight and the weight of successive layers. Robocasting permits printing with outstanding spatial resolution and has been used to print ceramic grids with line and gap diameters varying from hundreds of microns to submicron levels. In this respect, the robocasting technique allows the tailoring of the overall porosity of the scaffolds, together with the pore size, shape and distribution (Fig.4.1).

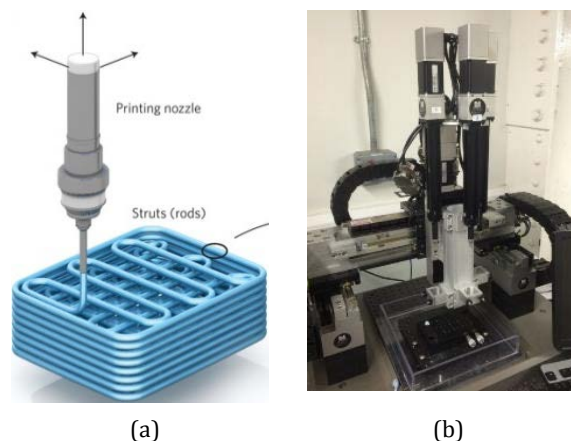


**Fig.4.1 - A schematic representation of 3D printing by robocasting [10]**

In this context, a great deal of research effort was devoted to the preparation of inks provided with adequate flowability and viscoelasticity, including the addition



of coagulant agents [11]. These inks have a very low organic content and can be printed inside a non-wetting oil bath, avoiding the appearance of tensions derived from uneven drying [12]. However, the achievement of adequate rheological performance of the inks requires the tuning of several parameters, including the powder content and particle size, the organic binder amount and the pH. In particular, the latter can be a problem when the printing of calcium phosphates is demanded, especially because on their pH-dependent solubility. The binder, which can be organic or water-based, locally binds the particles and hardens the wetted area, or results in a reaction similar to the hydraulic setting reaction in cements [13].

The main objective of this work was to design a flexible ink formulation approach to print a wide range of calcium phosphates. This would enable the fabrication of rigid scaffolds with composition and microstructure optimized for specific applications.

In this activity, I prepared 3D complex-shape micro- and macroporous  $\beta$ -TCP scaffolds by robotic assisted deposition (3D Inks, USA).

#### **4.2 Preparation of calcium phosphate pastes for robocasting**

The preparation of  $\beta$ -tricalcium phosphate ( $\beta$ -TCP) suspensions to obtain micro- and macroporous scaffolds by robocasting involved the functionalization of the powder particles with a branched copolymer surfactant (BCS).

Commercial  $\beta$ -TCP powders (Keramat, Spain) were dispersed in water-based suspensions containing different amounts of BCS, according to the volume ratio powder:water suspensions=43:57 and mild ball milled for 24 hours after addition of alumina-based milling spheres.

The BCS is based on methyl methacrylic acid (MAA) and polyethylene glycol methacrylate (PEGMA) with hydrophobic dodecanethiol (DDT) chain ends and ethylene glycol di-methacrylate (EGDMA) as cross linker [14-16] (Fig.4.2a).

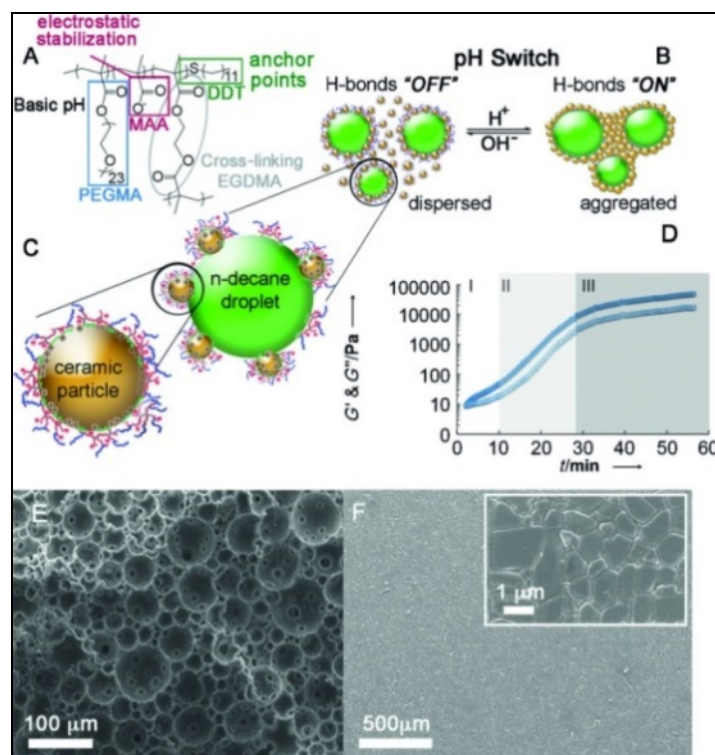


**Fig.4.2 - a) BCS structure showing the branch functionalities. b) pH-triggered assembly of an oil-in-water emulsified suspension of BCS functionalized ceramic particles. c) The BCS-particle-droplet and BCS-particle interactions. d) Evolution of the viscoelastic ( $G', G''$ ) properties of an emulsified suspension with changing pH, illustrating the assembly process. Examples of ceramic structures fabricated through responsive self-assembly: E) porous SiC from an emulsion and F) sintered highly dense (>99% of the theoretical value) alumina [17].**

This amphiphilic molecule can segregate to oil-water interfaces, stabilizing them [16]. Furthermore, the branched architecture ensures that each molecule contains multiple potential points of attachment to the surface of an inorganic particle to functionalize it and promote its segregation to oil-water interfaces in an emulsion (Fig.4.2 b,c).

Attachment and functionalization occurs by the following mechanisms: 1) The interactions of the hydrophobic chain ends (DDT) on the surfaces; 2) the electrostatic interaction between the carboxylic anions in the MAA residues ( $\text{COO}^-$ ) with the positively charged particle surfaces; and 3) the establishment of chemical covalent bonding between the carboxylic residues and the metal oxides on the surface of the particles.

The functionalization of the ceramic particles with BCS leads to the creation of smart inorganic particles that can self-disperse or assemble to form a network

under pH control (Fig.4.2b,c,d). The branched architecture of BCS ensures that each molecule contains multiple potential points of attachment to the surface of the inorganic particles, promoting also the segregation to oil–water interfaces.

The addition of a pH-switch triggers a sort of particles coagulation, which promotes the tight packing of the ceramic particles (Fig.4.2b). When allowed to dry, the oil phase is eliminated from our material, and we obtain this porosity as a consequence of the oil templating.

A similar process allows the fabrication of strong materials with complex shapes and a wide range of architectures from dense to foams with closed or open cells [17] (Fig.4.2 e,f).

The suspensions were also emulsified with Decane (Sigma Aldrich) at 50 vol% and stirred at 24k rpm (T25 Ultra-Turrax, IKA, Germany) in order to induce the formation of microbubbles into the suspension, while Glucono- $\delta$ -Lactone (GdL) (Sigma Aldrich) was finally added as pH-trigger.

The pH and rheological performance of suspensions and emulsions were analyzed after the preparation and 72 hours after the addition of GdL.

The influence of different BCS (wt%), pH-trigger (wt%) and stirring times on the pH, viscosity and Yield stress of the inks was evaluated according to a Design of Experiment (DoE) approach (Face Centered Central Composite scheme (FCCCD)) (Table 4.I).

**Table 4.I - Input parameters (coded levels) and output parameters of the FCCCD scheme**

INPUT PARAMETERS		-1	0	+1	OUTPUT PARAMETERS
<b>A</b>	BCS concentration (wt%)	2	4	8	pH Viscosity Yield stress (Pa)
<b>B</b>	GdL concentration (wt%/vol%)	1	2	4	
<b>C</b>	Emulsification time (min)	0	2,5	5	

Regression analysis of data, contour plots and Pareto charts were obtained with MATLAB software.

The phase composition of suspensions and emulsions was also performed before and after sintering (Table 4.II) and the microstructure of the scaffolds was finally analyzed by scanning electron microscopy.

Table 4.II - Sintering treatment

Temperature (°C)	Rate increase (°C/min)	Dwell time (hours)
0-500	1	-
500	-	2
500-989	5	-
989	-	1

### 4.3 Results and Discussion

The suspensions exhibited basic pH (8.6-9.2) and appeared well-dispersed, probably due to the steric and electrostatic stabilization provided by the functionalities in the branches (EG and MAA).

Only a slight decrease of the pH was observed even quadrupling the BCS amount, probably due to the polymer buffer properties [17] (Fig.4.3). On the other hand, the increase in BCS reflected in the increase of the suspensions' viscosity.

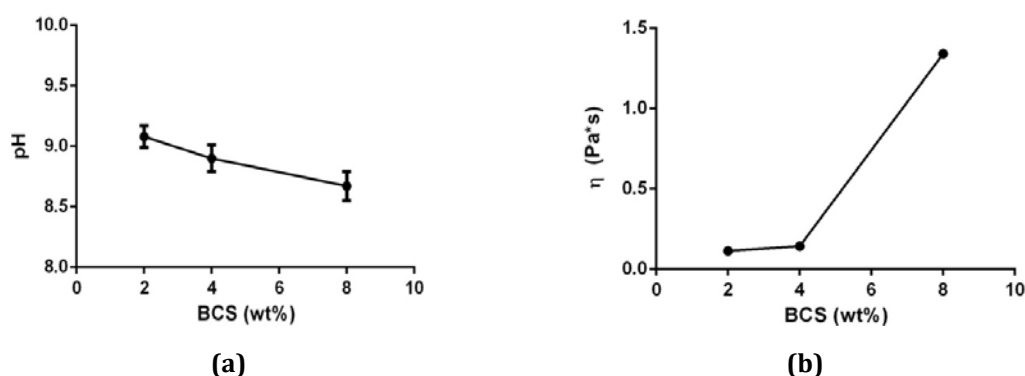


Fig.4.3 - pH and viscosity of the suspensions, with increasing the amount of BCS

No statistical difference was observed among the zeta-potential of the suspensions at different pH (titration test), probably due to the buffer property of the polymer.

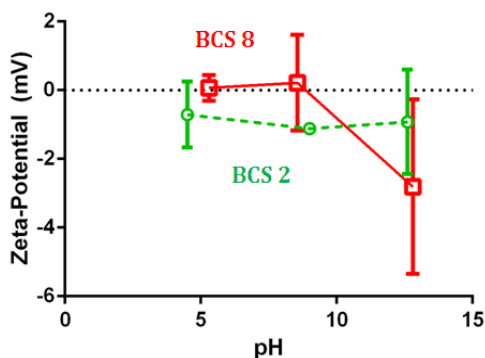


Fig.4.4 - Zeta potential of the suspensions with increasing the amount of BCS

The analysis of the viscoelasticity evidenced an increase of both Storage and Loss moduli, while no Yield stress was detected (Fig.4.5).

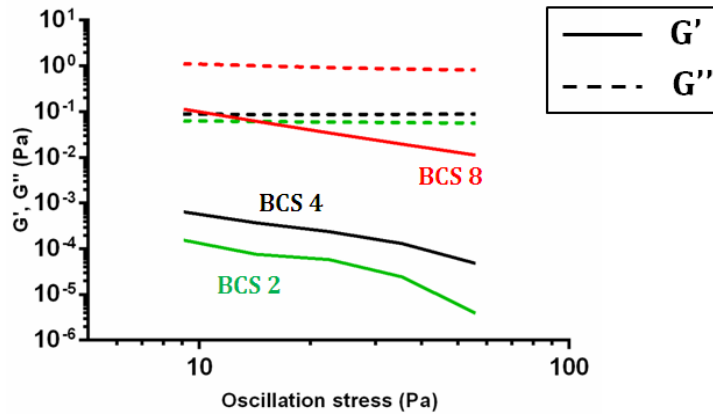


Fig.4.5 - Viscoelastic properties of the suspensions

The loss moduli, higher than the storage moduli, confirmed the prevalent fluid behavior of the suspensions. After the addition of GdL, a significant decrease of the pH was observed (Fig.4.6).

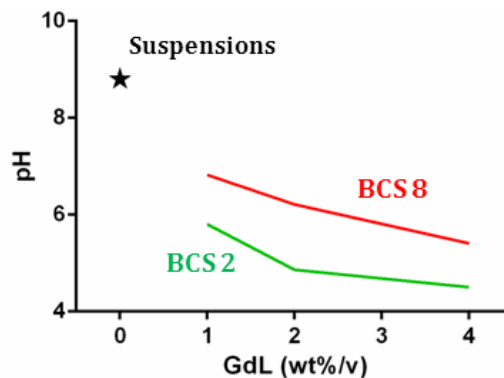


Fig.4.6 - pH of the suspensions with increasing of GdL

The lowest pH were detected for the suspensions with lower amount of BCS; this is in agreement with a previous work, in which it was stated that, because of the buffer polymer, larger BCS concentrations lead to longer aggregation times, so slower pH drop [17].

The addition of GdL determined also an increase of the viscosity (Fig.4.7): the highest viscosity was exhibited by the lowest BSC suspensions. This is actually in

agreement with the pH results (Fig.4.6), as lower pH determines higher aggregation of the powder particles and higher viscosity.

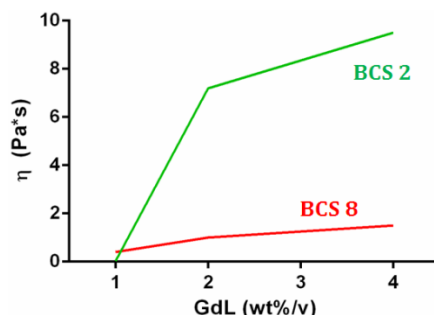


Fig.4.7 – Viscosity of the suspensions with increasing the GdL

The rheological tests showed an increase of both Storage and Loss moduli while increasing the GdL amount: in particular, the higher viscosity of BCS2 reflected also in the highest  $G'$ . No yield stress was detected.

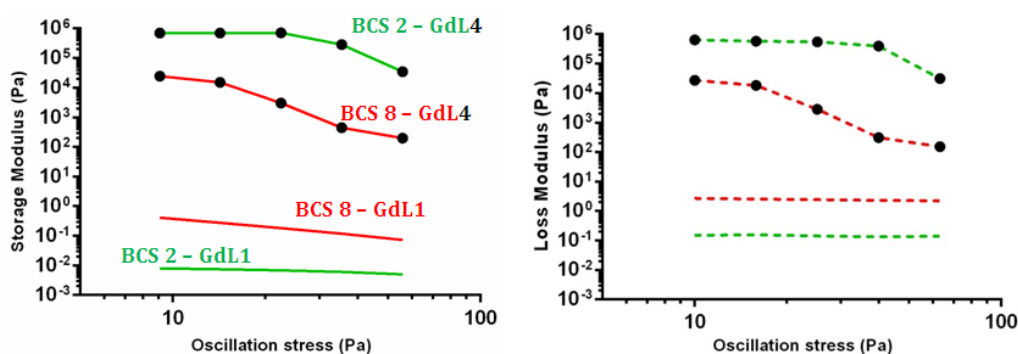


Fig.4.8 – Viscoelastic properties of the suspensions, after addition of GdL

The viscoelasticity tests were in accordance with the viscosity measurements: if only 1wt%/vol of GdL is added, the suspensions with higher amount of BCS exhibit higher viscosity and dynamic mechanical performance, but increasing the amount of GdL the result is reversed (Fig.4.7-4.8).

However, it should be noted that a slight sedimentation of the powder occurred, leading to partial solid/liquid demixing: it was hypothesized that within 72 hours the GdL is able to induce extensive ceramic particles aggregation, by turning away the water molecules around the particles. For that reason, the rheological tests were partially negatively affected.

After the emulsification of the suspensions with decane, the oil droplets were stabilized by a synergetic combination of the BCS molecules in the liquid and the functionalized particles, both of which attach to the oil–water interface.

The emulsification induced an increase of the viscosity, if compared with the suspensions (Fig.4.9); in addition, the effect of both stirring time and BCS concentration on the rheological performance was separately evaluated, indicating a slight prevalence of BCS in increasing the viscosity.

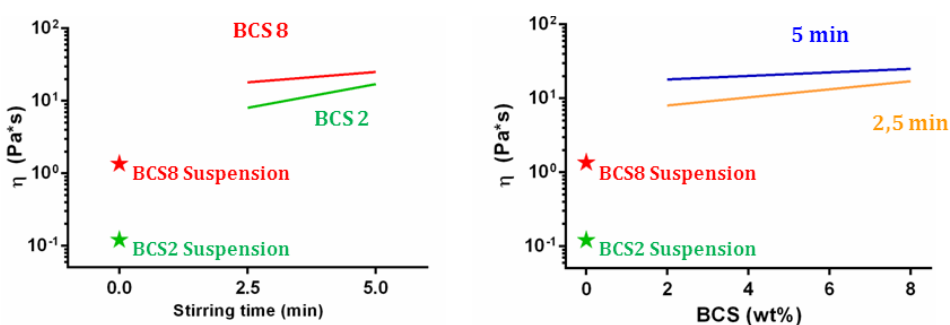


Fig.4.9 – Viscosity tests of the emulsions, by varying stirring time and BCS amount

The viscoelasticity analysis of the emulsions showed also a slight increase of the storage and loss modulus with increasing the amount of BSC (Fig.4.10), while a higher increase of the yield stress (here approximated by the intersection between the two curves) also occurred.

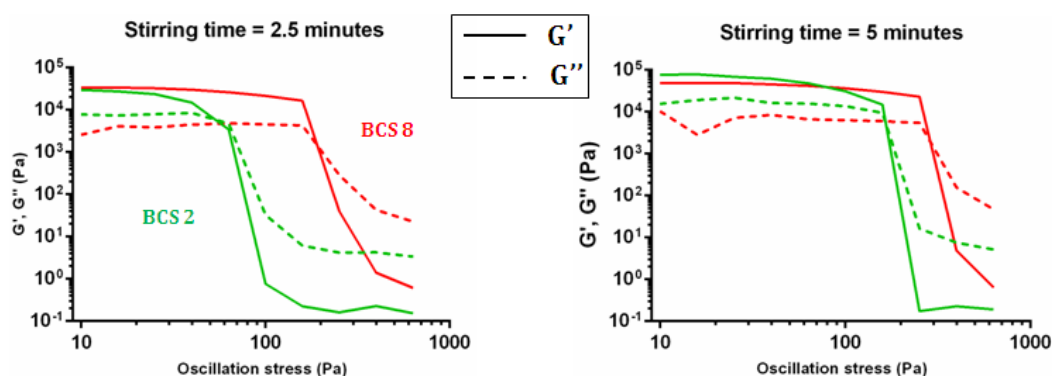


Fig.4.10 – Storage and Loss modulus of the emulsions, after 2.5 and 5 minutes of emulsification

At high pH, both suspensions and emulsions were mainly fluid. After the addition of GdL, a homogeneous decrease of pH occurred (due to the hydrolysis of GdL to

gluconic acid [15, 18, 19]), while increasing the viscosity (due to the formation of multiple links between the BCS-functionalized particles).

The effect of different BCS (wt%), GdL (wt%) and stirring times on the pH, viscosity and Yield stress of the  $\beta$ -TCP emulsions was assessed according to the Design of Experiment scheme reported in Table 4.III.

**Table 4.III – The full factorial FCCD scheme implemented in this study**

<b>A</b>	<b>B</b>	<b>C</b>	<b>AB</b>	<b>AC</b>	<b>BC</b>	<b>A<sup>2</sup></b>	<b>B<sup>2</sup></b>	<b>C<sup>2</sup></b>	<b>pH</b> (after 72h GdL)	<b>Viscosity</b> (constant shear rate 50s <sup>-1</sup> after 96h GdL) [Pa * s]	<b>Yield stress</b> (after 96h GdL) [Pa]
-1	-1	-1	1	1	1	1	1	1	5,00	4,00	4
1	-1	-1	-1	-1	1	1	1	1	6,34	5,00	5
-1	1	-1	-1	1	-1	1	1	1	4,34	12,00	56
1	1	-1	1	-1	-1	1	1	1	4,78	48,00	300
-1	-1	1	1	-1	-1	1	1	1	5,02	20,00	110
1	-1	1	-1	1	-1	1	1	1	6,14	26,00	125
-1	1	1	-1	-1	1	1	1	1	4,51	60,00	300
1	1	1	1	1	1	1	1	1	4,73	95,00	380
0	0	0	0	0	0	0	0	0	5,02	22,00	50
0	0	0	0	0	0	0	0	0	5,24	23,00	51
0	0	0	0	0	0	0	0	0	5,02	22,00	52
-1	0	0	0	0	0	1	0	0	4,55	21,00	20
1	0	0	0	0	0	1	0	0	5,01	20,00	75
0	-1	0	0	0	0	0	1	0	5,78	15,00	24
0	1	0	0	0	0	0	1	0	4,66	43,00	120
0	0	-1	0	0	0	0	0	1	4,90	5,00	35
0	0	1	0	0	0	0	0	1	4,72	32,00	250

The regression analysis of data is reported in Table 4.IV.

**Table 4.IV – Summary of the regression analysis of data**

	<b>pH</b>		<b>Viscosity</b>		<b>Yield stress</b>	
	<b>Coefficient</b>	<b>p-value</b>	<b>Coefficient</b>	<b>p-value</b>	<b>Coefficient</b>	<b>p-value</b>
<b>Constant</b>	4.98	0.00	19.98	0.00	51.00	0.02
<b>A</b>	0.36	0.00	7.70	0.00	39.50	0.01
<b>B</b>	-0.52	0.00	18.81	0.00	88.80	0.00
<b>C</b>	-0.02	0.64	15.90	0.00	76.50	0.00
<b>AB</b>	-0.23	0.00	8.00	0.00	38.50	0.00
<b>AC</b>	-0.05	0.36	0.50	0.83	-18.75	0.22
<b>BC</b>	0.04	0.52	7.25	0.01	12.25	0.41
<b>A<sup>2</sup></b>	-0.12	0.23	2.28	0.56	-3.50	0.89
<b>B<sup>2</sup></b>	0.32	0.01	10.77	0.02	21.00	0.41
<b>C<sup>2</sup></b>	-0.09	0.35	0.27	0.94	91.50	0.01
<b>R<sup>2</sup></b>	96 %		95%		95 %	
<b>R<sup>2</sup> (adj)</b>	92 %		91%		88 %	



To maximize the responses, the factors with positive coefficients should be increased and those with negative coefficients should be decreased.

Considering only the coefficients with  $p < 0.05$ , the regression models for pH, viscosity and yield stress were:

**Table 4.V - Regression models of the output parameters (considering  $p < 0.05$ )**

Output parameters	Regression model
pH	$4,98 + 0,36 A - 0,52 B - 0,23 AB + 0,32 B^2$
Viscosity $\eta (\dot{\gamma} = 50s^{-1})$	$19,98 + 7,70A + 18,81B + 15,90C + 8AB + 7,25BC + 10,8 B^2$
Yield stress ( $\tau_{yield}$ )	$51 + 39,5A + 88,8B + 76,5C + 38,5AB + 91,5 C^2$

On the basis of the regression analysis results, a Pareto chart was also implemented to show the most effective input parameters on the outputs (Fig.4.11).

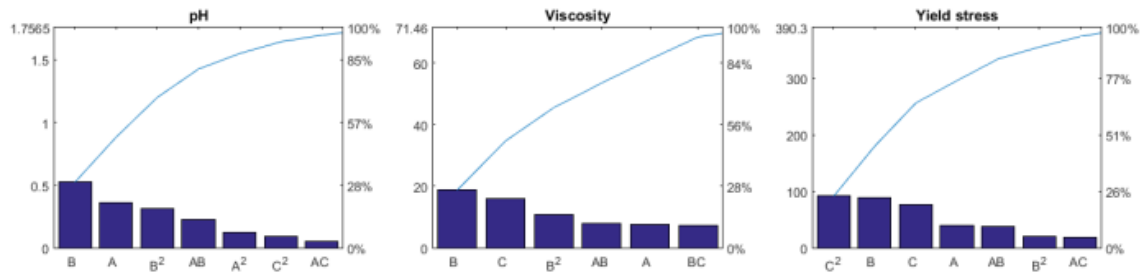


**Fig.4.11 - Pareto charts of the data**

It was observed that the parameter which mainly affects pH, viscosity and yield stress of the emulsions is the GdL concentration. Moreover, both the viscosity and yield stress are secondly affected by the emulsification time, more than the BCS concentration. As shown, the interactions among the input parameters were also significant.

Contour plots were generated from the model equations obtained in the regression analysis (Fig.4.12), in which the blue and red colors refer to lower and higher values of the response, respectively.

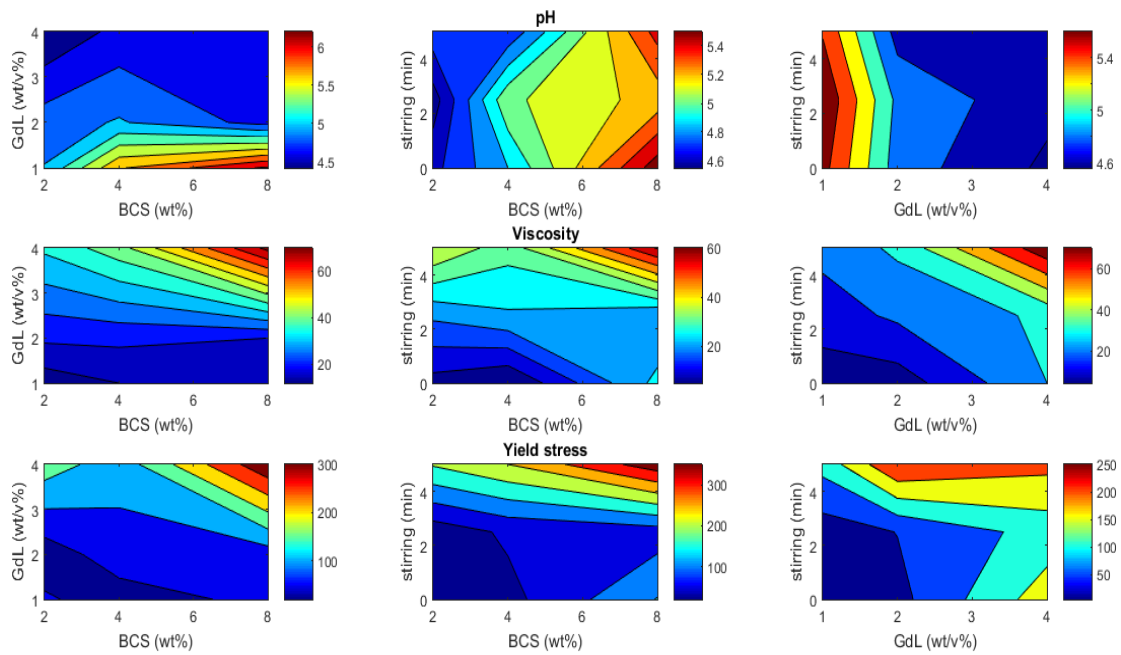


**Fig.4.12 - Contour plots of data**

The two dimensional contour plots are a series of curves of constant response for different combinations of factor levels. Such diagrams illustrate the change in properties when two or more variables change together and allow predictions to be made for combinations not actually run in the experiment. The significant interactions between the parameters are easily observable where the contour lines diverge from horizontal or vertical trends.

The phase composition analysis of some formulations of suspensions and emulsions before and after sintering is reported in Fig.4.13.

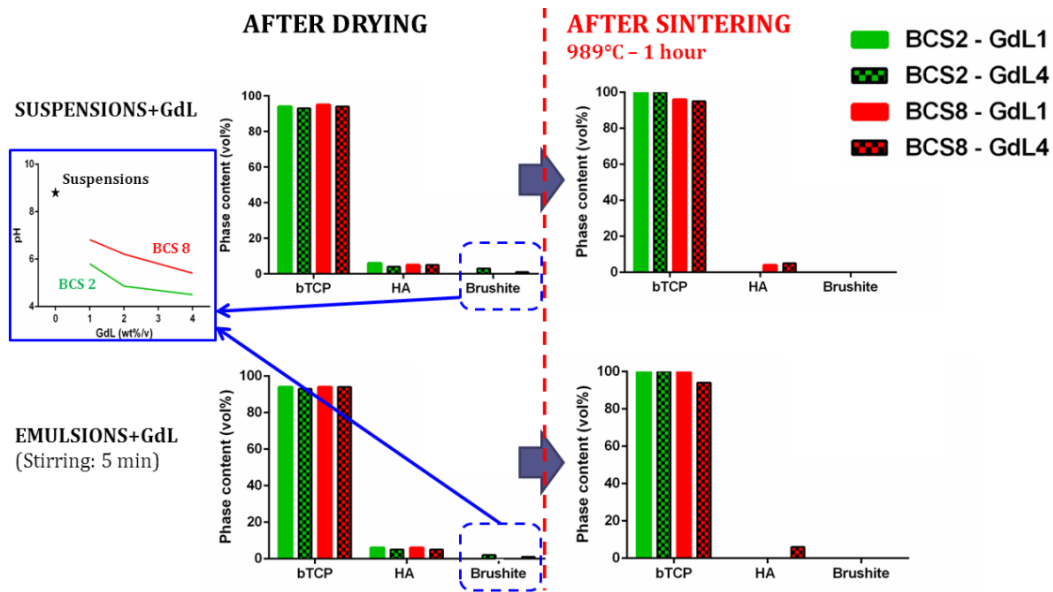


**Fig.4.13 – Effect of BCS and GdL on the phase composition**

Generally, the calcium phosphates solubility is strongly dependent on the pH: the solubility increases with lowering the pH. In this respect, with increasing the GdL amount, the dissolution of the  $\beta$ TCP followed the pH lowering, leading to the formation of hydroxyapatite (HA) and brushite ( $\text{CaHPO}_4 \cdot 2\text{H}_2\text{O}$ ).

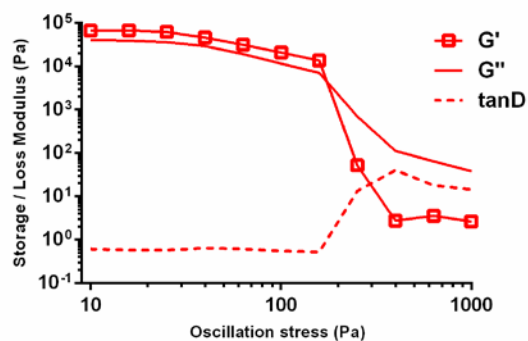
The formation of brushite was higher when lower amount of BCS was present; this is in agreement with the pH results (Fig.4.6), as larger amount of BCS induce slower pH drop.

Due to the difficulty in printing ink formulation with lower amount of BCS, it was supposed that the polymer content greatly enhances the ink stability, but may also results in larger microporosity and lower mechanical strength.

After the thermal treatment, the brushite was fully reconverted into  $\beta$ TCP and HA.

Due to the difficulty in printing ink formulation with lower amount of BCS, it was supposed that the polymer content greatly enhances the ink stability, but may also results in larger microporosity and lower mechanical strength.

The most reliable, fully injectable ink formulation for robocasting was identified as the one containing BCS (8wt%), GdL (2wt%) and emulsified for 5 minutes (Fig.4.14).



<b>pH</b>	5.3 ± 0.2
<b>Viscosity (Pa*s)</b>	28
<b>Yield Stress (Pa)</b>	160

**Fig.4.14 - Rheological performance of the most reliable ink formulation for robocasting**

This emulsion was deposited in a layer-by-layer sequence to directly write complex 3D patterns able to mimic the spongy bone architecture surrounded by an external cortical bone layer (Fig.4.15).

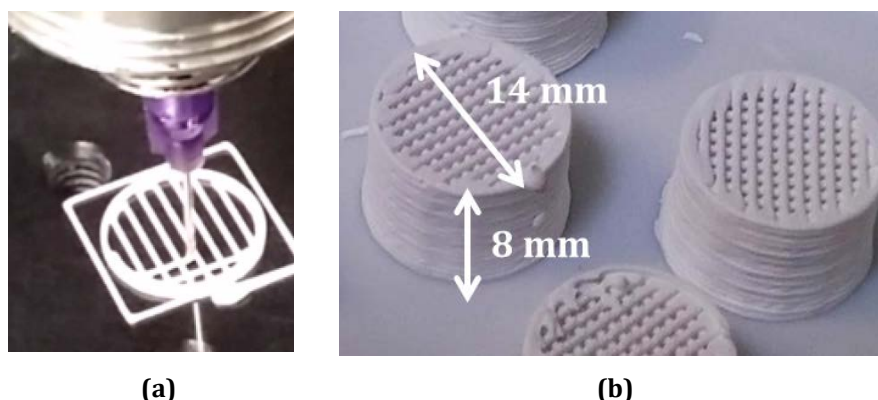


**Fig.4.15 - Preparation of the scaffolds via robocasting (a) and macroscopic view of the robocasted scaffolds, after sintering (b)**

The inks were deposited through cylindrical nozzles of diameter  $d=510\mu\text{m}$  at a constant linear printing speed of 20 mm/s. A layer spacing  $\Delta z=0.80d$  was implemented to promote intimate contact between the layers. The emulsion was successfully extruded without demixing or decohesion. No collapse of the struts occurred after drying for 3 hours at room temperature followed by drying for 24 hours at 37°C.

After the sintering treatment (Tab.4.II), the structure exhibited interpenetrated struts associated with an extensive microporosity (Fig.4.16).

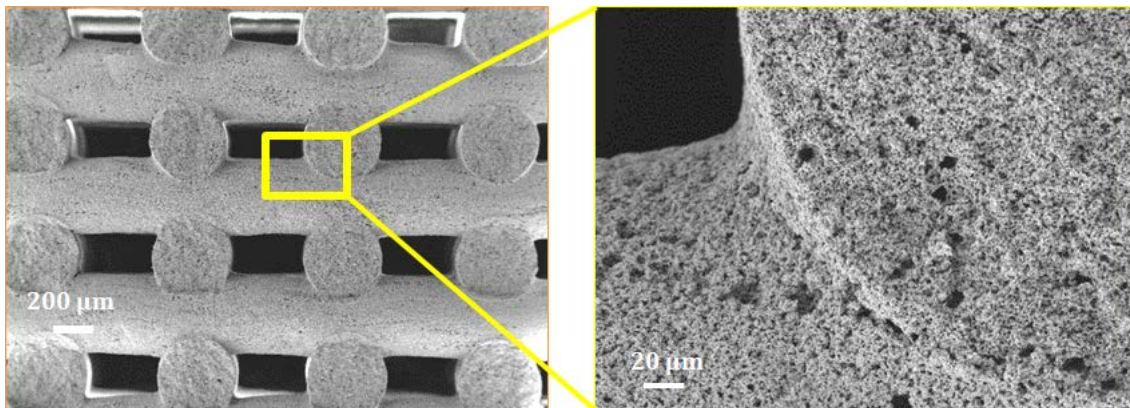


**Fig.4.16 - Microstructure of the sintered robocasted structures**

The extensive microporosity resulted from the oil templating can favour cell attachment and proliferation, as well as the perfusion by physiological fluids [20-22].

The mechanical performance of ceramic materials are strictly related to the density of the green body (semifinished sample before thermal treatment), as well as the micro- and macroporosity.

The macroporosity of the robocasted specimens was determined by geometrical method: the relative density was determined by the ratio  $\rho_c/\rho_s$ , that is, the density of the cellular material calculated as weight-on-volume ratio ( $\rho_c$ ), divided by the theoretical density of  $\beta$ -TCP phase ( $\rho_s=3.08 \text{ g/cm}^3$ ). The porosity of the structures,  $\Phi$ , was evaluated as  $\Phi = 1-\rho_c/\rho_s$ .

In addition, in order to investigate the microporosity of the struts, parallelepiped molds were filled with the same ink formulation used for robocasting. After appropriate drying and sintering, the porosity of the struts was evaluated by geometrical method and the compressive strength was evaluated by uniaxial loading of parallelepiped specimens (11 x 6 x 3 mm) with a preload of 0.5N (Table 4.VI).

**Table 4.VI – Porosity and mechanical performance of struts and robocasted samples**

	<b>Total Porosity (%)</b>	<b>Compressive strength (MPa)</b>	<b>Young's Modulus (GPa)</b>
<b>Strut</b>	66.7 ± 0.5	4.50 ± 0.96	0.15 ± 0.02
<b>Robocasted</b>	80.2 ± 0.8	1.77 ± 0.41	0.11 ± 0.02

The strength of the robocasted scaffolds is comparable with the typical values attributed to trabecular bone [23].

Despite the optimal reproducibility and structural homogeneity of such robocasted scaffolds, the reported mechanical performance are not actually able to meet the requirements for load-bearing bone applications. In this respect, it can be envisaged that the further reduction of the struts microporosity (e.g. increase of powder content, optimization of the emulsification process) may lead to the improvement of the final mechanical strength.

#### **4.4 Conclusions**

$\beta$ TCP-based colloidal inks suitable for the preparation of 3D printed scaffolds by robotic-assisted deposition were successfully prepared by Branched Copolymer Surfactant (BCS) solutions, emulsification with decane and pH manipulation with Glucono- $\delta$ -lactone (GdL). A Design of Experiment approach was implemented to evaluate the role of BCS, GdL and stirring time on the pH, viscosity and yield stress of the colloidal inks. It was observed that the GdL mainly affects the pH, viscosity and yield stress of the emulsions. Some interactions among the factors were also detected. Microporosity can play a key role in determining the biological response to the materials, but also negatively affects the strength of the scaffold. In this respect, further experiments are required to improve the close packing of the powder particles, thus leading to the increase of the final mechanical performance. A similar approach can be promising to the accurate manipulation of the microstructure and composition of the ceramic scaffolds, allowing the fabrication of materials with tailored features for specific applications.

#### 4.5 References

- [1] Saiz E, Gremillard L, Menendez G, Miranda P, Gryn K, Tomsia AP. Preparation of porous hydroxyapatite scaffolds. *Materials Science and Engineering: C*. 2007;27:546-50.
- [2] Ben-Nissan B. Natural bioceramics: from coral to bone and beyond. *Current opinion in solid state and materials science*. 2003;7:283-8.
- [3] Bohner M, van Lenthe GH, Grunenfelder S, Hirsiger W, Evison R, Muller R. Synthesis and characterization of porous beta-tricalcium phosphate blocks. *Biomaterials*. 2005;26:6099-105.
- [4] Sous M, Bareille R, Rouais F, Clement D, Amedee J, Dupuy B, et al. Cellular biocompatibility and resistance to compression of macroporous beta-tricalcium phosphate ceramics. *Biomaterials*. 1998;19:2147-53.
- [5] Deville S, Saiz E, Tomsia AP. Freeze casting of hydroxyapatite scaffolds for bone tissue engineering. *Biomaterials*. 2006;27:5480-9.
- [6] Leong KF, Cheah CM, Chua CK. Solid freeform fabrication of three-dimensional scaffolds for engineering replacement tissues and organs. *Biomaterials*. 2003;24:2363-78.
- [7] Bose S, Vahabzadeh S, Bandyopadhyay A. Bone tissue engineering using 3D printing. *Materials Today*. 2013;16:496-504.
- [8] Sachs EM, Haggerty JS, Cima MJ, Williams PA. Three-dimensional printing techniques. Google Patents; 1993.
- [9] Hollister SJ. Porous scaffold design for tissue engineering. *Nature materials*. 2005;4:518-24.
- [10] Wegst UG, Bai H, Saiz E, Tomsia AP, Ritchie RO. Bioinspired structural materials. *Nature materials*. 2015;14:23-36.
- [11] Smay JE, Cesarano J, Lewis JA. Colloidal inks for directed assembly of 3-D periodic structures. *Langmuir*. 2002;26.
- [12] Miranda P, Pajares A, Saiz E, Tomsia AP, Guiberteau F. Mechanical properties of calcium phosphate scaffolds fabricated by robocasting. *J Biomed Mater Res A*. 2008;85:218-27.
- [13] Warnke PH, Seitz H, Warnke F, Becker ST, Sivananthan S, Sherry E, et al. Ceramic scaffolds produced by computer-assisted 3D printing and sintering: characterization and biocompatibility investigations. *J Biomed Mater Res B Appl Biomater*. 2010;93:212-7.
- [14] Weaver JVM, Rannard SP, Cooper AI. Polymer-Mediated Hierarchical and Reversible Emulsion Droplet Assembly. *Angewandte Chemie-International Edition*. 2009;48:2131-4.
- [15] Woodward RT, Chen L, Adams DJ, Weaver JVM. Fabrication of large volume, macroscopically defined and responsive engineered emulsions using a homogeneous pH-trigger. *Journal of Materials Chemistry*. 2010;20:5228-34.
- [16] Woodward RT, Weaver JVM. The role of responsive branched copolymer composition in controlling pH-triggered aggregation of "engineered" emulsion droplets: towards selective droplet assembly. *Polymer Chemistry*. 2011;2:403-10.
- [17] Garcia-Tunon E, Barg S, Bell R, Weaver JVM, Walter C, Goyos L, et al. Designing Smart Particles for the Assembly of Complex Macroscopic Structures. *Angewandte Chemie-International Edition*. 2013;52:7805-8.

- [18] Pocker Y, Green E. Hydrolysis of D-Glucono-Delta-Lactone .1. General Acid-Base Catalysis, Solvent Deuterium-Isotope Effects, and Transition-State Characterization. *Journal of the American Chemical Society*. 1973;95:113-9.
- [19] Pocker Y, Green E. Hydrolysis of D-Glucono-Delta-Lactone .2. Comparative Studies of General Acid-Base Catalyzed-Hydrolysis of Methylated Derivatives. *Journal of the American Chemical Society*. 1974;96:166-73.
- [20] Andrade JC, Camilli JA, Kawachi EY, Bertran CA. Behavior of dense and porous hydroxyapatite implants and tissue response in rat femoral defects. *J Biomed Mater Res*. 2002;62:30-6.
- [21] He X, Su B, Tang ZH, Zhao B, Wang XY, Yang GZ, et al. The comparison of macroporous ceramics fabricated through the protein direct foaming and sponge replica methods. *Journal of Porous Materials*. 2012;19:761-6.
- [22] Hyers R, SanSoucie M. Porous calcium phosphate networks for synthetic bone material. Google Patents; 2010.
- [23] Misch CE, Qu Z, Bidez MW. Mechanical properties of trabecular bone in the human mandible: implications for dental implant treatment planning and surgical placement. *Journal of oral and maxillofacial surgery : official journal of the American Association of Oral and Maxillofacial Surgeons*. 1999;57:700-6; discussion 6-8.



# Chapter 5

## DEVELOPMENT OF APATITIC BONE CEMENTS

---

The calcium phosphate bone cements (CPCs) have been widely studied in the last decades as injectable materials for minimally invasive surgery to assist the regeneration of bone. In this chapter, the preparation of a novel Sr-doped apatitic formulation is reported: Sr-substituted  $\alpha$ TCP phases, designed to be the unique cement inorganic precursors, were prepared and mixed with appropriate amount of sodium alginate solutions.

A chemico-physical, morphological, mechanical and biological characterization was carried out on the formulation complying with the clinical requirements, in comparison with a polymer-free commercial CPC. The effect of chemical composition and some processing parameters on the setting times and compressive strength of Sr-containing apatitic bone cements was also investigated according to a Design of Experiment approach.

### 5.1 Preparation of Sr-doped Calcium Phosphate bone cements (CPCs)

In the development of CPCs, the method based on the hydrolysis and transformation of  $\alpha$ - $\text{Ca}_3(\text{PO}_4)_2$  ( $\alpha$ TCP) into elongated calcium-deficient hydroxyapatite (CD-HA) particles is particularly interesting and promising [1].

However, due to critical synthesis conditions, commercial  $\alpha$ -TCP, reagent or biomedical grade, are very scarce. This forces researchers and developers to synthesize it themselves.

It is well documented that some ionic substitutions may exert a drastic effect on the thermodynamic relationships between  $\alpha$ - and  $\beta$ -TCP [2]. For example, partial

substitution of Mg for Ca in TCP increases the thermal stability of the  $\beta$ -phase and gives rise to a binary phase field where  $\beta + \alpha$ -TCP solid solutions coexist [3].

In the same way, partial substitutions of Zn and Sr ions for Ca have a similar effect to Mg [4]. In order to locally evoke a specific cellular response based on the cell-material interaction, nowadays the research on bone cements is focused on the synthesis of ion-doped calcium phosphate cements able to transform into ion-doped apatite upon injection.

Among the various ions, strontium has been proposed to possess both a bone formation stimulating and at the same time anti-resorptive effect and is thus used in systemic osteoporosis therapy [5] (Fig.5.1).

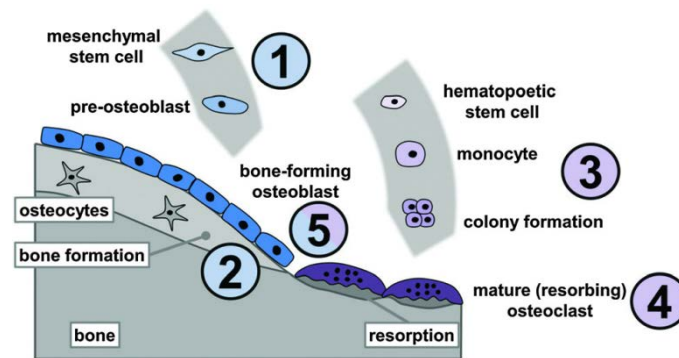


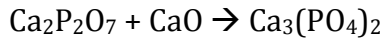
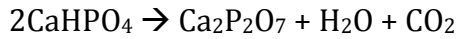
**Fig.5.1 - Effects of Sr<sup>2+</sup> ions on bone metabolism: stimulation of osteoblast precursor proliferation and osteogenic differentiation (1), increase of bone mineralization by osteoblasts (2), reduced osteoclast-precursor recruitment and osteoclastogenesis (3), decreased resorption activity and increased apoptosis of mature osteoclasts (4) as well as interaction with the osteoblast/osteoclast paracrine signalling (5) [6].**

### 5.1.1 Synthesis and characterization of Sr- $\alpha$ TCP phases

Sr-substituted  $\alpha$ -TCP powders with different strontium content (i.e. Sr/(Ca+Sr) = 0, 2, 5, 10 mol%, henceforth coded as Sr0, Sr2, Sr5 respectively) were synthesized by solid state reaction of stoichiometric amounts of calcium carbonate (CaCO<sub>3</sub>, Carlo Erba, Italy), calcium hydrogen phosphate (CaHPO<sub>4</sub>, Sigma Aldrich) and strontium carbonate (SrCO<sub>3</sub>, Carlo Erba, Italy) [7, 8], following the reaction:



During the thermal treatment, the decomposition of the initial reactants occurs, according to:



The powders were firstly dry mixed for 30 minutes, then uniaxially pressed to form pellets, and finally treated at 1400 °C for 1 hour (Fig.5.2).

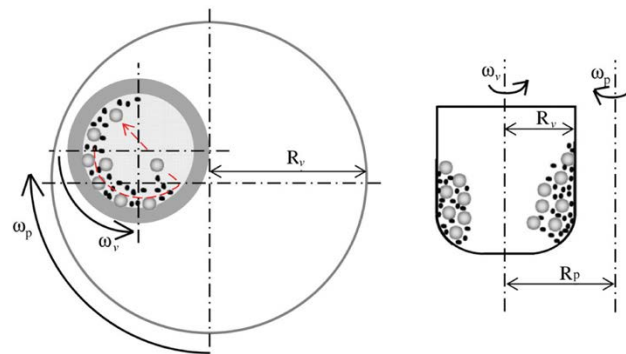


Fig.5.2 – FCN Furnace with mobile crucible (Nannetti, Faenza, Italy)

After the firing, the pellet was removed from the hot furnace and placed in a large pan where it was rapidly crushed with a pestle within a few seconds. Then, the final product was ground, sieved under 150 $\mu\text{m}$  and further milled by planetary mono mill (Pulverisette 6 classic line, Fritsch, Germany) (Fig.5.3).



(a)



(b)

Fig.5.3 – Planetary mono mill Pulverisette 6 classic line, Fritsch, Germany (a); schematic diagram of the planetary ball mill and the jar (b)

The planetary ball mill owes its name to the planet-like movement of its vial (s) (Fig.5.3). Since the vials and the supporting disc rotate in opposite directions, the centrifugal forces alternatively act in like and opposite directions. This causes the milling balls to run down the inside wall of the vial – the friction effect, followed by the material being milled and milling balls lifting by of and travelling freely through the inner chamber of the vial and colliding against the opposite inside wall [9].

The transfer of mechanical energy to the powder particles results in introduction of strain into the powder through generation of dislocations and other defects which act as fast diffusion paths. Additionally, refinement of particle and grain sizes occurs, and consequently the diffusion distances are reduced. Further, a slight rise in powder temperature occurs during milling.

The powders were dispersed in pure ethanol, to inhibit  $\alpha$ TCP transitions to hydrated phases, while preserving the heating of the material during milling. The powders were milled for 50 minutes at 400 rpm using a zirconia jar with 5 mm diameter grinding media (ball-to-powder weight ratio = 2).

### 5.1.2 Synthesis of aqueous setting solutions

In this work, aqueous solutions containing 5%wt of  $\text{Na}_2\text{HPO}_4$  (Sigma Aldrich), enriched with 2 wt% of sodium alginate (Alginic Acid Sodium Salt from Brown Algae, Sigma Aldrich) were prepared and mixed with the powders to obtain the cements.

### 5.1.3 Liquid-On-Powder Ratio And Mixing Procedure

The microstructure and porosity of CPCs can be tuned by adjusting some processing parameters, such as the particle size of the powder phase and the liquid-on-powder ratio (L/P). The reactivity of the powder increases when decreasing its particle size, due to an increase in its specific surface area [10]. This results in a higher supersaturation degree achieved in the cement paste, which favors crystal nucleation and results in the precipitation of more numerous and smaller needle-like crystals, instead of the larger plate-like crystals formed when

big particles are used. These different microstructures give rise to different pore size distributions in the set cements (Fig.5.4).

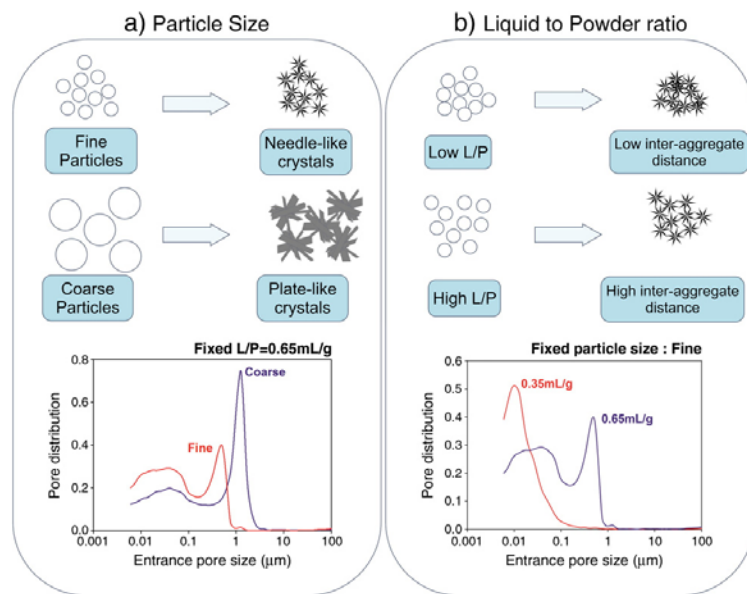


**Fig.5.4 – Effect of particle size and liquid-on-powder ratio on the CPC microstructure [10]**

For the same L/P ratio and different powder size, the total porosity of the cement remains constant, but smaller pores are formed in the fine cement (i.e. using small particles). Another way of tuning the porosity and the pore size distribution of the CPCs is by varying the L/P ratio. At low L/P ratios the space between particles in the blend decreases. Considering that the precipitation of HA crystals takes place surrounding the initial powder particles, this leads to a more compact structure of crystal agglomerates. In contrast, when the L/P ratio increases, the total porosity of the cements increases and larger pores are formed due to the augmented separation between aggregates resulting from the larger distance between the original  $\alpha$ -TCP particles.

In this work, a formulation able to meet the clinical requirements in terms of setting times was prepared with L/P=0.48 and a robust characterization was performed in comparison with a commercial polymer-free CPC (KyphOs FS™, Medtronic Spine LLC, Minneapolis, MN, USA) [1]. The investigation of chemical composition and some powder milling parameters on the setting times and compressive strength of the cements was also carried out with L/P=0.55, to ensure the complete injectability of cements with different particle size precursors.

The mixing procedures of the cement components was optimized in order to define a repeatable protocol suitable for the operating theatre, by adopting a commercial Bone Cement Delivery System equipment (P-system, Medmix, Switzerland) (Fig.5.5).



**Fig.5.5 – Bone Cement Delivery System equipment (P-system, Medmix, Switzerland)**

Before mixing, solid and liquid components were also treated with  $\gamma$  irradiation (25 kGy) and autoclaving (121 °C for 20 minutes), respectively, in order to produce sterile materials with a repeatable procedure for the operating theatre.

## 5.2 Results and Discussion

### 5.2.1 Characterization of the Sr-doped CPCs

The chemical analysis of the Sr- $\alpha$ TCP phases confirmed the presence of strontium in amounts very close to the nominal composition of the starting mixture (Table 5.I).

**Table 5.I. Chemical analysis of the cements precursor powders**

Cement	Nominal Sr/(Ca+Sr) (mol%)	Actual composition		
		Ca/P (mol)	(Sr + Ca)/P (mol)	Sr/(Ca+Sr) (mol %)
Sr0	0	1.51 ± 0.01	1.51 ± 0.03	0
Sr2	2	1.44 ± 0.02	1.46 ± 0.02	1.91 ± 0.03
Sr5	5	1.40 ± 0.03	1.46 ± 0.02	4.95 ± 0.02
KyphOs	-	1.24 ± 0.01	1.26 ± 0.03	2.67 ± 0.02

The phase composition and the lattice parameters of the precursor powders were investigated by X-ray diffraction patterns, evidencing peaks mainly ascribed to  $\alpha$ -TCP and  $\beta$ -TCP phases (Fig.5.6).

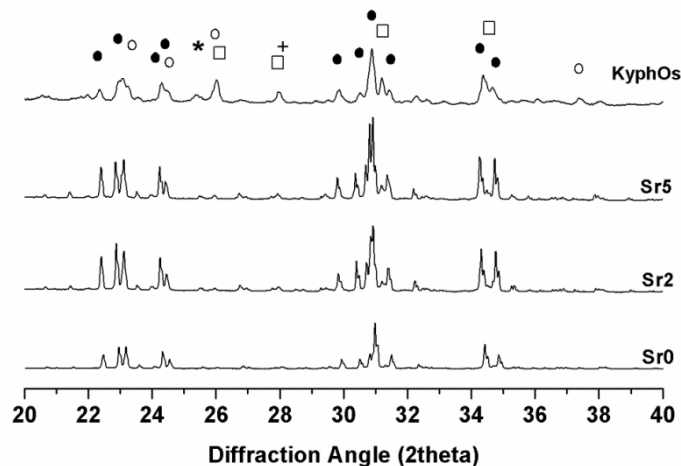


**Fig.5.6 - XRD patterns of the cement precursor powders. Peaks legend: Sr- $\alpha$ TCP (●), Sr- $\beta$ TCP (□), HA (x), SrCO<sub>3</sub> (\*), Mg<sub>3</sub>(PO<sub>4</sub>)<sub>2</sub> (○), MgHPO<sub>4</sub> (+)**

The Sr-doped powders prepared in this work exhibited only a slight increase in the amount of  $\beta$ TCP phase with increasing the strontium content (estimated between 8wt% and 12wt%). Conversely, the KyphOs cement also contained SrCO<sub>3</sub>, Mg<sub>3</sub>(PO<sub>4</sub>)<sub>2</sub> and MgHPO<sub>4</sub> phases, as reported in [1].

The formation of Sr- $\alpha$ TCP precursors upon solid state synthesis at high temperature and subsequent fast cooling was accompanied by crystallization of the  $\beta$ TCP polymorph, thermodynamically stable below 1125 °C [11, 12], especially due to the presence of strontium, which has a recognized ability to promote the  $\beta$ TCP formation [3, 13]. However, in spite  $\beta$ TCP did not take active part to the setting mechanisms, its presence in small amounts did not hamper significantly the setting properties of the cement, thus successfully achieving setting times compliant with the requirements relevant for the clinical practice.

The phase composition and the lattice parameters of the cements, obtained after 7 days of immersion in Hanks' balanced salt solution (H6648, Sigma Aldrich) at 37°C, were investigated by Bruker D8 Advance.

The diffraction patterns of the cements evidenced the complete transformation of  $\alpha$ TCP into nanocrystalline HA (Fig. 5.7) after 7 days of soaking, while  $\beta$ TCP content remained unchanged.

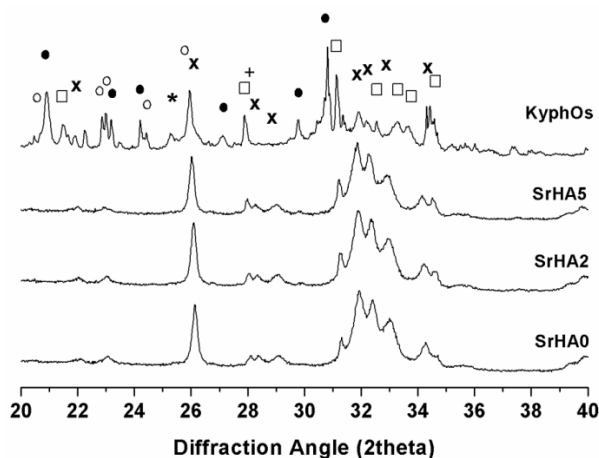


**Fig.5.7 – XRD patterns of the hardened cements, 7 days after soaking.**  
**Peaks legend: Sr- $\alpha$ TCP (●), Sr- $\beta$ TCP (□), HA (x), SrCO<sub>3</sub> (\*), Mg<sub>3</sub>(PO<sub>4</sub>)<sub>2</sub> (○), MgHPO<sub>4</sub> (+)**

A slight and continuous peaks shift towards higher d values was also detected with increasing the Sr amount. The control cement exhibited SrCO<sub>3</sub>, Mg<sub>3</sub>(PO<sub>4</sub>)<sub>2</sub> and MgHPO<sub>4</sub> phases in addition to  $\alpha$ TCP and  $\beta$ TCP, as reported elsewhere [1]. The cements developed in this work underwent complete transformation of  $\alpha$ TCP into HA after 7 days of soaking, whereas the control cement still exhibited peaks belonging to the precursor phases, thus indicating incomplete transformation (Fig.5.6).

The injectability of the cements was qualitatively evaluated by measuring the amount of cement in the syringe after extrusion, according to [14]. The initial and final setting times of the cements (henceforth indicated as  $T_{in}$  and  $T_{fin}$ , respectively) were evaluated by using Gillmore apparatus (Fig.5.8), according to ASTM C266-99, testing 5 specimens for each composition, upon immersion in Hanks' solution at 37 °C.



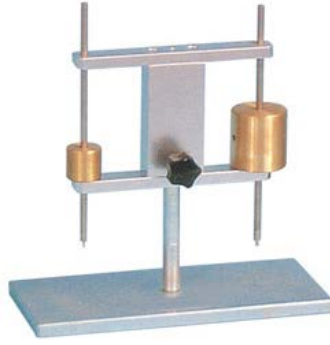


**Fig.5.8 - Gillmore apparatus to measure the setting times of cements**

The cements showed complete injectability after extrusion through 13 Gauges needles, i.e. the totality of the paste could be extruded from the syringe without de-mixing; it was also found that the setting times were strongly influenced by the amount of incorporated strontium (Table 5.II).

**Table 5.II. Initial and final setting times of the cements.**

<b>Cement</b>	<b>T<sub>in</sub> (minutes)</b>	<b>T<sub>fin</sub> (minutes)</b>
<b>Sr0</b>	9 ± 2	14 ± 2
<b>Sr2</b>	11 ± 2	22 ± 3
<b>Sr5</b>	29 ± 4	47 ± 5
<b>KyphOs</b>	12 ± 2	23 ± 1

The average domain size of the crystalline phases was  $270 \pm 40$  nm for  $\alpha$ TCP and  $75 \pm 15$  nm for  $\beta$ TCP. No significant variations of the domain size of TCP polymorphs in function of the Sr content was detected. In the HA phase the peak width of (300) and (002) reflections ( $d \cong 2.72$  and  $3.44$  Å, respectively) were separately evaluated, thus achieving the size of coherent domains along both the ab plane and the c axis. It was found that the introduction of strontium induce a slight increase of the domain sizes (Fig.5.9a) and cell volume (Fig.5.9b), associated also with slight crystal deformation (Fig. 5.9c).

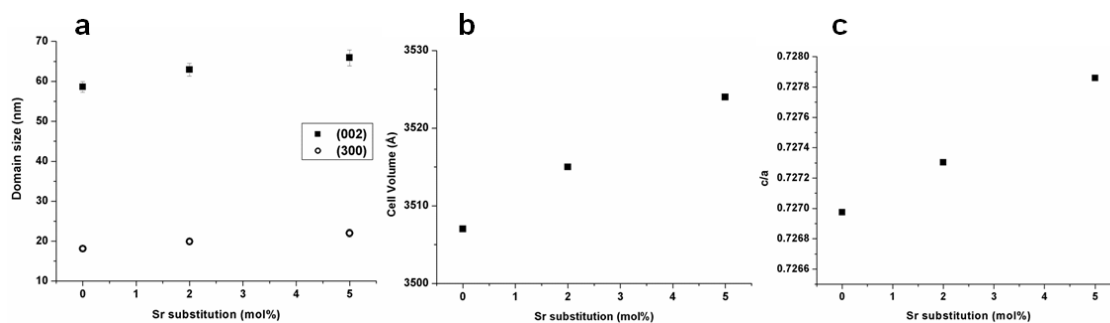


**Fig.5.9 - a) Size of the coherent domain of the HA lattice along the (002) and (300) directions; b) cell volume of HA phase in Sr-HA cements; c) c/a ratio vs. Sr content in Sr-HA cements.**

In respect to the effect of strontium doping, a retard in the setting behaviour has been observed (Tab.3), thus confirming the actual substitution in the HA lattice, as also previously observed by [6, 15]. Strontium substitution in the HA lattice was also confirmed by the increase of cell volume, highlighted by the general shift of XRD peaks towards higher  $d$  values with increasing the Sr amount, due to the larger ionic radius of strontium, if compared with calcium ( $\text{Sr}^{2+}$  ionic radius = 0.113 nm;  $\text{Ca}^{2+}$  ionic radius = 0.099 nm) [8]. Besides, the introduction of strontium ions provoked a slight deformation of the HA lattice, thus resulting in anisotropic crystal growth along the  $c$  axis, as highlighted by the progressive increase of  $c/a$  with the strontium content (Fig.5.9c), whereas the general domain size was not significantly affected by the strontium concentration in the calcium crystals sites, at least up to 5 mol% (Fig.5.8a). This finding further supports the actual Sr-substitution in the HA lattice, as also evidenced by [16].

Then, the biocompatibility of the cements was preliminarily assessed in collaboration with the biologists of ISTECCNR. In this respect, human osteoblast-like cell line, MG63 cell line, purchased from Lonza (Italy) were cultured in Dulbecco Modified Eagle's (DMEM)/F12 Medium (Gibco), containing penicillin-streptomycin (100 U/ml-100  $\mu\text{g}/\text{ml}$ ) supplemented with 10% foetal bovine serum (FBS) and kept at 37°C in an atmosphere of 5%  $\text{CO}_2$ . For the experiments, cells were plated at  $1.5 \times 10^4/\text{cm}^2$  and cultured for up to 3 days. Cement discs were sterilized with 3 washes in ethanol 70 % for 20 min followed by 3 washes in PBS 1X for 10 min each. Samples were then air dried and sterilized by UV irradiation for 30 min per side under laminar flow hood and preconditioned for three days in

cell culture medium supplemented with FBS and penicillin-streptomycin. Live/Dead assay and cell morphological evaluation was also performed according to [17].

The intracellular esterase activity and plasma membrane integrity were preserved. A very high ratio of viable cells was seen with no significant differences among the tested cements. Only few dead cell (stained in red) were observed (Fig.5.10a-c). Analysis of cell morphology carried out with SEM reported similar results: Fig. 5.10d show a nearly complete coverage of Sr2 cement by cells, whereas Fig. 5.10e shows a detail of cell plasma extension.

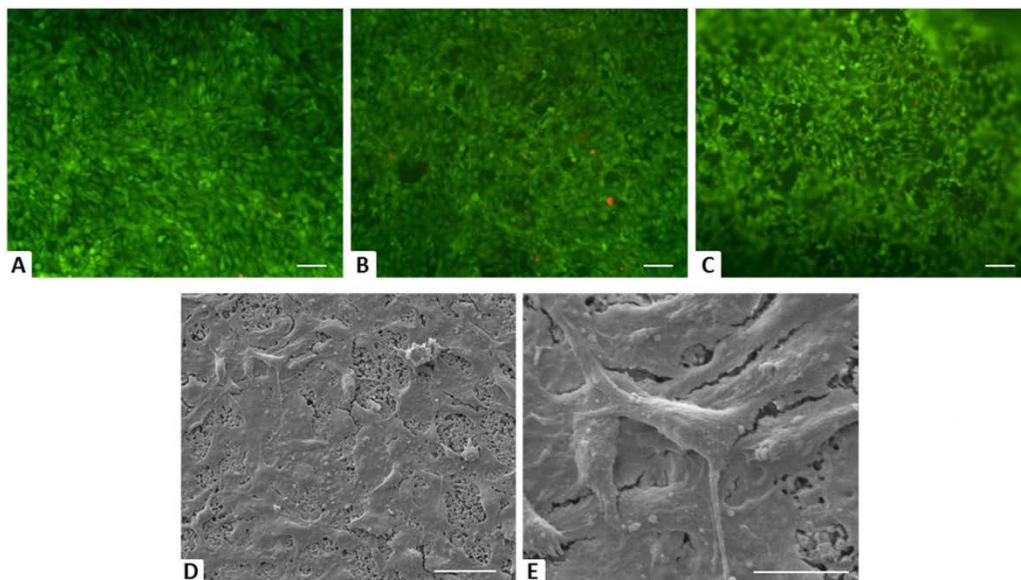


**Fig.5.10 - *In vitro* study - Cell viability was analysed by the Live/Dead assay. Calcein AM stains for live cells in green, EthD-1 stains for dead cells in red. (A) Sr0%; (B) Sr2% and (C) Sr5% (scale bars: 100 $\mu$ m). Analysis of cell morphology assessed by SEM, (D) MG63 grown for 3 days on Sr2% surface (scale bar: 50  $\mu$ m), with a detail of cell plasma extensions (E) (scale bar: 20  $\mu$ m).**

A good biocompatibility of the KyphOs cement, already used in clinical applications, was previously assessed [18, 19]. On this basis, Sr2 was selected for *in vivo* testing, as Sr-doped formulation with setting behaviour compliant with the requirements for the clinical practice.

The compressive strength and Young's modulus of cements were evaluated by testing cylindrical specimens (diameter = 8mm; height = 17mm) after 1 and 3 days soaking in Hanks' balanced salt solution at 37 °C. Five specimens were tested for

each cement and timepoint by using a universal testing machine (MTS Insight 5, Minnesota, USA) with a crosshead speed of 0.5 mm/min. The Young's modulus was approximated by calculating the slope of the linear, elastic portion of the stress-strain curves. The porosity percentage was evaluated on the cylindrical specimens immersed in Hanks' balanced salt solution at 37°C for 3 days, as  $P=1-\rho/\rho_0$ , where  $\rho$  is the cement density calculated as weight-on-volume ratio and  $\rho_0$  is the theoretical density of the hydroxyapatite phase (3.16 g/cm<sup>3</sup>).

As setting times shorter than 30 minutes are usually required for clinical applications, [20, 21] only Sr0 and Sr2, in comparison with KyphOs, were mechanically tested (see Table 2) on cylindrical specimens (diameter=9mm, height=17mm).

The KyphOs cement exhibited significantly higher compressive strength and Young's modulus than Sr0 and Sr2 (Fig.5.11).

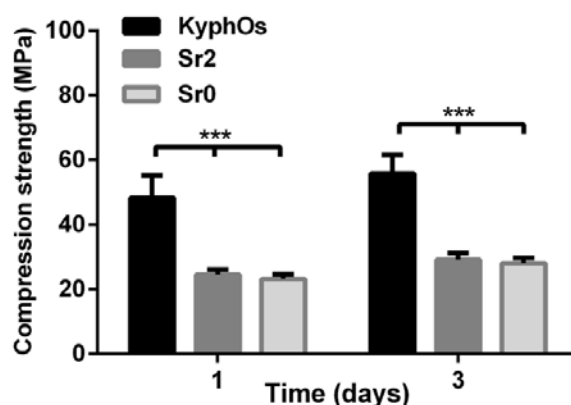


**Fig.5.11 - Evaluation of compressive strength of the studied cements**

In this respect, the estimated Young's modulus after 3 days were  $E_{KYPHOS}=3.6\pm0.5$  GPa,  $E_{Sr0}=2.3\pm0.7$  GPa and  $E_{Sr2}=2.6\pm0.4$  GPa. Sr0 and Sr2 cements exhibited a porosity extent of ~48%, resulting significantly higher than KyphOs (~31%).

The setting of apatite cements is mainly based on the physical interlocking of nanosized CD-HA crystals that heterogeneously nucleate and grow on the surface of  $\alpha$ TCP grains, with typical flaky- to needle-like morphology and open micron-sized porosity [8, 10, 22, 23]. In the present work such microstructures were observed for the new cements, without significant differences induced by the

introduction of strontium (Fig.5.12). Conversely, KyphOs exhibited a more close-packed microstructure without evidence of elongated particles.

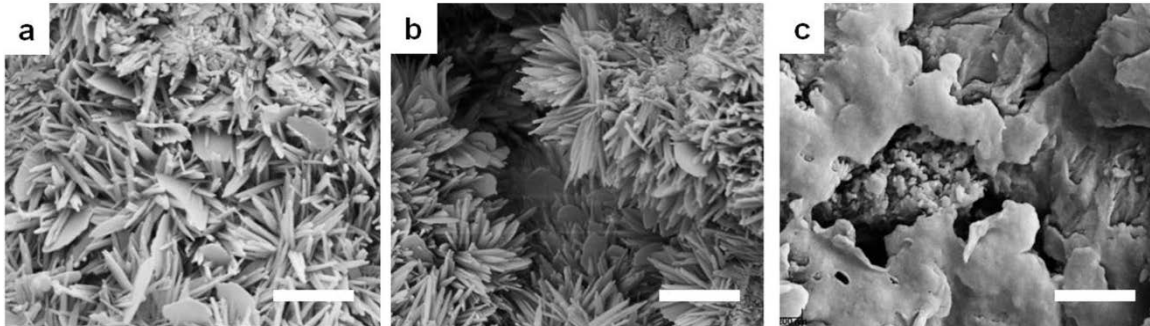


**Fig.5.12 – Microstructure of the cements after 7 days of immersion at 37 °C in Hank's Balanced solution. a) Sr0, b) Sr2; c) KyphOs. Scale bar = 500nm**

Conversely, KyphOs exhibited a more close-packed microstructure without evidence of elongated particles.

In this respect, considering that no effects related to different amounts of strontium can be addressed (Table 1), it can be supposed that the difference in the cement microstructure is ascribable to the incomplete transformation of KyphOs precursor.

The *in vivo* performance of the Sr2 and KyphOs cements were evaluated by surgeons of Policlinico Gemelli – Università Cattolica Sacro Cuore (Roma) after implantation of Sr2 and KyphOs in 3 New Zealand White (NZW) male rabbits (weighing about 3 Kg) for each cement. The tests were conducted with previous approval of the institutional Ethical Committee strictly following Italian (Law by Decree, 27 January 1992, No.116), European (Directive 86/609/EEC) and International Laws and Regulations (ISO 10993-2-Animal Welfare Requirements). The cements were implanted according to a previously reported procedure [24-26]. Briefly, a blind tunnel (diameter = 4 mm; length = 8 mm) was firstly aseptically created under fluoroscopic control by a surgical drill in the metaepiphyseal distal zone of both femurs, then irrigated with a saline solution and filled by injection with the cements. All the procedures were performed under general anaesthesia.

At 4 weeks after surgery, the animals were pharmacologically euthanized with intravenous administration of Tanax, under general anaesthesia. The femurs were

then harvested and all surrounding soft-tissue was removed. The presence of deformities or fractures and the bone-cement interface were investigated. For histological analysis, the harvested specimens were fixed in phosphate-buffered 4% paraformaldehyde and stored at 4° C for 12 hours until processing. Then, the specimens were embedded in Technovit 7200, according to the manufacturers protocol (Exakt, Germany). Using a saw microtome (Leica Microsystems Srl, Italy), three consecutive central sections ( $30 \pm 10 \mu\text{m}$ ) were cut and stained with toluidine blue. The region of interest (ROI) was made by tracing over the material followed by a 100 pixels increase to include the bone-cement interface.

The microscopic examination was performed by an optical microscope (Carl Zeiss Axioscop 40 equipped with AxioCam ICC 3 Zeiss) and Axiovision 4.8 software.

Standard terms and nomenclature for bone histomorphometric analysis were used, according to [27] (Table 5.III).

**Table 5.III - Terms and nomenclature for histomorphometric analysis**

<b>Parameter</b>	<b>Abbreviation</b>	<b>Formula</b>
Material Perimeter	M-Pm	
Bone Material Contact Length	BMC-Le	
Bone Pores Length	BPo-Le	
Material Diameter	M-Dm	
Bone Material Contact Rate	BMCR	$(\text{BMC-Le} / \text{M-Pm}) \times 100$
Bone Penetration Rate Length	BPR-Le	$(\text{BPo-Le} / (\text{M-Dm}/2)) \times 100$

The histological analysis of the explants at 4 weeks after the injection *in vivo* evidenced a positive interaction of both cements with the surrounding bone tissue, without signs of inflammatory processes, fractures or infections. The penetration of bone tissue was more evident for Sr2 cement (Fig.5.12 a,c). The histological analysis showed enhanced deposition of new bone around Sr2 cement, if compared with KyphOs (Fig.5.13 b,d).

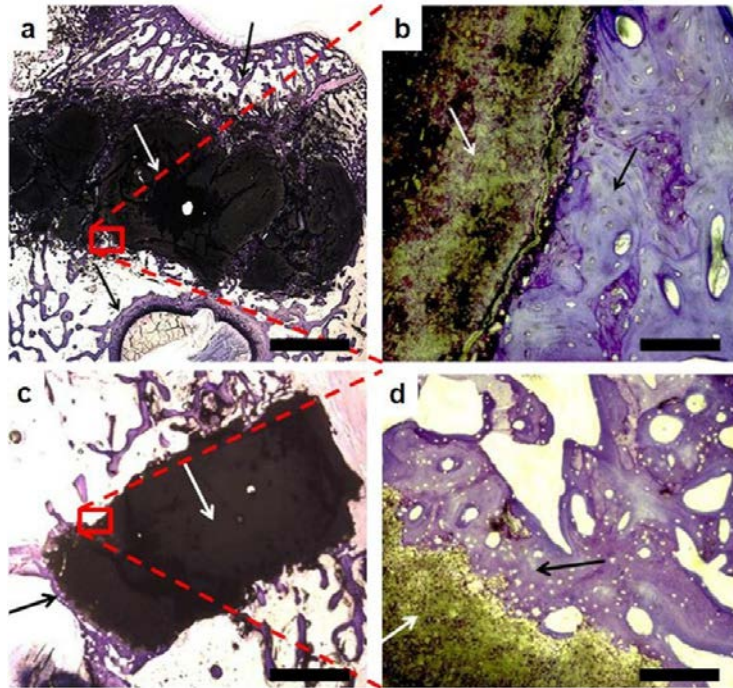


**Fig.5.13 - Optical microscopic view of explanted Sr2 (A,B) and KyphOs (C,D) at 4 weeks after implantation. Cements and surrounding bone are indicated with white and black arrows, respectively. Scale bars (A,C = 2mm, B,D = 100 $\mu$ m)**

In addition, the histomorphometric analysis showed a significantly higher bone penetration for Sr2 (Fig.5.14).

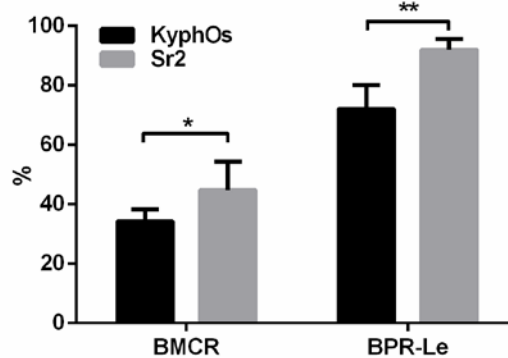


**Fig.5.14 - Histomorphometric results of samples obtained at 4 weeks after implantation**

The XRD analysis of the explanted Sr2 and KyphOs specimens revealed that Sr2 underwent complete transformation of  $\alpha$ -TCP into HA also *in vivo*, so that only low-crystallinity HA and unreacted  $\beta$ TCP were detected in the implant site (Fig. 5.15). Besides, a significant peak broadening in the HA profile was detected, suggesting a decrease in the crystal ordering, particularly when compared with the HA phase

obtained after cement soaking for 7 days in Hanks' solution (see Fig. 5.6). In particular, the domain size along (300) direction (i.e. the  $ab$  plane) was reduced from  $19.9\pm 0.7$  to  $9.6\pm 1.8$  nm, whereas along the (002) direction (i.e. the  $c$  axis) it decreased from  $62.9\pm 1.6$  to  $34.3\pm 2.2$  nm. The explanted tissue treated with KyphOs showed the presence of low-crystallinity HA phase, but associated with significant amount of residual precursor phases that made not possible the evaluation of peak broadening.

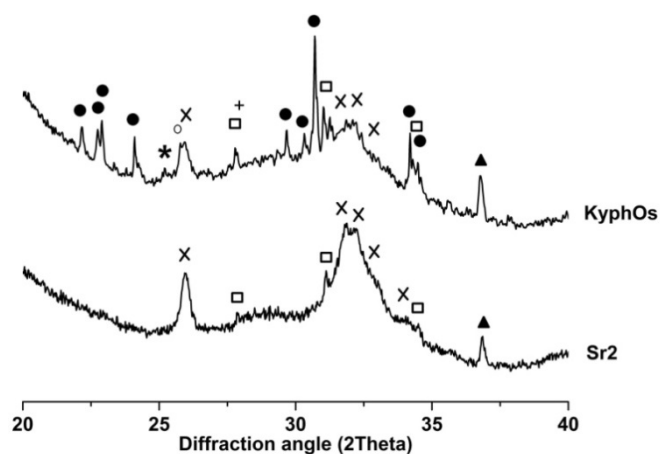


**Fig.5.15 - XRD patterns of explanted Sr2 and KyphOs specimens at 4 weeks after implantation. Peaks legend:  $\alpha$ -TCP(●),  $\beta$ -TCP(□), HA (x),  $\text{SrCO}_3$  (\*),  $\text{Mg}_3(\text{PO}_4)_2$  (○),  $\text{MgHPO}_4$ (+), aluminium of the sample-holder support (▲)**

Also, SEM analysis of the explants highlighted marked difference in the cement morphology (Fig.5.16), thus confirming the findings related to the cements microstructure after hardening *in vitro* (Fig.5.12).

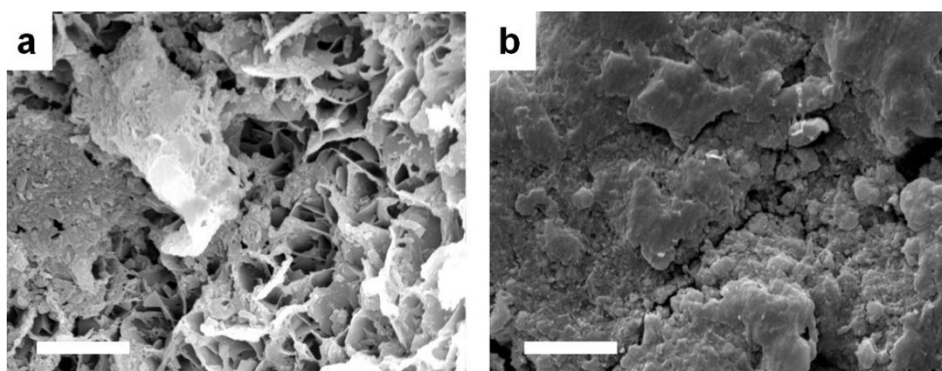


**Fig.5.16 - Microstructure of Sr2 (a) and KyphOs (b) cements at 4 weeks after implantation in vivo (scale bar=5 $\mu\text{m}$ )**



The different morphology of Sr2 and control cement after hardening *in vitro* was confirmed by compositional and morphological analysis of the tissue explants after 4 weeks *in vivo* (Fig.5.13 and 5.14). In this respect, complete transformation of  $\alpha$ TCP into HA was detected for Sr2 (Fig.5.7), associated with a more extensive microporosity (Fig.5.12). It can be hypothesized that the more extensive transformation of the cement precursors in needle-like HA crystals and the presence of a bio-erodible polymer such as alginate, have played a key role in the occurrence of discontinuities within the Sr2 cement *in vivo*, leading to an enhanced penetration of bone tissue, if compared with KyphOs (Fig.5.13 and 5.14).

It can be also hypothesized that the multi-phase composition of the KyphOs precursor may have hampered extensive transformation into HA, thus maintaining a more compact microstructure and a reduced porosity, while exhibiting a significantly higher compressive strength (Fig.5.11). However, such features significantly impacted on new bone penetration, possibly limiting the osteointegration of the control cement in the surrounding bone.

In the pursuing of bone regeneration, it is well accepted that the rapid formation of a tight bone-cement interface associated with bone penetration is a main goal [28-30], as well as to prevent the formation of fibrous or necrotic areas into the bone defects [31]. Therefore, in spite of a reduced strength, even though acceptable for many clinical applications [32], the development of bone cements with open, porous microstructure can be considered as a major goal that, particularly in the long term, can result into improved bone healing and recovery of mechanical functionality. In this respect, deeper investigation are required, particularly with longer term *in vivo* assessment, to clarify this assumption and to ascertain the potential of effective bio-resorption.

It can be also observed that the use of single-phase precursors permits the easy tailoring of the amount of strontium introduced in the cement, while improving the osteointegration of the material with the surrounding bone. A further optimization of the rheological properties may open to the development of a platform of bioactive injectable materials with tailored composition and viscosity, with perspective of wide applications in different anatomical compartments such as

vertebral bodies, tibial plateau, proximal humerus, wrist and calcaneus [33] as well as the hip and femoral neck [34].

### 5.2.2 Designing the performance of CPCs

The effect of the strontium amount as well as milling time and milling media diameter on the powder particle size, as well as setting times and compressive strength of Sr-containing apatitic bone cements was investigated according to a Design of Experiment (DoE) approach.

A face-centered composite design was used, and the set of experiment reported in Table 5.IV was implemented.

**Table 5.IV – Design matrix for the experimental design validation conditions and responses.**

Random order	A	B	C	D <sub>50</sub> (µm)	T <sub>in</sub> (min)	T <sub>fin</sub> (min)
5	-1	-1	-1	2.3	13 ± 1	20 ± 1
9	1	-1	-1	2.2	27 ± 2	58 ± 3
10	-1	1	-1	1.5	12 ± 1	18 ± 2
19	1	1	-1	1.4	25 ± 2	56 ± 3
2	-1	-1	1	4.1	18 ± 3	30 ± 2
6	1	-1	1	4.3	35 ± 2	74 ± 3
13	-1	1	1	2.2	16 ± 2	27 ± 2
7	1	1	1	2.1	34 ± 2	71 ± 4
15	0	0	0	2.5	21 ± 2	38 ± 1
17	0	0	0	2.3	22 ± 1	41 ± 3
3	0	0	0	2.4	20 ± 2	40 ± 4
12	0	0	0	2.5	19 ± 2	40 ± 2
18	0	0	0	2.3	20 ± 2	40 ± 3
14	-1	0	0	2.7	15 ± 2	23 ± 2
8	1	0	0	2.6	26 ± 2	62 ± 3
4	0	-1	0	3.1	21 ± 3	48 ± 2
16	0	1	0	1.9	19 ± 1	45 ± 2
11	0	0	-1	1.8	16 ± 2	41 ± 2
1	0	0	1	3.1	23 ± 3	51 ± 2

The planetary ball milling parameters adopted in this activity caused an extensive powder comminution, as showed by the low values of D<sub>50</sub>, if compared with other works [35, 36].

During a planetary ball milling treatment, the reduction in powder size and crystal order occurred by high-energy ball-ball and ball-wall impacts [37, 38], thus leading to highly reactive powders upon mixing with aqueous solutions [39, 40].

The regression analysis of data is reported in Table 5.V. To maximize the responses, the factors with positive coefficients should be increased and those with negative coefficients should be decreased.

**Table 5.V. Results of the regression analysis of data**

	<b>D<sub>50</sub></b>		<b>T<sub>in</sub></b>		<b>T<sub>fin</sub></b>	
	<b>Coefficient</b>	<b>p-value</b>	<b>Coefficient</b>	<b>p-value</b>	<b>Coefficient</b>	<b>p-value</b>
<b>Constant</b>	2.45	0.00	19.86	0.00	41.64	0.00
<b>A</b>	-0.02	0.61	7.31	0.00	20.31	0.00
<b>B</b>	-0.69	0.00	-0.80	0.11	-1.30	0.15
<b>C</b>	0.66	0.00	3.30	0.00	6.00	0.00
<b>AB</b>	-0.04	0.39	0.00	0.99	0.00	0.99
<b>AC</b>	0.04	0.38	1.00	0.06	1.50	0.09
<b>BC</b>	-0.31	0.00	0.00	0.98	-0.25	0.79
<b>A<sup>2</sup></b>	0.14	0.06	1.32	0.16	-1.44	0.38
<b>B<sup>2</sup></b>	-0.01	0.92	0.82	0.37	2.56	0.14
<b>C<sup>2</sup></b>	-0.01	0.41	0.32	0.72	2.06	0.22

As shown, the response were significantly influenced by both the factors and their interactions. Considering the coefficients with  $p < 0.10$ , the regression equation for  $D_{50}$ ,  $T_{in}$  and  $T_{fin}$  are shown in the following equations:

$$D_{50} = 2.45 - 0.69B + 0.66C - 0.31BC + 0.14 A^2$$

$$T_{in} = 19.86 + 7.31A + 3.3C + AC$$

$$T_{fin} = 41.64 + 20.31A + 6C + AC$$

These equations reflect the quantitative influence of the processing variables. The  $R^2$  values indicate the percentage of the variation in the response that can be explained by varying the factors [41, 42].

The statistical analysis for the response showed that the standard error of estimate was 0.11 for  $D_{50}$ , 1.43 for  $T_{in}$  and 2.21 for  $T_{fin}$ . The  $R^2$  values for the observed responses were 0.96, 0.94 and 0.95 for  $D_{50}$ ,  $T_{in}$  and  $T_{fin}$ , respectively, while the

respective  $Q^2$  values were 0.92, 0.88 and 0.91, thus exhibiting a very good fitting quality of the models.

It was observed that a decrease in  $D_{50}$  was mainly achieved by increasing the milling time and decreasing the milling media diameter, probably due to the higher surface area exposed by the spheres [9, 43, 44]. A significant reduction in setting times was obtained by reducing the strontium content and milling media diameter, more than prolonging the milling time (Fig.5.17). A quadratic relationship of the strontium content on  $D_{50}$  was also detected.

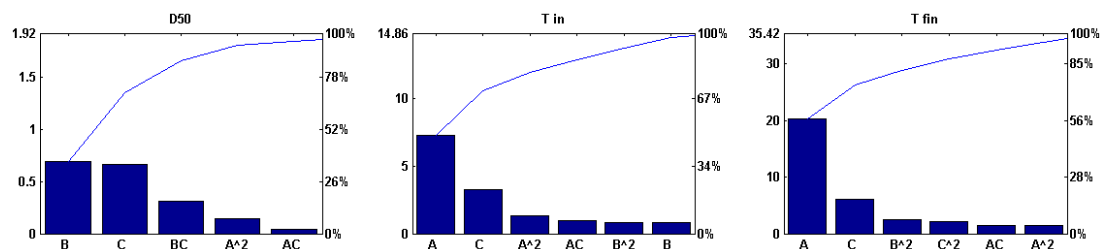


Fig.5.17 - Pareto charts evaluating the effect of experimental parameters on  $D_{50}$ ,  $T_{in}$  and  $T_{fin}$

To investigate the response of the system for combinations not actually run in the experiment, 2D contour plots were also generated (Fig.5.18).

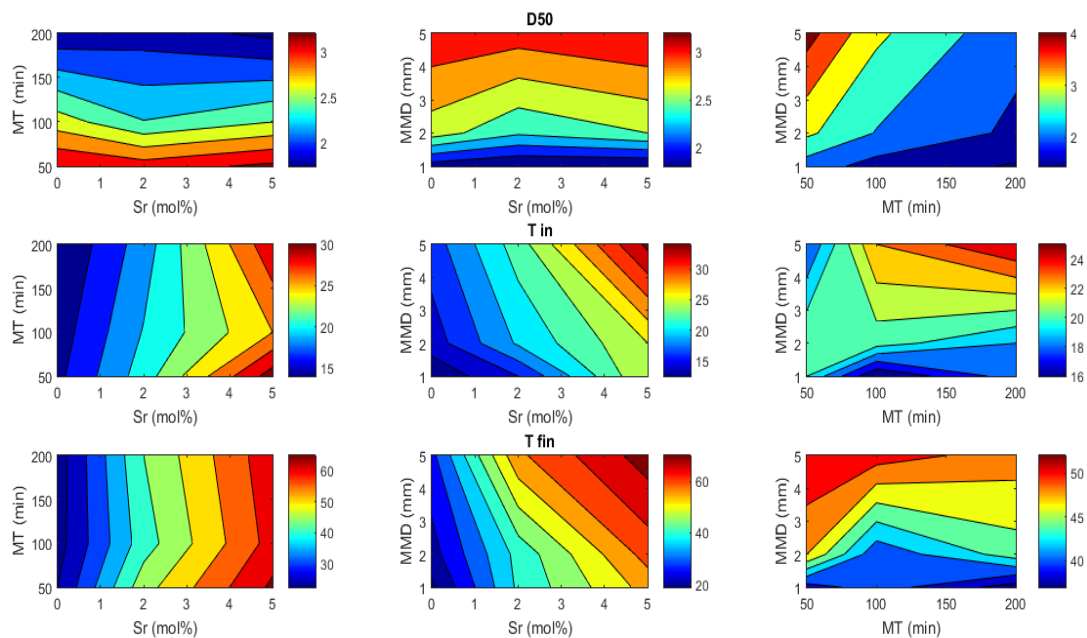


Fig.5.18 - Contour plots for the effects of strontium content, milling time and milling media diameter on the  $D_{50}$  (top row), initial setting time (middle row) and final setting time (bottom row).

From the top to the bottom, the rows refer to  $D_{50}$ ,  $T_{in}$  and  $T_{fin}$ , while the blue and red colors refer to lower and higher response values, respectively. The more the contour lines diverge from horizontal or vertical trends, the more significant is the interaction between the parameters.

Basing on the results obtained so far, the strontium content and the milling media diameter demonstrated to be the most effective parameters in reducing the setting times. In this respect, the mechanical performance of the cements obtained by mixing powders milled for 100 minutes were also investigated.

A significant increase of compressive strength was observed by reducing the milling media diameter, more than varying the strontium amount (Fig.5.19).

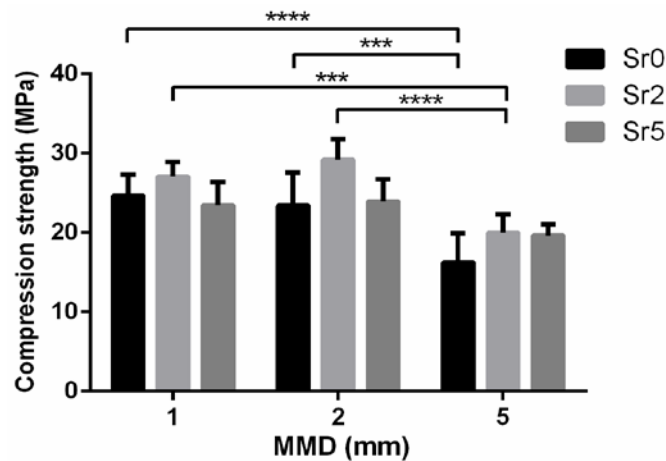


Fig.5.19 – Compressive strength of cements

The higher compressive strength was detected for the Sr2 formulations, achieving comparable strength to apatite-cement formulations reinforced with fibers [32].

The reduction of the compressive strength with the increase in strontium content should be ascribed both to a non-optimal particles hydrolysis and to the increase in the crystals defects due to an excess in the substitution of strontium, as previously supposed [45].

The overall porosity exhibited by the cements was in the range 35-55%, according to the previously reported values for CPCs [46]; a slight porosity decrease occurred by using smaller milling media (Table 5.VI).

**Table 5.VI – Porosity and Young’s modulus of cements with different strontium amounts and milling media diameter**

	Porosity (%)			Young’s modulus (GPa)		
	MMD (mm)			MMD (mm)		
	1	2	5	1	2	5
<b>Sr0</b>	45 ± 2	46 ± 3	53 ± 2	2.2 ± 0.3	2.3 ± 0.2	1.8 ± 0.6
<b>Sr2</b>	44 ± 1	42 ± 2	46 ± 2	2.1 ± 0.3	2.3 ± 0.4	2.0 ± 0.7
<b>Sr5</b>	44 ± 2	47 ± 2	49 ± 1	1.9 ± 0.2	1.8 ± 0.4	1.7 ± 0.4

A flaky to needle-like morphology was detected for each formulation (Fig.5.20).

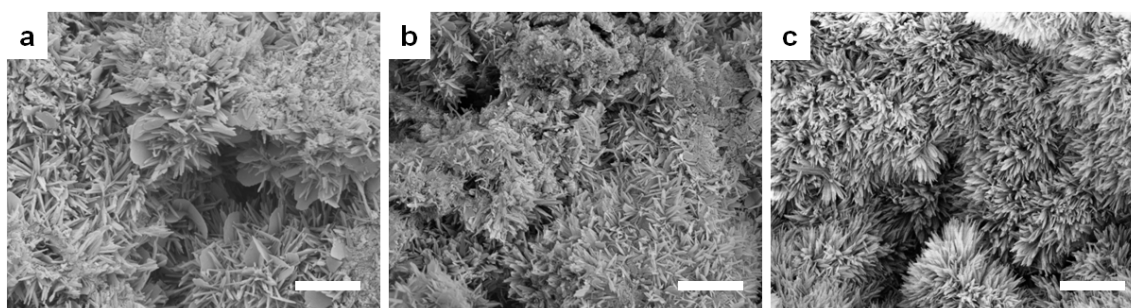


**Fig.5.20 – Morphology of the Sr2 cements obtained by powders milled with different milling media diameter: (a) 5 mm, (b) 2mm, (c) 1mm. Scale bars: 1 μm**

An apparent prevalence of sharp crystals was also appreciated in the cements obtained by mixing finer precursor powders, supporting that the formation of more packed crystal structures occurred in this condition, as previously observed [14, 35, 47].

### 5.3 Conclusions

A novel formulation of strontium-substituted apatitic cement enriched with alginate was proposed, exhibiting complete injectability, fast setting and stable mechanical performance. An extensive microstructure was shown to enhance the bone formation and penetration, thus suggesting that, in spite remarkable mechanical strength is required to address load-bearing application, cements with a too compact structure may significantly limit the extent of new bone penetration. In this respect, the ability to undergo complete transformation into HA phase and the presence of a bio-erodible polymer in the cement formulation can be two key features relevant for achieving substantial bone regeneration throughout the whole injected cement mass. It was also observed that the particle size of

precursor powders of CPCs was mainly affected by the milling parameters, while the setting times were primarily influenced by the strontium doping. Smaller milling media diameter reflected in stronger cements, with extensive interlocking of needle-like crystals. On this basis, the present work elucidates the interaction effect of some processing parameters of CPCs, in order to overcome the technological limitations that are hampering their clinical applications.

#### **5.4 References**

- [1] Bohner M. Design of Ceramic-Based Cements and Putties for Bone Graft Substitution. *European Cells & Materials*. 2010;20:1-12.
- [2] Carrodeguas RG, De Aza S. alpha-Tricalcium phosphate: synthesis, properties and biomedical applications. *Acta Biomater*. 2011;7:3536-46.
- [3] Enderle R, Gotz-Neunhoeffler F, Gobbels M, Muller FA, Greil P. Influence of magnesium doping on the phase transformation temperature of beta-TCP ceramics examined by Rietveld refinement. *Biomaterials*. 2005;26:3379-84.
- [4] Xue W, Dahlquist K, Banerjee A, Bandyopadhyay A, Bose S. Synthesis and characterization of tricalcium phosphate with Zn and Mg based dopants. *J Mater Sci Mater Med*. 2008;19:2669-77.
- [5] Marie PJ. Strontium as therapy for osteoporosis. *Curr Opin Pharmacol*. 2005;5:633-6.
- [6] Schumacher M, Gelinsky M. Strontium modified calcium phosphate cements - approaches towards targeted stimulation of bone turnover. *Journal of Materials Chemistry B*. 2015;3:4626-40.
- [7] Chow LC. Calcium phosphate cements. *Monogr Oral Sci*. 2001;18:148-63.
- [8] Saint-Jean SJ, Camire CL, Nevsten P, Hansen S, Ginebra MP. Study of the reactivity and in vitro bioactivity of Sr-substituted alpha-TCP cements. *J Mater Sci Mater Med*. 2005;16:993-1001.
- [9] Suryanarayana C. Mechanical alloying and milling. *Progress in Materials Science*. 2001;46:1-184.
- [10] Ginebra MP, Canal C, Espanol M, Pastorino D, Montufar EB. Calcium phosphate cements as drug delivery materials. *Adv Drug Deliv Rev*. 2012;64:1090-110.
- [11] Kreidler ER, Hummel FA. Phase relations in the system SrO-P2O5 and the influence of water vapor on the formation of Sr4P2O9. *Inorganic Chemistry*. 1967;6:884-91.
- [12] Welch JH, Gutt W. High-temperature studies of the system calcium oxide-phosphorus pentoxide. *Journal of the Chemical Society (Resumed)*. 1961:4442-4.
- [13] Cicek G, Aksoy EA, Durucan C, Hasirci N. Alpha-tricalcium phosphate (alpha-TCP): solid state synthesis from different calcium precursors and the hydraulic reactivity. *J Mater Sci Mater Med*. 2011;22:809-17.
- [14] Montufar EB, Maazouz Y, Ginebra MP. Relevance of the setting reaction to the injectability of tricalcium phosphate pastes. *Acta Biomater*. 2013;9:6188-98.

- [15] Chow LC. Next generation calcium phosphate-based biomaterials. *Dental Materials Journal*. 2009;28:1-10.
- [16] Espanol M, Portillo J, Manero JM, Ginebra MP. Investigation of the hydroxyapatite obtained as hydrolysis product of alpha-tricalcium phosphate by transmission electron microscopy. *Crystengcomm*. 2010;12:3318-26.
- [17] Cunha C, Sprio S, Panseri S, Dapporto M, Marcacci M, Tampieri A. High biocompatibility and improved osteogenic potential of novel Ca-P/titania composite scaffolds designed for regeneration of load-bearing segmental bone defects. *J Biomed Mater Res A*. 2013;101:1612-9.
- [18] de Falco R, Scarano E, Di Celmo D, Grasso U, Guarnieri L. Balloon kyphoplasty in traumatic fractures of the thoracolumbar junction. Preliminary experience in 12 cases. *J Neurosurg Sci*. 2005;49:147-53.
- [19] Fölsch CD, Pinkernell R, Stiletto R. Biokompatibilität von Polymer-Glaskeramik-Zement Cortoss® : In-vitro-Testung mit dem MG63-Zell-Modell | Biocompatibility of polymer-bioglass cement Cortoss® : In vitro test with the MG63 cell model. 2013. p. 170-6.
- [20] Bohner M. Reactivity of calcium phosphate cements. *Journal of Materials Chemistry*. 2007;17:3980-6.
- [21] Dorozhkin SV. Calcium orthophosphate cements for biomedical application. *Journal of Materials Science*. 2008;43:3028-57.
- [22] Oda M, Takeuchi A, Lin X, Matsuya S, Ishikawa K. Effects of liquid phase on basic properties of alpha-tricalcium phosphate-based apatite cement. *Dent Mater J*. 2008;27:672-7.
- [23] TenHuisen KS, Brown PW. Formation of calcium-deficient hydroxyapatite from alpha-tricalcium phosphate. *Biomaterials*. 1998;19:2209-17.
- [24] Barkarmo S, Wennerberg A, Hoffman M, Kjellin P, Breding K, Handa P, et al. Nano-hydroxyapatite-coated PEEK implants: a pilot study in rabbit bone. *J Biomed Mater Res A*. 2013;101:465-71.
- [25] Landi E, Logroscino G, Proietti L, Tampieri A, Sandri M, Sprio S. Biomimetic Mg-substituted hydroxyapatite: from synthesis to in vivo behaviour. *J Mater Sci Mater Med*. 2008;19:239-47.
- [26] Landi E, Tampieri A, Celotti G, Belmonte MM, Logroscino G. Synthetic biomimetic nanostructured hydroxyapatite. *Bioceramics*, Vol 17. 2005;284-286:949-52.
- [27] Dempster DW, Compston JE, Drezner MK, Glorieux FH, Kanis JA, Malluche H, et al. Standardized Nomenclature, Symbols, and Units for Bone Histomorphometry: A 2012 Update of the Report of the ASBMR Histomorphometry Nomenclature Committee. *Journal of Bone and Mineral Research*. 2013;28:1-16.
- [28] Chen CS, Ingber DE. Tensegrity and mechanoregulation: from skeleton to cytoskeleton. *Osteoarthritis and Cartilage*. 1999;7:81-94.
- [29] Huang CY, Ogawa R. Mechanotransduction in bone repair and regeneration. *Faseb Journal*. 2010;24:3625-32.
- [30] Santos A, Bakker AD, Klein-Nulend J. The role of osteocytes in bone mechanotransduction. *Osteoporosis International*. 2009;20:1027-31.
- [31] Sprio S, Sandri M, Iafisco M, Panseri S, Filardo G, Kon E, et al. 9 - Composite biomedical foams for engineering bone tissue. In: Netti PA, editor. *Biomedical*



- Foams for Tissue Engineering Applications: Woodhead Publishing; 2014. p. 249-80.
- [32] Zhang J, Liu W, Schnitzler V, Tancret F, Bouler JM. Calcium phosphate cements for bone substitution: chemistry, handling and mechanical properties. *Acta Biomater.* 2014;10:1035-49.
- [33] Kona S, Wadajkar AS, Nguyen KT. 6 - Tissue engineering applications of injectable biomaterials A2 - Vernon, Brent. *Injectable Biomaterials*: Woodhead Publishing; 2011. p. 142-82.
- [34] Stankewich CJ, Swiontkowski MF, Tencer AF, Yetkinler DN, Poser RD. Augmentation of femoral neck fracture fixation with an injectable calcium-phosphate bone mineral cement. *Journal of Orthopaedic Research.* 1996;14:786-93.
- [35] Ginebra MP, Driessens FC, Planell JA. Effect of the particle size on the micro and nanostructural features of a calcium phosphate cement: a kinetic analysis. *Biomaterials.* 2004;25:3453-62.
- [36] Lopez-Heredia MA, Bohner M, Zhou W, Winnubst AJA, Wolke JGC, Jansen JA. The effect of ball milling grinding pathways on the bulk and reactivity properties of calcium phosphate cements. *Journal of Biomedical Materials Research Part B-Applied Biomaterials.* 2011;98B:68-79.
- [37] Gbureck U, Barralet JE, Radu L, Klinger HG, Thull R. Amorphous  $\alpha$ -Tricalcium Phosphate: Preparation and Aqueous Setting Reaction. *Journal of the American Ceramic Society.* 2004;87:1126-32.
- [38] Schilz J. Internal kinematics of tumbler and planetary ball mills: A mathematical model for the parameter setting. *Materials Transactions Jim.* 1998;39:1152-7.
- [39] Camire CL, Gbureck U, Hirsiger W, Bohner M. Correlating crystallinity and reactivity in an alpha-tricalcium phosphate. *Biomaterials.* 2005;26:2787-94.
- [40] Gbureck U, Thull R, Barralet JE. Alkali ion substituted calcium phosphate cement formation from mechanically activated reactants. *J Mater Sci Mater Med.* 2005;16:423-7.
- [41] Araujo PW, Brereton RG. Experimental design .2. Optimization. *Trac-Trends in Analytical Chemistry.* 1996;15:63-70.
- [42] Montgomery DC. *Design and Analysis of Experiments*: John Wiley & Sons; 2008.
- [43] Rhodes M. Index. *Introduction to Particle Technology*: John Wiley & Sons, Ltd; 2008. p. 441-50.
- [44] Takacs L, Pardaviihorvath M. Magnetic-Properties of Nanocomposites Prepared by Mechanical Alloying. *Nanophases and Nanocrystalline Structures.* 1993:135-44.
- [45] Tao Y, Li DX, Li YB. Effect of substitutional Sr ion on mechanical properties of calcium phosphate bone cement. *Journal of Wuhan University of Technology-Materials Science Edition.* 2013;28:741-5.
- [46] Espanol M, Perez RA, Montufar EB, Marichal C, Sacco A, Ginebra MP. Intrinsic porosity of calcium phosphate cements and its significance for drug delivery and tissue engineering applications. *Acta Biomaterialia.* 2009;5:2752-62.

[47] Liu C, Shao H, Chen F, Zheng H. Effects of the granularity of raw materials on the hydration and hardening process of calcium phosphate cement. *Biomaterials*. 2003;24:4103-13.

# FINAL CONCLUSIONS AND FUTURE PERSPECTIVES

---

In the present work, novel biomimetic bone scaffolds addressed to regenerative bone surgery have been developed and optimized following three different approaches. In summary:

- 1) large and macroporous hydroxyapatite scaffolds with controlled pore distribution and improved mechanical performance were prepared by a novel route based on direct foaming of ceramic suspensions. The optimization of this process by the use of a planetary ball mill for the powder processing enabled a radical shortening of the process time and improvement of the scaffold homogeneity. Such scaffolds can be addressed to the regeneration of load-bearing bones, particularly in cranio-maxillofacial and orthopaedic surgery, where regenerative solutions to large bone defects are still lacking.
- 2) the fabrication of bioactive complex-shape macro- and micro-porous  $\beta$ TCP-based scaffolds was achieved by 3D printing. The reported mechanical strength was comparable with the typical values of trabecular bone but a further tuning of the processing parameters is needed to achieve mechanical performance enabling load-bearing applications. In particular, it can be envisaged that further powder processing may enable closer packing of the ceramic particles, thus leading to improved viscoelasticity of the colloidal inks and final mechanical strength.
- 3) a novel formulation of injectable, self-setting strontium-substituted apatitic bone cement enriched with alginate was prepared, exhibiting promising features as injectable bioactive paste for the regeneration of complex-shape bony regions such as vertebral bodies or tibial plateau, particularly in the

case of degenerative diseases such as osteoporosis. An extensive micro-porosity was shown to enhance new bone formation and penetration. Despite the reported compressive strength can be improved in order to adequately withstand the early biomechanical loads upon implantation, the new cement can be considered promising for load-bearing applications, as the fast penetration of new bone and the subsequent improvement of the bone/cement construct mechanical performance can be envisaged, thus leading to progressive stabilization of the defect.

In the last decades, a great deal of research effort has been devoted to the preparation of scaffolds able to fulfill all the requirements of chemically active surfaces and mimesis of morpho-structural features of bone, both considered as necessary to induce effective bone regeneration. However, the regeneration of critical size bone defects is still a major challenge in bone tissue engineering.

Despite further advances are still required to meet the clinical need for load-bearing bone regeneration, the results of the research conducted in the present thesis highlight promising combination of bioactivity, porosity and mechanical performance in the developed biomaterials, as well as new strategies to achieve more accurate design of the ceramic processing, towards the desired features of the final scaffold.

# ACKNOWLEDGMENTS

---

Firstly, I wanted to say thanks and share my gratitude to my Family, especially my Mum, my Dad and my Brother: they always supported me, while teaching the indispensable value of Home.

My heartfelt gratitude goes also to Martina, for her understanding, support and love.

This thesis would not have been possible without Simone Sprio and Anna Tampieri, who introduced me to the bioceramics research field and supervised all my work.

I want to thank all my colleagues of the *Bioceramics and Bio-hybrid Composites Group* from the Institute of Science and Technology for Ceramics (Italy), for their support and collaboration, in particular Silvia Panseri, Monica Montesi, for the valuable contribution and discussion about the biological interaction of biomaterials and for the biological *in vitro* tests. I would also thank Claudio Capiani, Cesare Melandri, Guia Guarini, Andreana Piancastelli, for the significant support in the lab during the characterization of my materials.

I wish to thank Prof. Luca Cristofolini, my academic supervisor, and the staff of his lab, for the smart suggestions and valuable support during my PhD.

My thanks also go to a lot of scientists from companies and other academic institutions who collaborated to the studies presented in this thesis. In particular I would like to thank Elisa Figallo and Claudia Fabbi, from Finceramica S.p.A (Faenza, Italy), as well as Wanda Lattanzi, Giandomenico Logroscino (Università Cattolica Sacro Cuore-Policlinico Gemelli, Rome, Italy) for the *in vivo* tests.

I wish to take the opportunity to thank also Prof. Eduardo Saiz Gutierrez, for letting me the chance to work in his laboratory at Imperial College London for 6 months. A special thanks to all the guys from the Centre for Advanced Structural Ceramics, in particular Gil Costa Machado and Ezra Feilden-Irving, for their kindness and availability during my period in London.